APPLIED COMPUTATIONAL ELECTROMAGNETICS SOCIETY JOURNAL

March 2018
Vol. 33 No. 3
ISSN 1054-4887

The ACES Journal is abstracted in INSPEC, in Engineering Index, DTIC, Science Citation Index Expanded, the Research Alert, and to Current Contents/Engineering, Computing & Technology.

The illustrations on the front cover have been obtained from the research groups at the Department of Electrical Engineering, The University of Mississippi.

THE APPLIED COMPUTATIONAL ELECTROMAGNETICS SOCIETY
http://aces-society.org

EDITORS-IN-CHIEF

Atef Elsherbeni
Colorado School of Mines, EE Dept.
Golden, CO 80401, USA

Sami Barmada
University of Pisa, ESE Dept.
56122 Pisa, Italy

ASSOCIATE EDITORS-IN-CHIEF: REGULAR PAPERS

Mohammed Hadi
Kuwait University, EE Dept.
Safat, Kuwait

Antonio Musolino
University of Pisa
56126 Pisa, Italy

Marco Arjona López
La Laguna Institute of Technology
Torreon, Coahuila 27266, Mexico

Alistair Duffy
De Montfort University
Leicester, UK

Abdul A. Arkadan
Colorado School of Mines, EE Dept.
Golden, CO 80401, USA

Paolo Mezzanotte
University of Perugia
I-06125 Perugia, Italy

Wenxing Li
Harbin Engineering University
Harbin 150001, China

Salvatore Campione
Sandia National Laboratories
Albuquerque, NM 87185, USA

Luca Di Rienzo
Politecnico di Milano
20133 Milano, Italy

Maokun Li
Tsinghua University
Beijing 100084, China

Wei-Chung Weng
National Chi Nan University, EE Dept.
Puli, Nantou 54561, Taiwan

Rocco Rizzo
University of Pisa
56123 Pisa, Italy

ASSOCIATE EDITORS-IN-CHIEF: EXPRESS PAPERS

Lijun Jiang
University of Hong Kong, Dept. of EEE
Hong, Kong

Steve J. Weiss
US Army Research Laboratory
Adelphi Laboratory Center (RDRL-SER-M)
Adelphi, MD 20783, USA

Amedeo Capozzoli
Univerita di Napoli Federico II, DIETI
I-80125 Napoli, Italy

Shinichiro Ohnuki
Nihon University
Tokyo, Japan

William O'Keefe Coburn
US Army Research Laboratory
Adelphi Laboratory Center (RDRL-SER-M)
Adelphi, MD 20783, USA

Yu Mao Wu
Fudan University
Shanghai 200433, China

Kubilay Sertel
The Ohio State University
Columbus, OH 43210, USA

Jiming Song
Iowa State University, ECE Dept.
Ames, IA 50011, USA

Maokun Li
Tsinghua University, EE Dept.
Beijing 100084, China

EDITORIAL ASSISTANTS

Matthew J. Inman
University of Mississippi, Electrical Engineering Dept.
University, MS 38677, USA

Shanell Lopez
Colorado School of Mines, Electrical Engineering Dept.
Golden, CO 80401, USA

EMERITUS EDITORS-IN-CHIEF

Duncan C. Baker
EE Dept. U. of Pretoria
0002 Pretoria, South Africa

Allen Glisson
University of Mississippi, EE Dept.
University, MS 38677, USA

Ahmed Kishk
Concordia University, ECS Dept.
Montreal, QC H3G 1M8, Canada

Robert M. Bevensee
Box 812
Alamo, CA 94507-0516, USA

Ozlem Kilic
Catholic University of America
Washington, DC 20064, USA

David E. Stein
USAF Scientific Advisory Board
Washington, DC 20330, USA

EMERITUS ASSOCIATE EDITORS-IN-CHIEF

Yasushi Kanai
Niigata Inst. of Technology
Kashiwazaki, Japan

Levent Gurel
Bilkent University
Ankara, Turkey

Erdem Topsakal
Mississippi State University, EE Dept.
Mississippi State, MS 39762, USA

Mohamed Abouzahra
MIT Lincoln Laboratory
Lexington, MA, USA

Sami Barmada
University of Pisa, ESE Dept.
56122 Pisa, Italy

Alexander Yakovlev
University of Mississippi, EE Dept.
University, MS 38677, USA

Ozlem Kilic
Catholic University of America
Washington, DC 20064, USA

Fan Yang
Tsinghua University, EE Dept.
Beijing 100084, China

EMERITUS EDITORIAL ASSISTANTS

Khaled ElMaghoub
Trimble Navigation/MIT
Boston, MA 02125, USA

Anne Graham
University of Mississippi, EE Dept.
University, MS 38677, USA

Christina Bonnington
University of Mississippi, EE Dept.
University, MS 38677, USA

Mohamed Al Sharkawy
Arab Academy for Science and Technology, ECE Dept.
Alexandria, Egypt

MARCH 2018 REVIEWERS: REGULAR PAPERS

Mehmet Belen
Jinqun Ge
Han Guo
Guangwei Hu
Binke Huang
He Huang
Yongjun Huang
Achraf Jaoujal
Bing Li
Shisong Li
Mahdi Moosazadeh
Andrea Morabito
Payam Nayeri
Muthurajkumar Sannasy
Omar Saraereh
Mustafa Secmen
Chan See
Dan Shi
Kevn Shih
Ting-Yen Shih
Yu Tian
Hossein Torkaman
Lingasamy Veluchamy
Ramya Vijay
Yu Mao Wu
Huan Zhang
Kedi Zhang

MARCH 2018 REVIEWERS: EXPRESS PAPERS

Fangyuan Chen
William Coburn
Vivek Dhoot
Siping Gao
Lu Guo
Mang He
Bernhard Hoenders
Lijun Jiang
George Kyriacou
Quang Nguyen
Rashid Saleem
Nghia Tran
Nurhan Turker Tokan
Arash Valizade Shahmirzadi
Yansheng Wang

THE APPLIED COMPUTATIONAL ELECTROMAGNETICS SOCIETY JOURNAL

Vol. 33 No. 3 March 2018

TABLE OF CONTENTS – REGULAR PAPERS

TABLE OF CONTENTS – EXPRESS PAPERS

Wide-Angle Claerbout Scheme for Three-Dimensional Time Domain Parabolic Equation and its CN, ADI, AGE Solutions

Zi He [1,2], Hong-Cheng Yin [1], and Ru-Shan Chen [2]

[1] Science and Technology on Electromagnetic Scattering Laboratory
Beijing Institute of Environmental Features (BIEF), China
zihe@njust.edu.cn, yinhc207@126.com

Department of Communication Engineering
Nanjing University of Science and Technology, Nanjing 210094, China
eerschen@njust.edu.cn

Abstract – The wide-angle Claerbout scheme of three-dimensional time domain parabolic equation (Claerbout-TDPE) is derived in this paper, which can provide accurate results at angles within 25° of the paraxial direction. At first, the Crank-Nicolson (CN) type is introduced to discretize the Claerbout-TDPE. In this way, a three-dimensional EM scattering problem can be divided into a series of two-dimensional ones. Moreover, the alternating direction implicit (ADI) type is utilized to the Claerbout-TDPE. In this way, a three-dimensional EM scattering problem can be further reduced to a series of one-dimensional ones. Furthermore, the alternating group explicit (AGE) type is introduced to the Claerbout-TDPE for higher computational efficiency. Comparisons are made among the CN, ADI and AGE types in the numerical results.

Index Terms – Electromagnetic scattering, time domain parabolic equation, wide angle.

I. INTRODUCTION

The parabolic equation (PE) has been applied to study the wave propagation [1-3] and EM scattering problems [4-7] for several decades. The split-step Fourier-based PE is extremely attractive for its computational efficiency. However, it lacks the flexibility of boundary modeling for complicated targets. Therefore, it is best to use the FD schemes when dealing with problems of complicated boundaries. When applying the finite difference method to the paraxial direction, the PE can be solved in a marching manner. As a result, a series of two-dimensional problems are needed to be computed instead of a three-dimensional problem. Therefore, the computational efficiency can be improved significantly. However, the traditional PE methods are based on finite difference schemes in each transverse plane, which use rectangular meshes. This kind of meshes will result in poor accuracy to approximate complex targets. Moreover, the PE method cannot model the scattering targets with large changes along paraxial direction since the creeping waves cannot be captured. Therefore, some hybrid PE methods have been proposed by us to improve the accuracy and expand the application of the traditional PE method for EM scattering problems [8-11]. Moreover, some novel finite difference schemes and parallel technologies are introduced to accelerate the calculation of PE method [2-3, 11-13]. All of these works are focus on narrow-angle approximation of parabolic equation, which can obtain accurate results within 15° of the paraxial direction. Wide-angle parabolic equation methods were introduced for wider angle EM analysis by using high-order expansions of exponential or square-root functions. The Pade approximation [7, 14-17] is the most popular one, but may result in bad computational efficiency or instability with the Pade order increasing. The right approach is to use rational approximations instead. Therefore, the development of the Claerbout solution has a practical significance. The error for a plane wave propagating at angle α from the horizontal is of the order of $(\sin\alpha)^6$, which makes it acceptable for propagation angles up to 45 degrees or so from the paraxial direction.

In recent years, the transient EM scattering analysis becomes a hot topic. Some numerical methods are used for wide-band analysis, such as the time domain integral equation (TDIE) method, the finite-different time-domain (FDTD) method and so on. However, it is time-consuming to obtain the transient EM properties by these numerical methods. Therefore, the time domain parabolic equation (TDPE) method was proposed to fast solve the transient problems [18-23]. By implementing the finite difference scheme along both the temporal and paraxial directions, the calculation can be taken plane by plane for each time step. It can be found that high efficiency can be obtained by the TDPE method [22]. Moreover, we proposed a marching-on-in-degree solver

Submitted On: September 28, 2017
Accepted On: January 3, 2018

of TDPE in which the weighted Laguerre polynomials are used to expand the electrical fields [23-25]. However, all these methods can only provide accurate results at a small angle of 15° along the paraxial direction.

In this paper, the three-dimensional time domain wide-angle Claerbout parabolic equation (Claerbout-TDPE) is formulated firstly. Accurate results can be obtained at angles within 25° of the paraxial direction by the Claerbout-TDPE method while 15° for the traditional TDPE method. Then three different kinds of finite difference schemes are introduced to solve the Claerbout-TDPE, namely the Crank-Nicolson (CN) scheme, the alternating direction implicit (ADI) scheme and the alternating group explicit (AGE) scheme. For CN scheme, the calculation can be performed in a marching manner along the paraxial direction for each time step. For ADI scheme, the unknowns can be computed row by row or column by column in each transverse plane for any time step, thus the computational efficiency is further improved. For AGE scheme, the reduced transient scattered fields in each transverse plane of any time step are obtained directly without solving any matrix equations. As a result, it has the best performance among CN, ADI and AGE schemes. Moreover, the bistatic RCS result at any observed angle can be obtained by rotating Claerbout-TDPE method. Several numerical examples are given to demonstrate the validity of the proposed method and comparisons are made among different schemes. It can be observed that the AGE scheme of Claerbout-TDPE method can save the computational resources when compared with both the CN and ADI schemes.

II. THEORY

The wide-angle Claerbout TDPE

The standard parabolic equation in frequency domain can be expressed as:

$$\left[\frac{\partial}{\partial x}+ik(1-\sqrt{1+Q})\right]u_\xi^s=0 \qquad \xi=x,y,z\,, \tag{1}$$

where u_ξ^s denotes the reduced scattered fields, the x axis is supposed to be the paraxial direction of the parabolic equation. The pseudo-differential operator Q in free space is defined by:

$$Q=\frac{1}{k^2}\left(\frac{\partial^2}{\partial y^2}+\frac{\partial^2}{\partial z^2}\right). \tag{2}$$

The square-root operator in (1) is expanded with the one order Pade approximation [7], which can be derived as:

$$\begin{aligned}&\frac{\partial u_\xi^s}{\partial x}+\frac{0.25}{k^2}\frac{\partial^3 u_\xi^s}{\partial x\partial^2 y}+\frac{0.25}{k^2}\frac{\partial^3 u_\xi^s}{\partial x\partial^2 z}\\ &\quad=ik\left[\frac{0.5}{k^2}\left(\frac{\partial^2}{\partial y^2}+\frac{\partial^2}{\partial z^2}\right)\right]u_\xi^s \qquad \xi=x,y,z\end{aligned}\,. \tag{3}$$

Introduce the Fourier transform along the *x,y,z* axes, which is given by:

$$\Pi_\xi^s(x,y,z,s)=\frac{1}{2\pi}\int_{-\infty}^{\infty}\tilde{F}(k)u_\xi^s(x,y,z,k)e^{-iks}dk\,, \qquad \xi=x,y,z \tag{4}$$

where $\tilde{F}(k)$ represents the spectrum function, $s=ct-x$ and c is the light speed.

Then the three-dimensional time domain wide-angle Claerbout parabolic equation (Claerbout-TDPE) can be derived by using the forward Fourier transform:

$$4\frac{1}{c^2}\frac{\partial^3\Pi_\xi^s}{\partial t^2\partial x}-2\frac{1}{c}\left(\frac{\partial^3\Pi_\xi^s}{\partial t\partial y^2}+\frac{\partial^3\Pi_\xi^s}{\partial t\partial z^2}\right)=\frac{\partial^3\Pi_\xi^s}{\partial x\partial^2 y}+\frac{\partial^3\Pi_\xi^s}{\partial x\partial^2 z}\,. \qquad \xi=x,y,z \tag{5}$$

By introducing the CN scheme to both the temporal and marching steps, the semi-discretized formula for (5) can be obtained:

$$\begin{aligned}&\frac{4}{c^2\Delta x\Delta t^2}\begin{pmatrix}\Pi_{\xi,n+1,l+1}^s-\Pi_{\xi,n,l+1}^s+\Pi_{\xi,n+1,l-1}^s\\ -\Pi_{\xi,n,l-1}^s-2\Pi_{\xi,n+1,l}^s+2\Pi_{\xi,n,l}^s\end{pmatrix}\\ &\quad=\left(1+\frac{2}{c\Delta t}\right)\begin{pmatrix}\frac{1}{\Delta y^2}\nabla_y^2\left(\Pi_{\xi,n,l+1}^s-\Pi_{\xi,n,l}^s\right)+\\ \frac{1}{\Delta z^2}\nabla_z^2\left(\Pi_{\xi,n,l+1}^s-\Pi_{\xi,n,l}^s\right)\end{pmatrix},\\ &\qquad\qquad \xi=x,y,z\end{aligned} \tag{6}$$

in which, ${\Pi^s}_{\xi,n,l}$ is the transient reduced scattered fields for ξ component, Δx denotes the range step along the paraxial direction, Δt represents the time step, and ∇_y^2,∇_z^2 are the second-order difference operators.

It can be observed from (6) that the calculation can be taken plane by plane along the paraxial direction for any time step. As a result, the computational resources can be saved significantly. The CN, ADI, AGE solutions of Claerbout-TDPE are discussed as follows.

The equations in (6) are coupled with the inhomogeneous boundary conditions. For the conducting targets, the tangential total field is zero on the surface, which yields:

$$\begin{aligned}&n_x\Pi_y^s(x_b,y_b,z_b,t)-n_y\Pi_x^s(x_b,y_b,z_b,t)=\\ &\qquad -n_xE_y^i(x_b,y_b,z_b,t-x_b/c)+n_yE_x^i(x_b,y_b,z_b,t-x_b/c)\\ &n_x\Pi_z^s(x_b,y_b,z_b,t)-n_z\Pi_x^s(x_b,y_b,z_b,t)=\\ &\qquad -n_xE_z^i(x_b,y_b,z_b,t-x_b/c)+n_zE_x^i(x_b,y_b,z_b,t-x_b/c)\\ &n_y\Pi_z^s(x_b,y_b,z_b,t)-n_z\Pi_y^s(x_b,y_b,z_b,t)=\\ &\qquad -n_yE_z^i(x_b,y_b,z_b,t-x_b/c)+n_zE_y^i(x_b,y_b,z_b,t-x_b/c)\end{aligned}\,, \tag{7}$$

where $\mathbf{E}^\mathbf{i}$ is the incident field, (x_b,y_b,z_b) represents the boundary point, and (n_x,n_y,n_z) denotes the outer normal component.

Moreover, the divergence-free condition is used to ensure the unicity [4]:

$$-\frac{1}{2}\left(\frac{\partial^2\Pi_x^s}{\partial y^2}+\frac{\partial^2\Pi_x^s}{\partial z^2}\right)+\frac{1}{c^2}\frac{\partial^2\Pi_x^s}{\partial t^2}+\frac{1}{c}\frac{\partial^2\Pi_y^s}{\partial y\partial t}+\frac{1}{c}\frac{\partial^2\Pi_z^s}{\partial z\partial t}=0\,. \quad (8)$$

CN solution of the Claerbout-TDPE

By introducing the CN scheme to (6), the full-discretized form of Claerbout-TDPE can be obtained:

$$\begin{aligned}
&\left(\frac{4}{c^2\Delta x\Delta t^2}+\frac{1}{c\Delta t\Delta y^2}+\frac{1}{\Delta x\Delta y^2}+\frac{1}{c\Delta t\Delta z^2}+\frac{1}{\Delta x\Delta z^2}\right)\Pi_{\xi,n+1,l+1}^{s,p,q}-\left(\frac{1}{2c\Delta t\Delta y^2}+\frac{1}{2\Delta x\Delta y^2}\right)\left(\Pi_{\xi,n+1,l+1}^{s,p+1,q}+\Pi_{\xi,n+1,l+1}^{s,p-1,q}\right)\\
&\quad-\left(\frac{1}{2c\Delta t\Delta z^2}+\frac{1}{2\Delta x\Delta z^2}\right)\left(\Pi_{\xi,n+1,l+1}^{s,p,q+1}+\Pi_{\xi,n+1,l+1}^{s,p,q-1}\right)\\
&=\frac{4}{c^2\Delta x\Delta t^2}\left(2\Pi_{\xi,n+1,l}^{s,p,q}-2\Pi_{\xi,n,l}^{s,p,q}+\Pi_{\xi,n,l+1}^{s,p,q}+\Pi_{\xi,n,l-1}^{s,p,q}-\Pi_{\xi,n+1,l-1}^{s,p,q}\right)+\frac{1}{2\Delta x\Delta y^2}\begin{pmatrix}\Pi_{\xi,n+1,l}^{s,p+1,q}+\Pi_{\xi,n+1,l}^{s,p-1,q}-2\Pi_{\xi,n+1,l}^{s,p,q}\\ -\Pi_{\xi,n,l}^{s,p+1,q}-\Pi_{\xi,n,l}^{s,p-1,q}+2\Pi_{\xi,n,l}^{s,p,q}\end{pmatrix}\\
&\quad+\frac{1}{2\Delta x\Delta z^2}\begin{pmatrix}\Pi_{\xi,n+1,l}^{s,p,q+1}+\Pi_{\xi,n+1,l}^{s,p,q-1}-2\Pi_{\xi,n+1,l}^{s,p,q}\\ -\Pi_{\xi,n,l}^{s,p,q+1}-\Pi_{\xi,n,l}^{s,p,q-1}+2\Pi_{\xi,n,l}^{s,p,q}\end{pmatrix}+\left(\frac{1}{2c\Delta t\Delta y^2}-\frac{1}{2\Delta x\Delta y^2}\right)\left(\Pi_{\xi,n,l+1}^{s,p+1,q}+\Pi_{\xi,n,l+1}^{s,p-1,q}-2\Pi_{\xi,n,l+1}^{s,p,q}\right)\\
&\quad+\left(\frac{1}{2c\Delta t\Delta z^2}-\frac{1}{2\Delta x\Delta z^2}\right)\left(\Pi_{\xi,n,l+1}^{s,p,q+1}+\Pi_{\xi,n,l+1}^{s,p,q-1}-2\Pi_{\xi,n,l+1}^{s,p,q}\right)-\frac{1}{2c\Delta t\Delta y^2}\begin{pmatrix}\Pi_{\xi,n+1,l-1}^{s,p+1,q}+\Pi_{\xi,n+1,l-1}^{s,p-1,q}-2\Pi_{\xi,n+1,l-1}^{s,p,q}\\ +\Pi_{\xi,n,l-1}^{s,p+1,q}+\Pi_{\xi,n,l-1}^{s,p-1,q}-2\Pi_{\xi,n,l-1}^{s,p,q}\end{pmatrix}\\
&\quad-\frac{1}{2c\Delta t\Delta z^2}\begin{pmatrix}\Pi_{\xi,n+1,l-1}^{s,p,q+1}+\Pi_{\xi,n+1,l-1}^{s,p,q-1}-2\Pi_{\xi,n+1,l-1}^{s,p,q}\\ +\Pi_{\xi,n,l-1}^{s,p,q+1}+\Pi_{\xi,n,l-1}^{s,p,q-1}-2\Pi_{\xi,n,l-1}^{s,p,q}\end{pmatrix}\qquad \xi=x,y,z
\end{aligned}\quad ,(9)$$

where $\Delta y,\Delta z$ denote the range steps along the y, z directions, $\Pi_{\xi,n,l}^{s,p,q}$ is the ξ component of the transient reduced scattered field for $(n\Delta x, p\Delta y, q\Delta z)$ at the l th time step.

It can be seen that the unknowns in the $(n+1)th$ transverse plane for the $(l+1)th$ time step can be computed by the known fields of previous time steps and transverse planes. In this way, the Claerbout-TDPE can be calculated in a marching manner.

ADI solution of the Claerbout-TDPE

The ADI solution of the wide-angle Claerbout PE in frequency domain has been introduced in [16]. Then its time domain counterpart can be derived as:

$$\begin{aligned}
&\begin{bmatrix}\frac{1}{4c\Delta t\Delta y^2} & -\left(\frac{1}{2c\Delta t\Delta y^2}+\frac{1}{\Delta x\Delta t^2c^2}\right) & \frac{1}{4c\Delta t\Delta y^2}\end{bmatrix}\begin{bmatrix}\Pi_{\xi,n+1/2,l+1}^{s,p-1,q}\\ \Pi_{\xi,n+1/2,l+1}^{s,p,q}\\ \Pi_{\xi,n+1/2,l+1}^{s,p+1,q}\end{bmatrix}\\
&=\begin{bmatrix}-\frac{1}{4c\Delta t\Delta z^2} & \left(\frac{1}{2c\Delta t\Delta z^2}-\frac{1}{\Delta x\Delta t^2c^2}\right) & -\frac{1}{4c\Delta t\Delta z^2}\end{bmatrix}\begin{bmatrix}\Pi_{\xi,n,l+1}^{s,p,q-1}\\ \Pi_{\xi,n,l+1}^{s,p,q}\\ \Pi_{\xi,n,l+1}^{s,p,q+1}\end{bmatrix}\\
&+\begin{bmatrix}\left(\frac{1}{4\Delta x\Delta z^2}+\frac{1}{4c\Delta t\Delta z^2}\right) & \left(\frac{2}{\Delta x\Delta t^2c^2}-\frac{1}{2c\Delta t\Delta z^2}-\frac{1}{2\Delta x\Delta z^2}\right) & \left(\frac{1}{4\Delta x\Delta z^2}+\frac{1}{4c\Delta t\Delta z^2}\right)\end{bmatrix}\begin{bmatrix}\Pi_{\xi,n,l}^{s,p,q-1}\\ \Pi_{\xi,n,l}^{s,p,q}\\ \Pi_{\xi,n,l}^{s,p,q+1}\end{bmatrix}\\
&-\begin{bmatrix}\left(\frac{1}{4\Delta x\Delta y^2}-\frac{1}{4c\Delta t\Delta y^2}\right) & \left(\frac{2}{\Delta x\Delta t^2c^2}+\frac{1}{2c\Delta t\Delta y^2}-\frac{1}{2\Delta x\Delta y^2}\right) & \left(\frac{1}{4\Delta x\Delta y^2}-\frac{1}{4c\Delta t\Delta y^2}\right)\end{bmatrix}\begin{bmatrix}\Pi_{\xi,n+1/2,l}^{s,p-1,q}\\ \Pi_{\xi,n+1/2,l}^{s,p,q}\\ \Pi_{\xi,n+1/2,l}^{s,p+1,q}\end{bmatrix}\\
&-\frac{1}{\Delta x\Delta t^2c^2}\Pi_{\xi,n,l-1}^{s,p,q}+\frac{1}{\Delta x\Delta t^2c^2}\Pi_{\xi,n+1/2,l-1}^{s,p,q}\qquad \xi=x,y,z
\end{aligned}\quad ,\ (10)$$

$$
\begin{aligned}
&\begin{bmatrix} \dfrac{1}{4c\Delta t\Delta z^2} & -\left(\dfrac{1}{2c\Delta t\Delta z^2}+\dfrac{1}{\Delta x\Delta t^2c^2}\right) & \dfrac{1}{4c\Delta t\Delta z^2} \end{bmatrix}
\begin{bmatrix} \Pi_{\xi,n+1,l+1}^{s,p-1,q} \\ \Pi_{\xi,n+1,l+1}^{s,p,q} \\ \Pi_{\xi,n+1,l+1}^{s,p+1,q} \end{bmatrix} \\
&=\begin{bmatrix} -\dfrac{1}{4c\Delta t\Delta y^2} & \left(\dfrac{1}{2c\Delta t\Delta y^2}-\dfrac{1}{\Delta x\Delta t^2c^2}\right) & -\dfrac{1}{4c\Delta t\Delta y^2} \end{bmatrix}
\begin{bmatrix} \Pi_{\xi,n+1/2,l+1}^{s,p,q-1} \\ \Pi_{\xi,n+1/2,l+1}^{s,p,q} \\ \Pi_{\xi,n+1/2,l+1}^{s,p,q+1} \end{bmatrix} \\
&+\begin{bmatrix} \left(\dfrac{1}{4\Delta x\Delta y^2}+\dfrac{1}{4c\Delta t\Delta y^2}\right) & \left(\dfrac{2}{\Delta x\Delta t^2c^2}-\dfrac{1}{2c\Delta t\Delta y^2}-\dfrac{1}{2\Delta x\Delta y^2}\right) & \left(\dfrac{1}{4\Delta x\Delta y^2}+\dfrac{1}{4c\Delta t\Delta y^2}\right) \end{bmatrix}
\begin{bmatrix} \Pi_{\xi,n+1/2,l}^{s,p,q-1} \\ \Pi_{\xi,n+1/2,l}^{s,p,q} \\ \Pi_{\xi,n+1/2,l}^{s,p,q+1} \end{bmatrix}. \qquad (11) \\
&-\begin{bmatrix} \left(\dfrac{1}{4\Delta x\Delta z^2}-\dfrac{1}{4c\Delta t\Delta z^2}\right) & \left(\dfrac{2}{\Delta x\Delta t^2c^2}+\dfrac{1}{2c\Delta t\Delta z^2}-\dfrac{1}{2\Delta x\Delta z^2}\right) & \left(\dfrac{1}{4\Delta x\Delta z^2}-\dfrac{1}{4c\Delta t\Delta z^2}\right) \end{bmatrix}
\begin{bmatrix} \Pi_{\xi,n+1,l}^{s,p-1,q} \\ \Pi_{\xi,n+1,l}^{s,p,q} \\ \Pi_{\xi,n+1,l}^{s,p+1,q} \end{bmatrix} \\
&-\frac{1}{\Delta x\Delta t^2c^2}\Pi_{\xi,n+1/2,l-1}^{s,p,q}+\frac{1}{\Delta x\Delta t^2c^2}\Pi_{\xi,n+1,l-1}^{s,p,q} \qquad\qquad \xi = x, y, z
\end{aligned}
$$

It can be seen that the unknowns are solved line by line in each transverse plane for any time step. As a result, the computational efficiency can be further improved.

AGE solution of the Claerbout-TDPE

Four asymmetry schemes in Fig. 1 are introduced to (5), and then the AGE solution of the Claerbout TDPE can be expressed as:

$$
\begin{bmatrix} 1+r_1+r_2 & -r_1 & 0 & -r_2 \\ -r_1 & 1+r_1+r_2 & -r_2 & 0 \\ 0 & -r_2 & 1+r_1+r_2 & -r_1 \\ -r_2 & 0 & -r_1 & 1+r_1+r_2 \end{bmatrix}
\begin{bmatrix} \Pi_{\xi,n+1,l+1}^{s,p,q} \\ \Pi_{\xi,n+1,l+1}^{s,p+1,q} \\ \Pi_{\xi,n+1,l+1}^{s,p+1,q+1} \\ \Pi_{\xi,n+1,l+1}^{s,p,q+1} \end{bmatrix}
=\begin{bmatrix} a \\ b \\ c \\ d \end{bmatrix}, \qquad (12)
$$

$$\xi = x, y, z$$

in which,

$$
\begin{aligned}
a &= \left(r_1+r_2\right)\left(\Pi_{\xi,n,l+1}^{s,p-1,q}+\Pi_{\xi,n,l+1}^{s,p,q-1}\right)-\left(3r_1+3r_2-1\right)\Pi_{\xi,n,l+1}^{s,p,q} \\
&+r_2\Pi_{\xi,n,l+1}^{s,p,q+1}+r_1\Pi_{\xi,n,l+1}^{s,p+1,q}-\left(r_1+r_2\right)\left(\Pi_{\xi,n,l}^{s,p-1,q}+\Pi_{\xi,n,l}^{s,p,q-1}\right) \\
&-\left(2-3r_1-3r_2-\frac{1}{2r_3}\right)\Pi_{\xi,n,l}^{s,p,q}-\left(r_2+\frac{1}{4r_3}\right)\Pi_{\xi,n,l}^{s,p,q+1} \\
&-\left(r_1+\frac{1}{4r_3}\right)\Pi_{\xi,n+1,l}^{s,p+1,q}+\Pi_{\xi,n,l-1}^{s,p,q}+\left(2+r_1+r_2-\frac{1}{2r_3}\right)\Pi_{\xi,n+1,l}^{s,p,q} \\
&+\left(\frac{1}{4r_3}-r_1\right)\Pi_{\xi,n+1,l}^{s,p+1,q}+\left(\frac{1}{4r_3}-r_2\right)\Pi_{\xi,n+1,l}^{s,p,q+1}-\Pi_{\xi,n+1,l-1}^{s,p,q}
\end{aligned}
\qquad ,(13)
$$

$$
\begin{aligned}
b &= \left(r_1+r_2\right)\left(\Pi_{\xi,n,l+1}^{s,p+2,q}+\Pi_{\xi,n,l+1}^{s,p+1,q-1}\right)-\left(3r_1+3r_2-1\right)\Pi_{\xi,n,l+1}^{s,p+1,q} \\
&+r_1\Pi_{\xi,n,l+1}^{s,p,q}+r_2\Pi_{\xi,n,l+1}^{s,p+1,q+1}-\left(r_1+r_2\right)\left(\Pi_{\xi,n,l}^{s,p+2,q}+\Pi_{\xi,n,l}^{s,p+1,q-1}\right) \\
&-\left(2-3r_1-3r_2-\frac{1}{2r_3}\right)\Pi_{\xi,n,l}^{s,p+1,q}+\left(2+r_1+r_2-\frac{1}{2r_3}\right)\Pi_{\xi,n+1,l}^{s,p+1,q} \\
&-\left(r_2+\frac{1}{4r_3}\right)\Pi_{\xi,n,l}^{s,p+1,q+1}+\Pi_{\xi,n,l-1}^{s,p+1,q}+\left(\frac{1}{4r_3}-r_1\right)\Pi_{\xi,n+1,l}^{s,p,q} \\
&+\left(\frac{1}{4r_3}-r_2\right)\Pi_{\xi,n+1,l}^{s,p+1,q+1}-\left(r_1+\frac{1}{4r_3}\right)\Pi_{\xi,n,l}^{s,p,q}-\Pi_{\xi,n+1,l-1}^{s,p+1,q}
\end{aligned}
\qquad , \qquad (14)
$$

$$
\begin{aligned}
c &= \left(r_1+r_2\right)\left(\Pi_{\xi,n,l+1}^{s,p+2,q+1}+\Pi_{\xi,n,l+1}^{s,p+1,q+2}\right)-\left(3r_1+3r_2-1\right)\Pi_{\xi,n,l+1}^{s,p+1,q+1} \\
&+r_2\Pi_{\xi,n,l+1}^{s,p,q+1}+r_1\Pi_{\xi,n,l+1}^{s,p+1,q}-\Pi_{\xi,n+1,l-1}^{s,p+1,q+1} \\
&-\left(r_1+r_2\right)\left(\Pi_{\xi,n,l}^{s,p+2,q+1}+\Pi_{\xi,n,l}^{s,p+1,q+2}\right) \\
&-\left(2-3r_1-3r_2-\frac{1}{2r_3}\right)\Pi_{\xi,n,l}^{s,p+1,q+1}-\left(r_1+\frac{1}{4r_3}\right)\Pi_{\xi,n,l}^{s,p+1,q} \\
&+\left(2+r_1+r_2-\frac{1}{2r_3}\right)\Pi_{\xi,n+1,l}^{s,p+1,q+1}+\left(\frac{1}{4r_3}-r_2\right)\Pi_{\xi,n+1,l}^{s,p,q+1} \\
&-\left(r_2+\frac{1}{4r_3}\right)\Pi_{\xi,n,l}^{s,p,q+1}+\left(\frac{1}{4r_3}-r_1\right)\Pi_{\xi,n+1,l}^{s,p+1,q}+\Pi_{\xi,n,l-1}^{s,p+1,q+1}
\end{aligned}
\qquad , \qquad (15)
$$

$$
\begin{aligned}
d = {} & \left(r_1 + r_2\right)\left(\Pi_{\xi,n,l+1}^{s,p-1,q+1} + \Pi_{\xi,n,l+1}^{s,p,q+2}\right) - \left(3r_1 + 3r_2 - 1\right)\Pi_{\xi,n,l+1}^{s,p,q+1} \\
& + r_1\Pi_{\xi,n,l+1}^{s,p+1,q+1} + r_2\Pi_{\xi,n,l+1}^{s,p,q} - \left(r_1 + r_2\right)\left(\Pi_{\xi,n,l}^{s,p-1,q+1} + \Pi_{\xi,n,l}^{s,p,q+2}\right) \\
& - \left(2 - 3r_1 - 3r_2 - \frac{1}{2r_3}\right)\Pi_{\xi,n,l}^{s,p,q+1} + \left(\frac{1}{4r_3} - r_1\right)\Pi_{\xi,n+1,l}^{s,p+1,q+1} - \\
& \left(r_1 + \frac{1}{4r_3}\right)\Pi_{\xi,n,l}^{s,p+1,q+1} + \left(2 + r_1 + r_2 - \frac{1}{2r_3}\right)\Pi_{\xi,n+1,l}^{s,p,q+1} + \Pi_{\xi,n,l-1}^{s,p,q+1} \\
& + \left(\frac{1}{4r_3} - r_2\right)\Pi_{\xi,n+1,l}^{s,p,q} - \Pi_{\xi,n+1,l-1}^{s,p,q+1} - \left(r_2 + \frac{1}{4r_3}\right)\Pi_{\xi,n,l}^{s,p,q}
\end{aligned}
, \tag{16}
$$

where $r_1 = \dfrac{\Delta x c \Delta t}{4\Delta y^2}, r_2 = \dfrac{\Delta x c \Delta t}{4\Delta z^2}, r_3 = \dfrac{\Delta x}{4c\Delta t}$.

It can be found from (10) that the unknowns can be obtained directly by using the AGE scheme without solving any matrix equations. Therefore, it can achieve the highest computational efficiency.

The Crank-Nicolson scheme is unconditionally stable and it has second order accuracy. The ADI-PE method can be derived directly from the CN-PE method by adding $r_y r_z \delta_y \delta_z / (4ik)^2$ to each side of the equation. In this way, the ADI-PE is also unconditionally stable with second order accuracy as the CN-PE. The AGE method is explicit, second-order accurate, and is unconditionally stable because of using alternative strategies on the boundary grids.

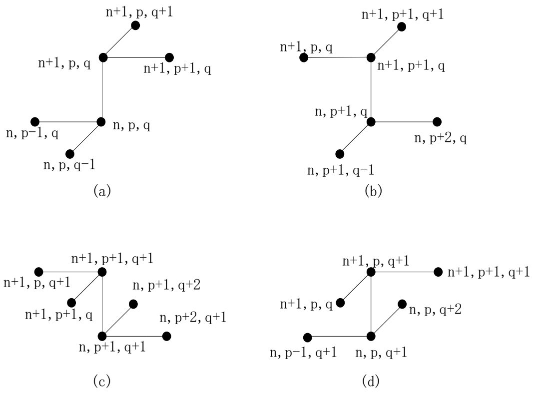

Fig. 1. Four asymmetry schemes for AGE scheme.

III. NUMERICAL EXAMPLES

At first, we consider the transient EM scattering from a PEC sphere with the radius of 5 m. The center frequency of the modulated Gaussian pulse is 300 MHz and its bandwidth is 600 MHz. In this numerical example, the range steps are set to be 0.05 m and there are 800 time steps are needed. The incident wave is fixed at $\theta_{inc} = 90^\circ, \varphi_{inc} = 0^\circ$. As shown in Fig. 2, the forward bistatic RCS results of the CN-Claerbout-TDPE, the ADI-Claerbout-TDPE and the AGE-Claerbout-TDPE at different frequencies are given and compared with the Mie Series. It can be seen that the accuracy can be ensured at the angles of 25°-30° along the paraxial direction. Moreover, as shown in Fig. 3, the transient forward-scattered field of the proposed method is compared with the results for the inverse discrete Fourier transform (IDFT) of the Mie Series. Furthermore, the computational resources are compared in Table 1 among the CN-TDPE, the CN-Claerbout-TDPE, the ADI-TDPE, the ADI-Claerbout-TDPE, the AGE-TDPE and the AGE-Claerbout-TDPE methods. It can be concluded that accurate results can be obtained at wider angles with less computational resources by the proposed AGE-Claerbout-TDPE method than other methods.

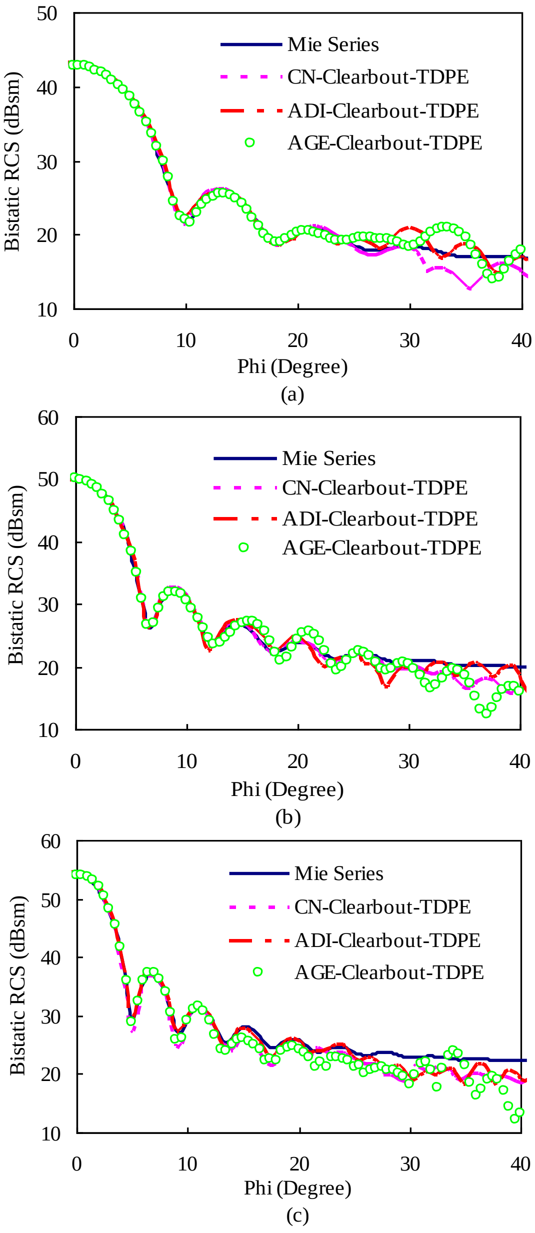

Fig. 2. Bistatic RCS of a PEC sphere: (a) 200 MHz, (b) 300 MHz, and (c) 400 MHz.

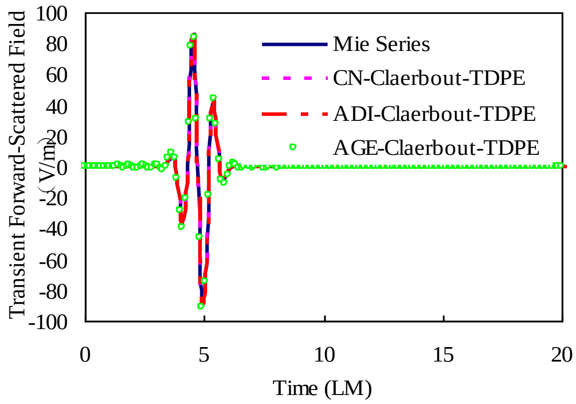

Fig. 3. Transient forward-scattered fields for the PEC sphere.

Table 1: Comparisons of the computational resources for the PEC sphere among different methods

Methods	Number of Discrete Grid	Peak Memory Requirement (MB)	Total CPU Time (s)
CN-TDPE	120*120*120	411	12928
CN-Claerbout-TDPE	120*120*120	487	14432
ADI-TDPE	120*120*120	325	1079
ADI-Claerbout-TDPE	120*120*120	647	1343
AGE-TDPE	120*120*120	335	326
AGE-Claerbout-TDPE	120*120*120	396	394

Secondly, the transient EM scattering from a PEC satellite is analyzed with the incident wave fixed at $\theta_{inc} = 180^\circ, \varphi_{inc} = 0^\circ$. The center frequency of the modulated Gaussian pulse is 300 MHz and its bandwidth is 600 MHz. The range steps are 0.05 m and there are 600 time steps are needed in this example. As shown in Fig. 4, the complete RCS result of the proposed AGE-Claerbout-TDPE method is compared with the FEKO. It should be noted that the complete RCS result is obtained by five rotating AGE-Claerbout-TDPE runs. There is a good agreement between them. Moreover, as shown in Fig. 5, the stability tests are made for the proposed three solutions. Figure 5 shows that the magnitudes of reduced time-domain scattered fields at the top point of the satellite attenuate exponentially to 1.E-5 V/m. It can be observed that the stability can be guaranteed of the three solutions for $\Delta t = 1/c\sqrt{(1/\Delta x)^2 + (1/\Delta y)^2 + (1/\Delta z)^2}$.

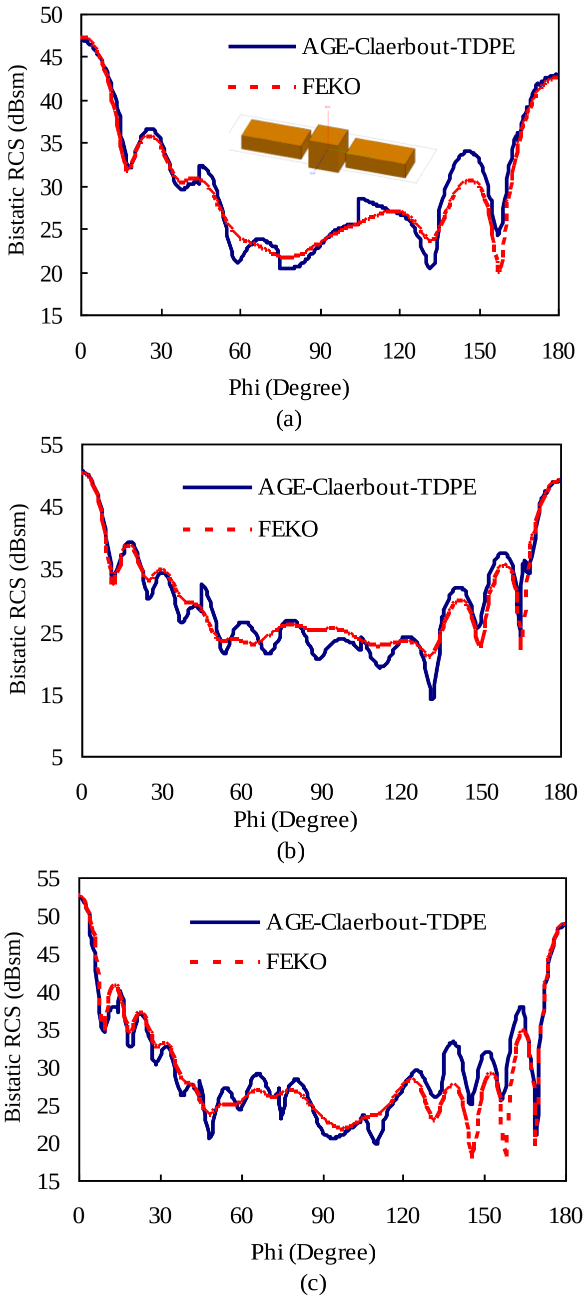

(a)

(b)

(c)

Fig. 4. Bistatic RCS of a PEC satellite: (a) 200 MHz, (b) 300 MHz, and (c) 400 MHz.

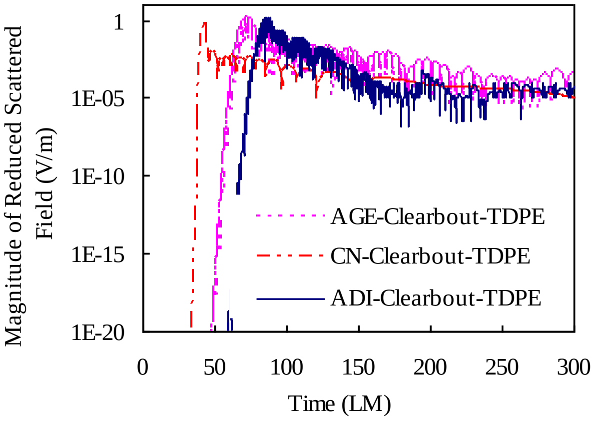

Fig. 5. Stability tests for the PEC satellite among the CN, ADI and AGE solutions.

IV. CONCLUSION

In this paper, a novel wide-angle Claerbout scheme of three-dimensional time domain parabolic equation (Claerbout-TDPE) is proposed to analyze the wide-band EM scattering problems. It can provide accurate bistatic RCS results at wider angle than the traditional TDPE, which is up to 25° along the paraxial direction. The CN, ADI and AGE schemes are used to solve the Claerbout-TDPE and efficiency tests are made among them. Furthermore, the complete bistatic RCS results can be achieved by several rotating Claerbout-TDPE runs.

ACKNOWLEDGEMENT

This work was supported in part by Natural Science Foundation of 61701232, Jiangsu Province Natural Science Foundation of BK20170854, the China Postdoctoral Science Foundation, the Fundamental Research Funds for the central Universities of No. 30917011317, and the State Key Laboratory of Millimeter Waves of K201805.

REFERENCES

[1] A. E. Barrios, “A terrain parabolic equation model for propagation in the troposphere,” *IEEE Trans. Antennas and Propagation*, vol. 42, no. 1, pp. 90-98, 1994.

[2] S. Mckee, D. P. Wall, and S. K. Wilson, “An alternating direction implicit scheme for parabolic equations with mixed derivative and convective terms,” *J. Computat. Phys.*, vol. 126, no. 0120, pp. 64-76, 1996.

[3] R. Martelly and R. Janaswamy, “Modeling radio transmission loss in curved, branched and rough-walled tunnels with the ADI-PE method,” *IEEE Trans. Antennas and Propagation*, vol. 58, no. 6, pp. 2037-2045, 2010.

[4] A. A. Zaporozhets and M. F. Levy, “Bistatic RCS calculations with the vector parabolic equation method,” *IEEE Trans. Antennas and Propagation*, vol. 47, no. 11, pp. 1688-1696, 1999.

[5] M. F. Levy and P. P. Borsboom, “Radar cross-section computations using the parabolic equation method,” *Electron. Lett.*, vol. 32, pp. 1234-1236, 1996.

[6] Z. He and R. S. Chen, “A novel parallel parabolic equation method for electromagnetic scatterings,” *IEEE Trans. Antennas and Propagation*, vol. PP, no. 99, pp. 1-1. (early access).

[7] M. F. Levy, *Parabolic Equation Methods for Electromagnetic Wave Propagation*, London: The Institution of Electrical Engineers, 2000.

[8] Z. He and R. S. Chen, “A vector meshless parabolic equation method for three-dimensional electromagnetic scatterings,” *IEEE Trans. Antennas and Propagation*, vol. 63, no. 6, pp. 2595-2603, 2015.

[9] Z. He, Z. H. Fan, and R. S. Chen, “Spectral element method based parabolic equation for EM scattering problems,” *Waves in Random and Complex Media*, vol. 26, iss. 1, pp. 80-88, 2016.

[10] Z. He, Z. H. Fan, D. Z. Ding, and R. S. Chen, “A vector parabolic equation method combined with MLFMM for scattering from a cavity,” *Applied Computational Electromagnetics Society Journal*, vol. 30, no. 5, pp. 496-502, 2015.

[11] Z. He, T. Su, and R. S. Chen, “Vector parabolic equation method for the scattering from PEC objects in half-space,” *Applied Computational Electromagnetics Society Journal*, vol. 30, no. 8, pp. 877-883, 2015.

[12] Z. He, Z. H. Fan, D. Z. Ding, and R. S. Chen, “Efficient radar cross-section computation of electrically large targets with ADI-PE method,” *Electronics Letters*, vol. 51, no. 4, pp. 360-362, 2015.

[13] Z. He, Z. H. Fan, D. Z. Ding, and R. S. Chen, “GPU-accelerated ADI-PE method for the analysis of EM scatterings,” *Electronics Letters*, vol. 51, no. 21, pp. 1652-1654, 2015.

[14] W. L. Siegmann, G. A. Kriegsmann, and D. Lee, “A wide-angle three-dimensional parabolic wave equation,” *J. Acoust. Soc. Am.*, vol. 78, no. 2, pp. 659-664, 1985.

[15] Z. X. Huang , B. Wu, W. Sha, M. S. Chen, X. L. Wu, and H. Dai, “High-order parabolic equation method for electromagnetic computation,” *APMC 2008, Asia-Pacific*, 2008.

[16] M. D. Collins, “Generalization of the split-step Pade solution,” *J. Acoust. Soc. Am.*, vol. 96, iss. 1, pp. 382-385, 1994.

[17] Z. He and R. S. Chen, “A wide-angle ADI-PE method for EM scattering from electrically large targets,” *Electromagnetics*, to be published.

[18] J. E. Murphy, “Finite-difference treatment of a time-domain parabolic equation: Theory,” *The*

Journal of the Acoustical Society of America, vol. 77, no. 5, pp. 1958-1960, 1985.

[19] A. V. Popov, V. V. Kopeikin, N. Y. Zhu, and F. M. Landstorfer, "Modeling EM transient propagation over irregular dispersive boundary," *Electronics Letters*, vol. 38, no. 14, pp. 691-692, 2002.

[20] N. Y. Zhu and F. M. Landstorfer, "Numerical modelling of pulse propagation in tunnels," *Frequenz*, vol. 62, no. 7-8, pp. 160-163, 2008.

[21] Y. Q. Yang and Y. L. Long, "Modeling EM pulse propagation in the troposphere based on the TDPE method," *Antennas and Wireless Propagation Letters*, vol. 12, pp. 190-193, 2013.

[22] Z. He and R. S. Chen, "Fast analysis of wide-band scattering from electrically large targets with time-domain parabolic equation method," *Computer Physics Communication*, vol. 200, pp. 139-146, 2016.

[23] Z. He and R. S. Chen, "A novel marching-on-in-degree solver of time domain parabolic equation for transient EM scattering analysis," *IEEE Trans. Antennas and Propagation*, vol. 64, no. 11, pp. 4905-4910, 2016.

[24] H. H. Zhang, Q. Q. Wang, Y. F. Shi, and R. S. Chen, "Efficient marching-on-in-degree solver of time domain integral equation with adaptive cross approximation algorithm-singular value decomposition," *Applied Computational Electromagnetics Society Journal*, vol. 27, no. 6, pp. 475-482, 2012.

[25] H. H. Zhang, Z. H. Fan, and R. S. Chen, "Marching-on-in-degree solver of time-domain finite element-boundary integral method for transient electromagnetic analysis," *IEEE Transactions on Antennas and Propagation*, vol. 62, no. 1, pp.319-326, 2014.

Zi He was born in Hebei, China. She received the B.Sc. and Ph.D. degrees in Electronic Information Engineering from the School of Electrical Engineering and Optical Technique, Nanjing University of Science and Technology, Nanjing, China, in 2011 and 2016, respectively. She has worked as a Visiting Scholar in the University of Illinois at Urbana and Champaign (UIUC) from September 2015 to September 2016. She works as a Postdoctor at the Science and Technology on Electromagnetic Scattering Laboratory, BIEF.

Since 2016, she has been an Assistant Professor with the Department of Communication Engineering, Nanjing University of Science and Technology. Her research interests include antenna, RF-integrated circuits, and computational electromagnetics.

Hong-Cheng Yin was born in Jiangxi, China. He received the B.S. degree from Northwest Telecommunication Engineering Institute, Xi'an, China, in 1986, the M.S. degree from Beijing Institute of Environmental Features (BIEF), Beijing, China, in 1989, and the Ph.D. degree from Southeast University, Nanjing, China, in 1993, all in Electromagnetic Field and Microwave Technique. He is currently a Researcher at the Science and Technology on Electromagnetic Scattering Laboratory, BIEF. His research interests include numerical methods in electromagnetic fields, electromagnetic scattering and inverse scattering, radar target recognition. Yin is a Fellow of Chinese Institute of Electronics.

Ru-Shan Chen was born in Jiangsu, China. He received the B.Sc. and M.Sc. degrees from the Department of Radio Engineering, Southeast University, China, in 1987 and 1990, respectively, and the Ph.D. degree from the Department of Electronic Engineering, City University of Hong Kong, in 2001.

He joined the Department of Electrical Engineering, Nanjing University of Science and Technology (NJUST), China, where he became a Teaching Assistant in 1990 and a Lecturer in 1992. Since September 1996, he has been a Visiting Scholar with the Department of Electronic Engineering, City University of Hong Kong, first as Research Associate, then as a Senior Research Associate in July 1997, a Research Fellow in April 1998, and a Senior Research Fellow in 1999. From June to September 1999, he was also a Visiting Scholar at Montreal University, Canada. In September 1999, he was promoted to Full Professor and Associate Director of the Microwave and Communication Research Center in NJUST, and in 2007, he was appointed as the Head of the Department of Communication Engineering, NJUST. He was appointed as the Dean in the School of Communication and Information Engineering, Nanjing Post and Communications University in 2009. And in 2011 he was appointed as Vice Dean of the School of Electrical Engineering and Optical Technique, NJUST. Currently, he is a principal investigator of more than 10 national projects. His research interests mainly include computational electromagnetics, microwave integrated circuit and nonlinear theory, smart antenna in communications and radar engineering, microwave material and measurement, RF-integrated circuits, etc. He has authored or coauthored more than 260 papers, including over 180 papers in international journals.

Phase-only Synthesis Algorithm for Transmitarrays and Dielectric Lenses

Susana Loredo, Germán León, Omar F. Robledo, and Enrique G. Plaza

Department of Electrical Engineering
University of Oviedo, Gijón, E33203, Spain
loredosusana@uniovi.es, gleon@uniovi.es, uo230632@uniovi.es, egplaza@tsc.uniovi.es

Abstract ─ In this work a phase-only synthesis algorithm is applied for the design of lens-array antennas yielding a desired radiation pattern. The potential relevance of spillover effect on the lens radiation pattern is illustrated, making it necessary to include it in the lens model and to take it into account in the synthesis algorithm. Thus, both the contribution of the lens and the spillover radiation are jointly modeled as a planar array. Moreover, in order to validate the algorithm, it has been applied to the synthesis of pixelated dielectric lenses, which have been simulated using a commercial software. Simulations show good agreement with the algorithm results, validating its use for this type of lenses.

Index Terms ─ Antenna array synthesis, dielectric antennas, lens antennas, transmitarrays.

I. INTRODUCTION

Planar lens-array antennas, also called transmitarrays, consist of a quasi-periodical planar array of printed radiating elements configured to yield a phase distribution that exhibits a collimating effect while ideally transmitting all the incident power [1-4]. Then, in order to achieve a desired radiation pattern, a phase-only synthesis algorithm must be applied to find the necessary phase distribution on the lens surface. Furthermore, the spillover radiation, which propagates in the same region as the radiation from the lens, may affect the antenna behavior. Consequently, the spillover radiation should be calculated and included in the synthesis algorithm and then taken into account to obtain the radiation pattern of the whole system consisting of the lens and the feeding element.

Many different synthesis algorithms have been proposed in the literature, some of them very costly both in time and computational resources. However, the algorithm presented in [5, 6] for the synthesis of low sidelobe radiation patterns is very simple and fast. It is based on the iterative application of direct and inverse fast Fourier transforms, and results are given both for amplitude-only and complex weighted synthesis. In this work that algorithm will be applied to the phase-only synthesis of the radiation pattern of a planar lens-array fed by a horn antenna. The desired pattern will be specified by two given masks defining the characteristics of both the main lobe and the sidelobe level, so more restrictions are imposed on the algorithm convergence. Moreover, the effect of spillover radiation will be included in the synthesis algorithm.

Finally, in this work it will also be proved that the proposed synthesis algorithm can be applied to the design of dielectric lenses consisting of variable height elements. Dielectric reflectarray and lens antennas have been recently proposed as low-loss, low-cost solutions, based on 3D printing technology, for millimeter-wave and terahertz antennas [7, 8].

II. PROPOSED APPROACH

A. System model

The whole antenna system consists of a feeding horn and the planar lens-array, as shown in [9]. The feed is placed at a distance F from the lens pointing at its center and it is modeled as a $cos^q\theta$ function. The lens elements are disposed in a rectangular regular grid made up of M_l by N_l elements, as shown in Fig. 1. In this figure, the shadowed area represents the lens, so the dots inside this area represent the lens elements, which are assumed to be isotropic. The field radiated by the feed impinges on these elements, which will modify the incident phase in order to achieve the desired far-field pattern. However, a part of the power radiated by the feed does not impinge on the lens surface since it is radiated at directions beyond the limits of the lens, although it will contribute to the final pattern and will distort it. Then, it is necessary to estimate its effect and include it in the synthesis process. Hence, the incident field from the horn will also be captured in a regular discrete mesh around the lens, represented by the dots outside the shadowed area in Fig. 1. They may be considered as *virtual array elements* following the same regular grid defined for the lens. Therefore the joint effect of the lens-array and the spillover radiation can be modeled as an *equivalent lens-array* of $M_s \times N_s$ elements, with $M_s = M_l + 2\Delta M$ and $N_s = N_l + 2\Delta N$.

Consequently the array factor (AF) would then be given by:

Submitted On: June 20, 2017
Accepted On: November 29, 2017

$$AF(u,v)=\sum_{m=1}^{M_s}\sum_{n=1}^{N_s} I_{mn}\, e^{j\beta d((m-1)u+(n-1)v)}, \tag{1}$$

where I_{mn} are the complex excitations at the elements of the *equivalent lens-array*, λ is the wavelength, $\beta = 2\pi/\lambda$, d is the element spacing, $u = sin\theta cos\phi$, and $v = sin\theta sin\phi$, being (θ,ϕ) the elevation and azimuth angles respectively that define the far-field direction where the AF is being evaluated.

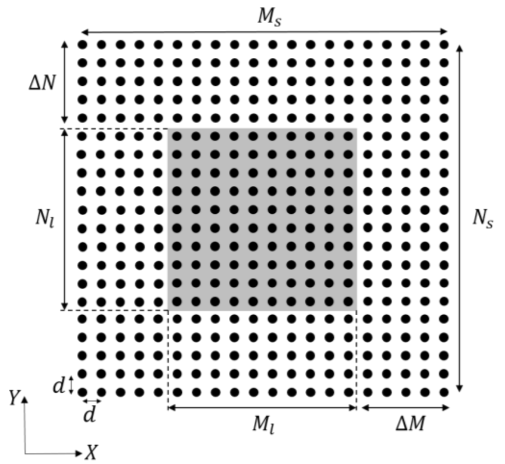

Fig. 1. Scheme of the lens-array model including spillover radiation: *equivalent lens-array*.

This model has been investigated in [9] for transmitarray antennas, comparing it with a Finite Element Method and setting the limits within which it can be used.

B. Pattern synthesis

The synthesis approach presented in [5, 6] is based on the well-known property that the AF of an antenna array having uniformly spaced elements is the inverse Fourier transform of the array element excitations. Then a direct Fourier transform relationship exists between the element excitations and the AF.

The synthesis procedure starts by defining an initial set of excitations for the array elements. The feed far field, according to the $cos^q\theta$ model, will be given by the following expression:

$$\vec{E}_F = j\frac{ke^{-jkr}}{2\pi r}\left[A_E\hat{\theta} + B_H\hat{\phi}\right], \tag{2}$$

where

$$A_E = C_E(\theta)cos\phi, \quad B_H = -C_H(\theta)sin\phi, \tag{3}$$

for an X-polarized feed, and

$$A_E = C_E(\theta)sin\phi, \quad B_H = C_H(\theta)cos\phi, \tag{4}$$

for an Y-polarized feed, with

$$C_E(\theta) = cos^{qE}(\theta), \tag{5}$$

$$C_H(\theta) = cos^{qH}(\theta). \tag{6}$$

For an axial symmetric radiation pattern $qE = qH = q$. The feed field given by (2) must then be expressed in Cartesian coordinates (E_{Fx},E_{Fy},E_{Fz}) and transformed to the lens coordinate system (E_{Lx},E_{Ly},E_{Lz}) [10]. As a result, the incident tangential electric field on the lens surface ($\vec{E}_L$) is given by:

$$\begin{pmatrix} E_{Lx} \\ E_{Ly} \end{pmatrix} = \begin{pmatrix} cos\alpha & sin\alpha \\ -sin\alpha & cos\alpha \end{pmatrix} \cdot \begin{pmatrix} E_{Fx} \\ E_{Fy} \end{pmatrix}, \tag{7}$$

with $\alpha = 0°$ in case of an X-polarized feed and $\alpha = 90°$ for Y-polarization. Expression (7) gives the initial value (I_o) for the amplitude and phase of the *equivalent lens-array* excitations:

$$(I_0)_{mn} = \left|\vec{E}_L(x_m,y_n)\right| e^{jarg\{\vec{E}_L(x_m,y_n)\}}, \tag{8}$$

being (x_m,y_n) the coordinates of the element (m,n).

For this initial set of the excitations the AF is calculated through a 2-D inverse fast Fourier transform (IFFT) of $K \times K$ points, with $K > M_s, N_s$. The obtained AF is then compared to the masks that define the desired array pattern and those AF values that do not fulfill the specifications are corrected by assigning them a new value into the specified limits.

Applying a 2D fast Fourier transform (FFT) to the corrected AF, the necessary set of element excitations is obtained. It consists of $K \times K$ samples, of which $M_s \times N_s$ correspond to the *equivalent lens-array*, so the extra samples are removed. After this, the remaining set of excitations $(I_1)_{mn}$ consists of:

1) $M_l \times N_l$ samples corresponding to the elements of the lens-array. The amplitude of these excitations is restored to its initial value, since only the phase is allowed to change:

$$|I_1|_{mn} = |I_0|_{mn} \quad \text{for} \begin{cases} \Delta M + 1 \le m \le \Delta M + M_l \\ \Delta N + 1 \le n \le \Delta N + N_l \end{cases}. \tag{9}$$

2) The samples corresponding to the spillover radiation. They are restored to its initial value, both amplitude and phase, since no synthesis can be applied on the spillover radiation:

$$(I_1)_{mn} = (I_0)_{mn} \quad \text{for} \begin{cases} 1 \le m \le \Delta M \\ \Delta M + M_l + 1 \le m \le M_s \\ 1 \le n \le \Delta N \\ \Delta N + N_l + 1 \le n \le N_s \end{cases}. \tag{10}$$

The IFFT is then applied to this new set of excitations, repeating iteratively the process until specifications are met or the maximum number of iterations is reached.

C. Effect of spillover radiation

Before applying the proposed algorithm to the synthesis of different patterns, an example will be shown in order to illustrate the effect of the spillover radiation and the convenience of including it into the synthesis algorithm. Let us consider a lens of 22×22 elements at the frequency of 16 GHz, being the separation between elements $d = 0.5\lambda$. The feed is modeled with $q = 5$, and the F/D ratio is 0.7 (being D the side length of the lens), resulting in an illumination tapper of -10 dB.

The pattern to be synthesized is a flat-top beam one with a ripple of 1 dB and sidelobe level under -18 dB. Initially the synthesis algorithm will not take into account the spillover radiation, that is $\Delta M = \Delta N = 0$, and the synthesis will be applied only on the lens-array elements. Then after each iteration a new set of $M_l \times N_l$ samples are obtained, which are treated as indicated in (2), keeping the synthesized phases and maintaining the initial values for the amplitudes. The pattern obtained with the resulting phase excitations, once the algorithm has converged, is shown in Fig. 2 (*synthesis w/o sp*). It can be observed that it fits into the specifications.

However, in order to prove the relevance of spillover radiation, its effect is added ex-post. After performing the phase synthesis on the lens elements, an *equivalent lens-array* is defined with $\Delta M = 0.5 M_l$, $\Delta N = 0.5 N_l$. The excitations of the elements representing the spillover radiation are given by the feed illumination, whereas the phases of the lens elements are the ones obtained with the synthesis algorithm, which did not have into account the spillover. Fig. 2 shows how the initial pattern (*synthesis w/o sp*) is distorted when the spillover effect is added (*synthesis w/o sp + sp*), showing the existence of side lobes that exceed the limit imposed by the mask. With this system configuration, spillover effects on the far-field pattern should be expected for values of θ greater than approximately 36º, since the maximum incidence angle on the lens surface is given by $tan^{-1}(0.5D/F)$. The appearance of these higher level lobes for $u, v > 0.6$ agrees well with this estimation.

To validate these results a dielectric lens was designed from the phase synthesis results, following a process similar to the one described in [7]. The design of the dielectric lens can be viewed as an array of dielectric slabs with different heights, which will depend on the aperture. Furthermore, in order to minimize the shadowing effects, the elements with maximum height should be placed at the center of the lens. Therefore it may be necessary to add a phase constant to the original phase provided by the synthesis algorithm.

This lens was simulated with FEKO software [11] using Geometrical Optics (GO) approximation. A dielectric lens has been chosen because GO analysis of the dielectric lens is much faster than full-wave simulation of a transmitarray. Furthermore, dielectric lenses have gained much attention due to their simple manufacture with current 3D printing technology and their potential suitability for mm-wave and terahertz frequencies [7, 8]. The simulation results are also included in Fig. 2 (*GO simulation*), presenting also important side lobes around the mentioned angles. This proves the need of including the spillover effect in the synthesis process.

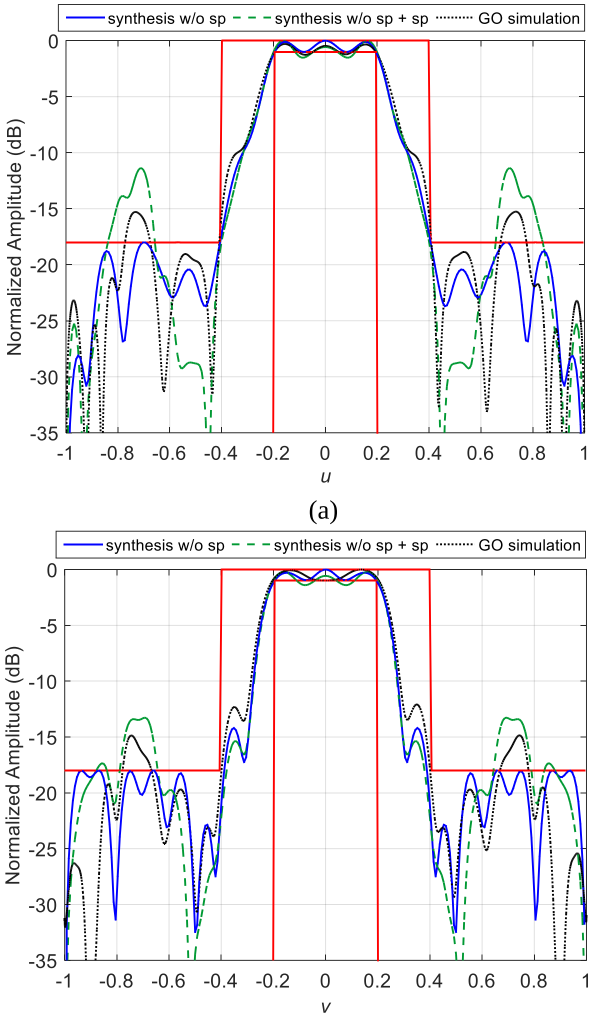

(a)

(b)

Fig. 2. Effect of spillover radiation. Main cuts for (a) $v = 0$, (b) $u = 0$.

III. RESULTS

Once the effect of the spillover in the lens radiation pattern has become evident, the same pattern will be now synthesized taking that effect into account. For that, ΔM and ΔN have been chosen to be $0.5 M_l$ and $0.5 N_l$ respectively, resulting in $M_s = N_s = 44$. In order to set the value of ΔM and ΔN, a study was carried out to analyze the effect of varying the size of the plane where the incident field from the feed is captured outside the lens-array. Then, for a given lens-array, the radiation pattern of the *equivalent lens-array* has been obtained for different sizes of the spillover grid. Some variations on the results were observed when increasing the size until reaching an illumination tapper of -32 dB on the edge of the *equivalent lens-array*. From there, no significant differences were appreciated when increasing the number of points on the spillover grid. For the example under study, the illumination on borders of the 44×44 *equivalent lens-array* is -31 dB relative to the illumination on the center of the lens.

Figure 3 shows the radiation pattern obtained once the algorithm has converged. Direct and inverse FFTs of 256×256 points were used and 977 iterations were needed so that-all far field directions fulfilled the masks, taking 22.5 seconds in a personal laptop with no special features. The necessary phase distribution on the lens surface is represented in Fig. 4 (a). With this new synthesized phase, after adjusting it as commented in Section II, a new dielectric lens was designed and simulated with FEKO. The resulting lens is depicted in Fig. 4 (b). Since a planar array model is being considered, the phase range of the dielectric lens has been limited to 360 degrees in order to have a quasi-planar lens and ensure the viability of the model. The results of the synthesis model and the simulation of the dielectric lens are compared in Fig. 5. Both patterns are very similar and fit well into the limits given by the masks, proving that the effect of the spillover radiation has been efficiently corrected. Similar results could have been obtained with different lens sizes, even smaller than the analyzed here. Simulations carried out in this study showed that the smallest lens to obtain this pattern should have 14×14 elements if $q = 5$ or 12×12 elements for $q = 10$. Both the value of q used in the feed model and the constraints imposed by the desired pattern will impact on the necessary number of array elements and also on the number of iterations needed for convergence.

The proposed algorithm was also applied to the synthesis of an isoflux pattern. In this case, the lens was made up of 38×38 unit cells, also with a periodicity of 0.5λ at the frequency of 16 GHz, and the feed was modeled with $q = 10$. The F/D ratio was kept at 0.7, and $\Delta M = \Delta N = 0.5M_l$, turning out in an illumination tapper of -20 dB on the lens-array and -52 dB on the *equivalent lens-array*. Figure 6 shows both the synthesized phase and the dielectric lens designed to validate the model with GO simulation. The 3D pattern obtained with the synthesis algorithm can be seen in Fig. 7. This result required 300 iterations, also with $K = 256$, and a computing time of 7.5 seconds. One of the main cuts is compared with the dielectric lens simulation in Fig. 8, showing a great concordance and good fulfilment of specifications. There is only a small discrepancy between the algorithm and the simulation since the slope of the main beam for the simulated dielectric lens is not as vertical as required between -10 and -15 dB.

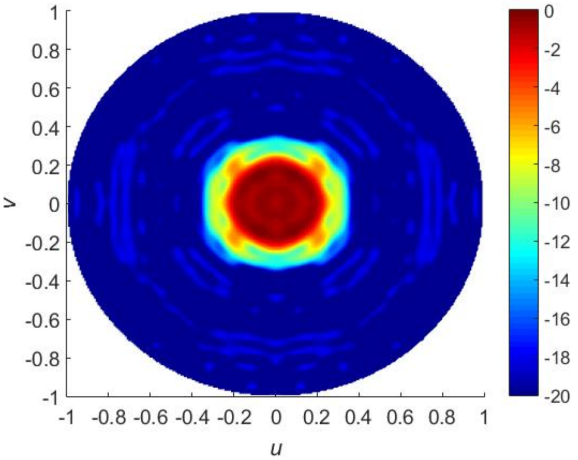

Fig. 3. 3D flat-top beam pattern obtained from phase-only synthesis algorithm.

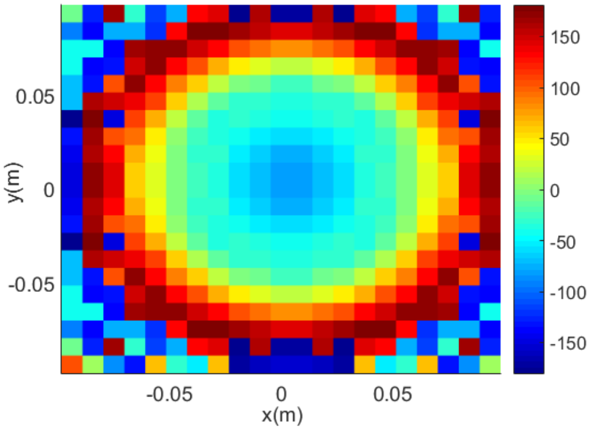

(a)

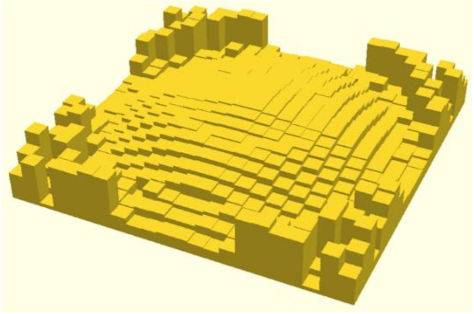

(b)

Fig. 4. (a) Synthesized phases, and (b) 3D model of dielectric lens for the flat-top beam pattern.

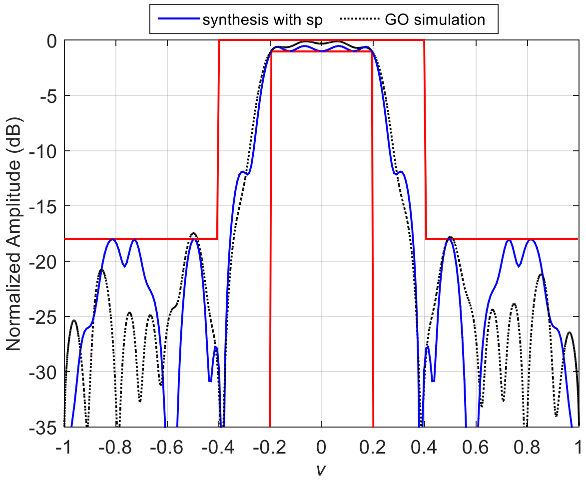

Fig. 5. Cut $u = 0$ for flat-top beam pattern.

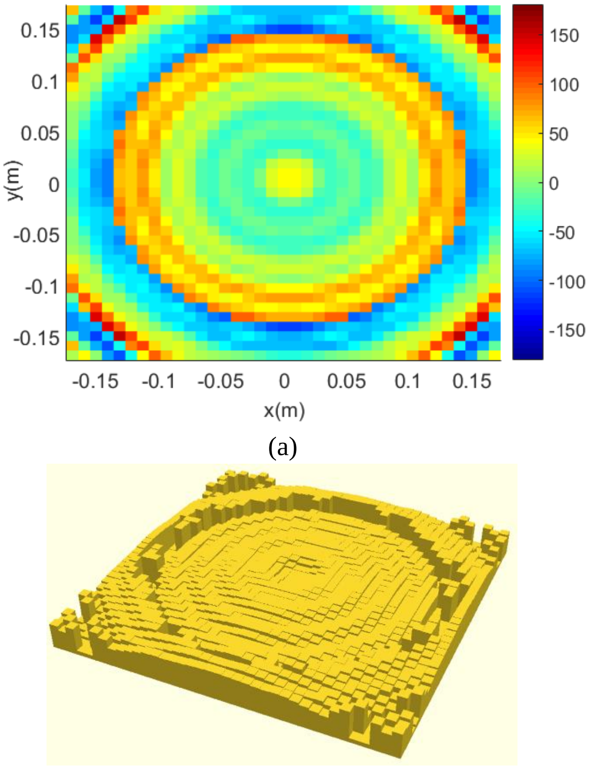

(a)

(b)

Fig. 6. (a) Synthesized phases, and (b) 3D model of dielectric lens for the isoflux pattern.

IV. CONCLUSION

A simple and fast phase-only synthesis algorithm has been proposed for the synthesis of lens-array antennas. The algorithm includes the effect of the spillover radiation, modeling the joint effect of the lens-array and the spillover as an *equivalent lens-array*, and applying iteratively the Fourier transform techniques to obtain the radiation pattern due to both contributions. In order to have the spillover appropriately modelled, the size of the spillover grid must be chosen to produce an illumination tapper lower than -30 dB on the edge of the *equivalent lens-array*.

The algorithm is based on a planar aperture model of the lens and is then valid for the design of transmitarray antennas yielding a desired radiation pattern. Furthermore, in this work it has been shown that its use can be extended to the synthesis of pixelated dielectric lenses, made up of square dielectric slabs of variable height, as long as the phase range is limited to 360 degrees so that the lens can be considered quasi-planar. The comparison of algorithm results and GO simulations of dielectric lenses shows both the efficiency of the algorithm to achieve the desired pattern and the good agreement of simulations with the algorithm results. Small discrepancies may be attributed to diffraction and shadowing effects on the dielectric lens.

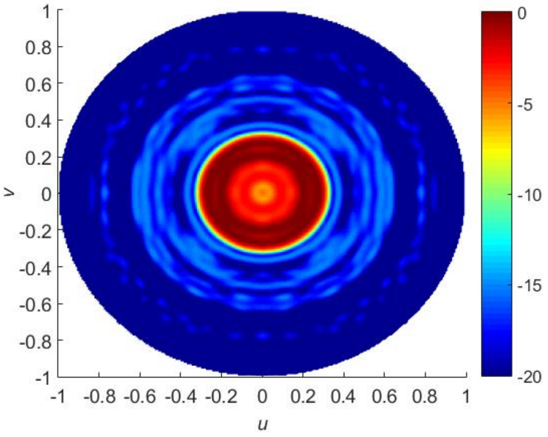

Fig. 7. 3D isoflux pattern obtained from phase-only synthesis algorithm.

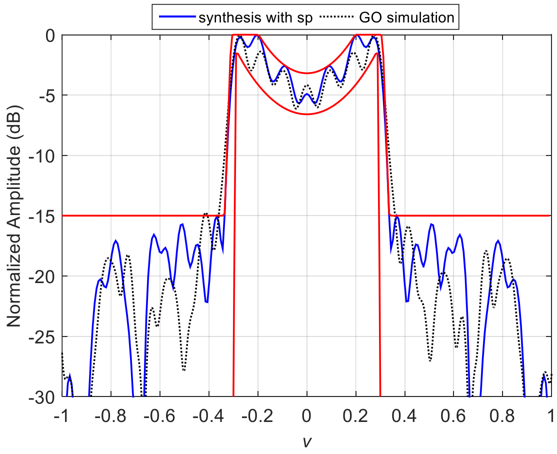

Fig. 8. Cut $u = 0$ for isoflux pattern.

ACKNOWLEDGMENT

This work was supported in part by the Ministerio de Economía y Competitividad, under project TEC2017-86619-R (ARTEINE), and by the Gobierno del Principado de Asturias/FEDER under project GRUPIN14-114.

REFERENCES

[1] J. Thorton and K.-C. Huang, *Modern Lens Antennas for Communications Engineering*, Wiley-IEEE Press, Hoboken, New Jersey, 2013.

[2] C. G. M. Ryan, M. R. Chachamir, J. Shaker, J. R. Bray, Y. M. M. Antar, and A. Ittipiboon, “A wideband transmitarray using dual-resonant double square rings,” *IEEE Trans Antennas Propagat*., vol. 58, no. 5, pp. 1486-1493, May 2010.

[3] S. Zainud-Deen, S. Gaber, H. Malhat, and K. Awadalla, “Single feed dual-polarization dual-band transmitarray for satellite applications,” *ACES Journal*, vol. 29, no. 2, pp. 149-156, Feb. 2014.

[4] L. Di Palma, A. Clemente, L. Dussopt, R. Sauleau, P. Potier, and P. Pouliguen, “Circularly-polarized reconfigurable transmitarray in Ka-band with beam scanning and polarization switching capabilities,” *IEEE Trans. Antennas Propagat*., vol. 65, no. 2, pp. 529-540, Feb. 2017.

[5] W. P. M. N. Keizer, “Low sidelobe pattern synthesis using iterative Fourier techniques code in MATLAB,” *IEEE Antennas Propag. Mag*., vol. 51, no. 2, pp. 137-150, Apr. 2009.

[6] W. P. M. N. Keizer, “Fast low-sidelobe synthesis for large planar array antennas utilizing successive fast Fourier transforms of the array factor,” *IEEE Trans. Antennas Propagat*., vol. 55, no. 3, pp. 715-722, Mar. 2007.

[7] P. Nayeri, M. Liang, R. A. Sabory-García, M. Tuo, F. Yang, M. Gehm, H. Xin, and A. Z. Elsherbeni, “3D printed dielectric reflectarrays: Low-cost high-gain antennas at sub-millimeter waves,” *IEEE Trans. Antennas Propagat*., vol. 62, no. 4, pp. 2000-2008, Apr. 2014.

[8] H. Yi, S.-W. Qu, K.-B. Ng, C. H. Chan, and X. Bai, “3D printed millimeter-wave and terahertz lenses with fixed and frequency scanned beam,” *IEEE Trans. Antennas Propagat*., vol. 64, no. 2, pp. 442-449, Feb. 2016.

[9] E. G. Plaza, G. León, S. Loredo, and F. Las-Heras, “A simple model for analyzing transmitarray lenses,” *IEEE Antennas Propag. Mag*., vol. 57, no. 2, pp. 131-144, Apr. 2015.

[10] Y. Rahmat-Samii, “Useful coordinate transformations for antenna applications,” *IEEE Trans. Antennas Propagat*., vol. AP-27, no. 4, pp. 571-574, July 1971.

[11] FEKO, ver. 7.0, EM Software & Systems-S.A., Stellenbosch, South Africa, 2014.

Susana Loredo received the M.Sc. and Ph.D. degrees in Telecommunication Engineering in 1997 and 2001 respectively, both from University of Cantabria, Spain. In 2001 she joined the Department of Electrical Engineering, University of Oviedo, first as a Research Scientist, and since 2007 as an Associate Professor.

Her research activity in recent years includes radio channel characterization, wireless communications (MIMO systems, vehicular communications), and techiques for echo cancellation and reconstruction of antenna patterns measured in non-anechoic environments. Her interest is now focused on the design of planar lenses and their application to imaging and detection at microwave and millimeter frequencies.

Germán León was born in Alcázar de San Juan, Spain. He received the M.Sc. degree and Ph.D. degree in Physical Sciences, from Universidad de Sevilla, Spain, in 1998 and 2005 respectively. In 2005, he joined the Department of Electrical Engineering, Universidad de Oviedo, Gijón, Spain, as an Associate Professor. His research interests are centered on planar lenses, near-field focusing antennas and their applications to imaging and detection.

Omar F. Robledo received his B.Sc. degree in Telecommunication Engineering from University of Oviedo, Spain, in 2016 and he is now pursuing his M.Sc. degree. His research activity is focused on synthesis algorithms for planar arrays with application to the design of planar lenses.

Enrique G. Plaza was born in Oviedo in 1988. He received his M.Sc. and Ph.D. degrees in Telecommunication Engineering at University of Oviedo in 2012 and 2017 respectively. His main research interests are the design and analysis of planar lenses and their use in imaging and detection applications.

Determination of Physical Properties of Concrete by Using Microwave Nondestructive Techniques

Murat Ozturk [1], Umur K. Sevim [1], Oguzhan Akgol [2], Emin Unal [2], and Muharrem Karaaslan [2]

[1] Department of Civil Engineering
Iskenderun Technical University, Hatay, 31200, Turkey
murat.ozturk@iste.edu.tr, ukorkut.sevim@iste.edu.tr

[2] Department of Electrical Engineering
Iskenderun Technical University, Hatay, 31200, Turkey
oguzhan.akgol@iste.edu.tr, muharrem.karaaslan@iste.edu.tr, emin.unal@iste.edu.tr

Abstract ─ Determination of the electrical properties of concretes with different water/cement ratios and investigation of the relationship between their electrical and mechanical properties is a promising technique towards improving novel nondestructive microwave based methods. In this study, this relationship between water-cement ratios/mechanical properties and electrical characteristics of various concretes is investigated in the frequency range of 3-18 GHz. The obtained data provides an accurate measurement results for the researchers to design microwave sensors operating at a constant frequency. Besides, the relationship between the electrical properties and the pressure applied to the concrete is also investigated experimentally for various cement types. The experimental study demonstrates the presumable mechanical characteristic of the concrete by using its dielectric constant values. The dielectric constant is retrieved from the reflection and transmission coefficients (which are more commonly known as scattering parameters) by using Nicolson Ross Weir (NRW) Technique. It is revealed that the most significant frequency point is 18 GHz to determine water/cement ratio and 17 GHz to differentiate applied pressure level by using dielectric constant values of the concrete.

Index Terms ─ Concrete, electromagnetic, Nicolson-Ross Weir, nondestructive testing.

I. INTRODUCTION

Concrete is one of the most commonly used materials in the construction industry. Cement powder, water, fine aggregate (sand), coarse aggregate (rocks) and air (porosity) are composition of concrete which is a heterogeneous material. Aggregate used in concrete is an inert filler material while the chemical reactions between cement powder and water generate a paste binder that holds filler materials together.

Detection of the aging and examining concrete effectively is possible by using nondestructive test (NDT) and nondestructive evaluation (NDE) techniques. These techniques are used for monitoring damages or examining the quality control of concretes [1]. In addition, NDT methods are used to predict premature collapses that the structures may have in future. Techniques and application of these methods are studied by various researchers [1,2].

Moisture content, cracks, voids etc. can be determined by radio and microwave nondestructive testing methods [2]. Conducting these methods provides advantages over the other NDE methods (such as radiography, ultrasonic, eddy current) since they are more reliable, cheaper and easier to apply on [3]. Nowadays, microwave nondestructive testing (MNDT) techniques (such as ground probing radar, free-space microwave techniques) are effectively used for quality control of concretes. Since MNDT techniques are fast, precise and reliable, these test methods have taken an important place in the construction applications [4].

Boiset et al. [5] studied microwave near-field reflection property analysis of concrete to correlate the analysis results with the strength of concrete, which is strongly influenced by water-to-cement (w/c) and coarse aggregate-to-cement (ca/c) ratios of concretes. In the study of Zoughi et al. [5], cement paste samples with different w/c are tested under different frequency ranges in microwave spectrum. According to their results, there is a correlation between the reflection coefficients of the samples and water-cement ratios. Thus, correlation between compressive strength and the reflection coefficient of these samples is also obtained.

A time domain reflectometry (TDR) and backscattering search optimization algorithm (BSA) based nondestructive approach for wiring diagnosis is also investigated by Boudjefdjouf et al. [6]. The results of proposed technique is realized by both simulations and experiments. It is concluded that the proposed

Submitted On: December 12, 2016
Accepted On: January 3, 2018

approach can be used to determine complex wire networks. Signal inversion by using sensors is also carried out for eddy current (EC) nondestructive testing (NDT) method. The proposed technique characterizes surface cracks by using the reflected EC signals [7].

In the current study, reflection coefficients and dielectric properties of the concrete samples containing different types of cement with various water-cement ratio are determined by electromagnetic waves at microwave frequency range of 3.0–18.0 GHz and mechanical and transport properties of the samples are also examined. At the end of the study, a correlation between electrical parameters (dielectric constant) and mechanical/transport properties of the concrete samples are presented.

II. EXPERIMENTAL STUDIES

In order to characterize the electromagnetic behaviours of the concrete samples, we need to obtain the scattering parameters (also known as S-Parameters). For this purpose, a wideband Vector Network Analyzer (VNA) which is capable of measuring electromagnetic signals from 10 MHz to 43.5 GHz are used. Two wide band, linearly polarized, directional and high gain horn antennas are used by connecting VNA. Antennas have the operating frequency of 3-18 GHz which is quite enough to analyze the electromagnetic behaviors of the concretes under test. Analyzer with the antennas is used to measure transmission and reflection parameters to find the electromagnetic behavior of the concrete samples.

Nicolson Ross Weir (NRW) approach is used to determine the electromagnetic properties of the concrete samples with various w/c values [10,11] and many different types of materials [12-14]. This approach uses reflection and transmission values as well as the associated phases obtained from the network analyzer to characterize the electromagnetic response of the concrete sample. NRW method which is preferred due to its advantages on free space measurements. It is based on extracting the parameters by using two main scattering coefficients, namely the reflection from the port-1 (S11) and the transmission between port-1 and port-2 (S21) (Fig. 1). The electromagnetic parameters of any medium including the concrete samples can be extracted from the transmission and reflection values by using NRW technique. Some of these parameters are the electrical permittivity, permeability and loss factor values that we successfully obtained from experimental setup. The formulas of $\mu = \mu_0\mu_r$, $\varepsilon = \varepsilon_0\varepsilon_r$, $Z = \sqrt{\mu_r/\varepsilon_r}\,Z_0$ can be used to find magnetic permeability, dielectric constant and impedance of the medium, respectively. The details of the NRW method can be summarized for the general case as follows.

First, the reflection coefficient which is shown by Γ should be found:

$$\Gamma = \frac{Z-Z_0}{Z+Z_0} = \frac{\sqrt{\mu_r/\varepsilon_r}-1}{\sqrt{\mu_r/\varepsilon_r}+1}. \quad (1)$$

By using the sample thickness and medium parameters, wave decay (z) can be calculated for the medium inside the sample under test:

$$\mathrm{z} = \exp - \mathrm{j}\omega\sqrt{\mu\varepsilon}\mathrm{d} = \exp[-\mathrm{j}(\omega/\mathrm{c})\sqrt{\mu_r\varepsilon_r}\mathrm{d}]. \quad (2)$$

By using the parameters found so far, it can be easily written the expressions for the reflection and transmission parameters as:

$$S_{21}(\omega) = \frac{(1+\Gamma)(1-\Gamma)z}{1-\Gamma^2z^2} = \frac{(1-\Gamma^2)z}{1-\Gamma^2z^2}, S_{11}(\omega) = \frac{(1-z^2)\Gamma}{1-\Gamma^2z^2}. \quad (3)$$

While the impedance of the sample unit is:

$$Z = \pm\sqrt{\frac{(1+S_{11})^2-S_{21}^2}{(1-S_{11})^2-S_{21}^2}}. \quad (4)$$

The relative permittivity and permeability can then be calculated using the formula below:

$$\mu_r \sim \left(\frac{2}{jk_0d}\right)\frac{1-V_2}{1+V_2}, \quad (5)$$

$$\varepsilon_r \sim \left(\frac{2}{jk_0d}\right)\frac{1-V_1}{1+V_1}. \quad (6)$$

Where k denotes wave vector in MUT which is $k \sim \frac{1}{jd}\frac{(1-V_1)(1+\Gamma)}{1-\Gamma V_1}$ and V1, V2 are defined for simplification as:

$$V_1 = S_{21} + S_{11}, \quad (7)$$

$$V_2 = S_{21} - S_{11}. \quad (8)$$

It should be noted that the derivation above is for the general case of the relative permittivity and permeability calculation. The software loaded onto the analyzer will choose the appropriate parameters while using NRW method. Therefore, the distance between the testing antennas and the sample under test as well as the thickness of the sample are extremely crucial in order to obtain more accurate results.

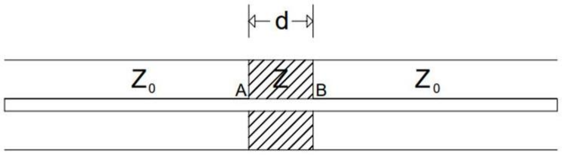

Fig. 1. Measurement configuration of S-parameters.

A. Materials and mixture proportions

An experimental analyze is conducted to determine the correlation between the effective electrical properties and mechanical/transport properties of different concrete mixtures. The materials used to prepare the concrete mixtures are portland cement, white cement, calcium alimunat cement, fine aggregate with a maximum grain size of 4mm, coarse aggregate with a maximum grain size of 16mm and tap water. The chemical composition of the portland cements used is presented in Table 1.

Table 1: Chemical composition of Portland cement

Chemical Properties	Analysis (%)
MgO	2.00
Al_2O_3	6.57
SiO_2	21.56
CaO	61.28
Fe_2O_3	3.00
SO_3	3.19
K_2O	0.69
Na_2O	0.27

The absolute volume method defined by ACI is used for mixture design. For the mixtures which contain Portland, white and calcium alimunat cement, the water-cement ratio is kept constant with a value of 0.5. In order to determine the effect of water-cement ratio, the traditional (Portland) cement containing concrete mixture is preferred as a control mixture and then samples with different w\c are produced. The details of mix proportions used in this study are given in Table 2.

Table 2: Mix design

W/C	Water (kg/m³)	Portland Cement (kg/m³)	Fine Aggregate Weight (kg) (0-4 mm)	Coarse aggregate Weight (kg) (4-11 mm)
0,4	200	500	672,39	693,79
0,5	250	500	617,39	637,04
0,6	300	500	562,39	580,29

B. Mix proportions

Five different mixtures are prepared as the material under test (MUT) with the consideration of the followings:

- Concrete mixtures containing three different cement types (Portland cement, white cement, calcium alimunat cement).
- Three different water-cement ratio for mixtures containing traditional cement (0.4, 0.5 and 0.6).

Fine and coarse aggregates are placed in concrete mixer and mixed for a minute, cement is then added and mixed for two minutes. Finally, tap water is added gradually and mixed up for the concrete to have plastic form. A speed controlled power-driven revolving pan mixer is used to mix the concrete. 15x15 cm^2 slap samples with 4 cm thickness to determine the electromagnetic (EM) behavior, 10x10x10 cm^3 cubes to conduct compressive strength, abrasion and absorption tests and 15x15x15 cm^3 cubes to perform tensile splitting and high water pressure tests are used. The mentioned dimensions are carefully selected to minimize the measurement errors and to provide adaptation for NRW limits. The correctness of the experimental results is provided by normalizing the results with respect to the results of both free space measurement in the same environment and the measurement performed by using metallic sheet between transmitter and receiver antennas. The specimens are demolded 24 hours after casting and cured in a water tank for 28 days.

C. Test methods

This study aims to determine the concrete properties of the samples with different mixtures by using a non-destructive electromagnetic based method. The proposed method retrieves the relative permittivity values from the scattering parameters, more widely known as S-parameters. These parameters characterize the reflected and transmitted electromagnetic signals between the ports. Two-port system is considered in the study. To find relationship between the mechanical characterization and the electromagnetic behaviour of the concrete samples will lead us to build various instruments including particularly microwave sensors and etc.

S-parameters can be measured by using a network analyzer within the operating frequency range of the analyzer. The instrument we have covers almost 43 GHz frequency band which is quite enough for our purpose as the results also support this statement. Although the range of the analyzer is high, it is observed that the relationship is obtained in the frequency range of 3-17 GHz. For this purpose, two linearly polarized horn antennas with very high efficiency and directivity is used in the measurement. The calibration is made by following the procedure suggested by the manufacturer which includes air for free space normalization and a metallic plate for full reflection calibration. After each calibration we have measured the testing setup for free space and no further work is done without confirming the calibration is accurate. Permittivity value of air is measured first for the calibration check and the values for air are always obtained before starting the concrete measurements. The separation distance and the sample thickness are measured and typed into the program and the corresponding subroutines tabulated the desired characteristics which will be shown in the following sections of the paper.

In case of determining the physical properties by using NRW free space method, each electromagnetic properties are determined with respect to the thickness of the samples as seen from Eq. (2), Eq. (5), Eq. (6) and Eq. (7). Hence, errors that can be occurred due to the thickness have been eliminated in the main equations. Beside this, diffraction errors are minimized by choosing the sample as large as the maximum wavelength of incident wave in the related frequency range.

The tests are conducted on 15x15 cm^2 concrete specimens with 4 cm thickness. Measurement setup and the schematic view of the experimental study is shown in Fig. 2. The measurement environment is set to minimize scattering and near field effects to enhance the accuracy of the experiments. The measurement environment should not include any other external electromagnetic wave transmitter in order to prevent any noise from the reflected and transmitted data. Therefore, all the instruments are switched off and removed from the testing area. The testing setup is prepared so that two horn antennas have the same orientation in order to measure the co-polarization measurement not the cross-polarization responses of the antennas. The separation distance between the antennas are calculated and precisely aligned so that reactive near field region effects are eliminated.

Tensile splitting tests are performed on 15x15x15 cm^3 cubes and compression tests are performed on 10x10x10 cm^3 cubes by a 1000 kN compression capacity testing machine. To conduct tensile splitting test on the cube, lines are drawn on the middle of two opposite faces of the cubes to ensure the applying load on the same axis. Two metal strips are then placed on the drawn lines. After that, approximately a 14-21kg/cm^2/minute load is applied. To estimate tensile splitting strength, Eq. (9) is used:

$$\sigma=2P/\pi a^2, \tag{9}$$

where

σ: Tensile splitting strength,
P: Load,
a: Length of the specimen.

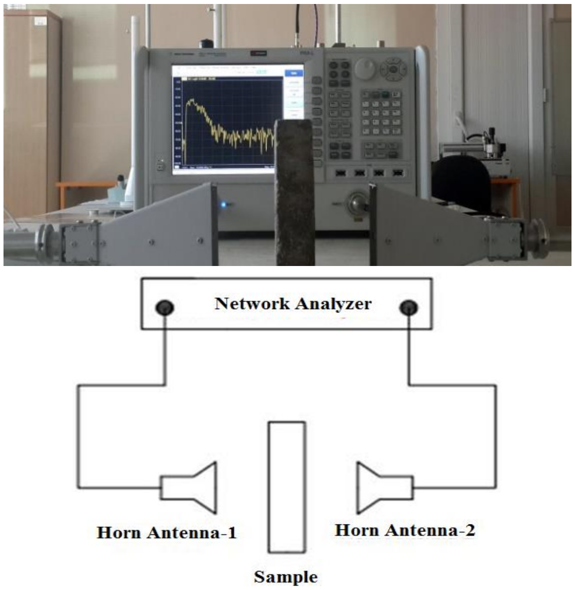

Fig. 2. Measurement setup and the schematic view.

Apart from applying a linear load in tensile splitting test to determine compressive strength of the concretes; a distributed load is also applied onto two opposite faces of the cube. To estimate compressive strength, Eq. (10) is used:

$$\sigma=P/a^2. \tag{10}$$

Determination of the abrasion resistance of the concrete, Vertical Abrasion Tester setup is used. Concretes having 10x10x10cm^3 dimensions are abbreviated by an abrasive dust. The dust is poured between the concrete sample and a metal disc, which rotates 75 times/min. For measuring abrasion amount, final (abbreviated) and first (not-abbreviated) weight of the samples are recorded. The weight difference between the final and first reading gives the abrasion resistance.

To determine water absorption capacity of the hardened concrete, 28 days water cured concrete samples are dried in an oven under the temperature of 105^oC for a day. Then, weight difference between fully saturated and oven dried concrete samples gives water absorption capacity of the concrete. For this test method, 10x10x10 cm^3 cubes are used.

High water pressure test is conducted to determine water penetration deepness of the concrete samples by applying 5 bar water pressure from bottom face. Before conducting the test procedure, concrete samples are dried in an oven under 105^oC for a day and then faces of the test specimen except top and bottom faces are coated with paraffin to control the water flow. A 5 bar water pressure is applied from bottom face of the 15x15x15 cm^3 cube samples for 72 hours. At the end of three days, the cube samples are split then the water penetration deepness is measured and recorded.

III. RESULTS AND DISCUSSIONS

Determining or predicting compressive strength of a concrete sample in terms of electrical properties provides a prediction of other mechanical and transport characteristics of the concrete under test with various properties. In order to provide this relationship, water-cement concrete mixtures with 0.4-0.5 and 0.6 ratios are prepared. The aim of the selection of these water-cement ratio values is to control compressive strengths of the samples so that the other mechanical and transport parameters would also be under control. Increasing water content in the concrete mixture causes weaker bond between cement paste and aggregates, bigger capillary pores and more heterogeneous mixture due to segregation compared to the concretes with lower water-cement ratio. Thus, as it can be seen in Table 3, higher values of w/c result in an increment in compressive strength, increase the splitting tensile strength and abrasion resistance; decrease the water absorption and high pressure water penetration.

The results of the strength and transport characteristics of the concretes containing different water content is illustrated and compared in Table 3. The prediction of compressive strength of the concrete will provide useful data to have a better idea about concrete properties for specialists.

Table 3: The relationship between mechanical properties of the concrete and water/cement ratios

Engineering Behaviors	W/C=0,4	W/C=0,5	W/C=0,6
Compressive strength (Mpa)	46,09	29,98	22,26
Splitting tensile strength (Mpa)	2,34	2,26	1,81
Abrasion resistance (weight loss (%))	0,04	0,08	0,09
Water absorption (%)	3,65	7,49	8,72
High pressure water penetration (cm)	0,5	3,5	5

In this study, both the concrete samples having different water contents and the concrete samples with different cement types are studied. Their compressive strengths and electromagnetic characteristics are tested and the results are then correlated. Each material has unique electromagnetic properties and responses when exposed to an electric field due to changing effective electromagnetic properties depending on the content of concretes. One of the parameters identifying the electromagnetic properties of a matter is the effective electrical permittivity. When electric field is applied to a material, it will interact and polarize depending on the amplitude, phase and direction of the field. Under the same condition, this parameter allows us to distinguish materials just by observing their electrical permittivity. Experimental studies are carried out by using a vector network analyzer in a significantly large frequency range between 3 GHz and 18 GHz. Two linearly polarized horn antennas with high gain and operating in the frequency range of 3-18 GHz are used in order to obtain the reflected and transmitted responses of the concrete samples.

Determination or observation of strength gaining of the concrete by using microwave test methods as a nondestructive method is carried out in this part of the study. In this respect, the effective dielectric constant values of the concrete samples with different water contents are investigated by using microwave measurement techniques at two different time lines. The measurements of the reflection and transmission coefficients and evaluation of the dielectric constant values are realized on the 28th day and in the 2nd month after casting. (The specimens are demolded 24 hours after casting and cured in a water tank for 28 days). As it is obvious in the literature that as the time passes, hydration reaction in the cement paste continues. Thus, concrete becomes denser and gains more strength [8]. The conducted studies showed that there is a correlation between the strength properties and effective dielectric constant values. As seen from Fig. 3 (a), the increment of the water/cement ratio reduces the effective dielectric constant in the entire frequency spectrum. Since the presence of water in cement reduces the effective density of the concrete, the dielectric constant reduces. The widest gap between dielectric constants occurs at the frequency of 18 GHz. The dielectric constants are 6, 2 and 0.65 for 0.4, 0.5 and 0.6 w/c ratios, respectively. Hence, a simple microwave device can be designed to determine the water content of concrete. Since, the increment of the water content in the cement decreases compressive strength and splitting tensile strength as dielectric constant, the relationship between w/c and dielectric constant can be used to estimate these two strength values. Beside this, the change of dielectric constant with respect to w/c ratio also helps to decide abrasion resistance, water absorption and high pressure water penetration properties of the concrete due to inverse relationship between these properties and dielectric constant of concrete. In addition, the concrete with 0.6 w/c ratio has zero dielectric constant in the frequency range of 9 GHz - 14 GHz. Hence, one can expect an enhancement of intensity in radiation mechanisms caused by scattering of pseudo photons [9]. Therefore, the mentioned concrete can be used to design novel radomes which are used to prevent radars and antennas from environmental conditions. As a result, determination of w/c, abrasion resistance, water absorption and high pressure water penetration properties, compressive strength and splitting tensile strength can be carried out by microwave technique at a constant frequency as a nondestructive method due to direct or inverse proportionality between these properties and effective electrical properties of the concrete.

The dielectric constant of concrete with different w/c ratios in the 2nd month after casting is shown in Fig. 3 (b). It is seen that the dielectric constant is inversely proportional with w/c ratios. The higher values of dielectric constants compared to the values on the 28th day after casting are due to the reduction of the water content in concrete with the elapsed time. Hence, the concrete w/c ratios can be determined by microwave measurement techniques as nondestructive method. Beside this, the relationship between w/c and mechanical properties also permits us to determine the mechanical properties of concrete by microwave techniques. The gap between dielectric constants is widest at 8.5 GHz at which the dielectric constants are 2.8, 6 and 9 for 0.6, 0.5 and 0.4 w/c ratios, respectively. In addition, determination of the w/c ratios of concrete can also be carried out in entire frequency spectrum. Therefore, a simple microwave device that operates at a constant frequency can be used to specify the mentioned mechanical properties of the concrete depending on the electrical properties.

As a final step, the electrical properties of different cement types under various pressures are evaluated from the free space measurement coefficients of the reflection and transmission in the frequency spectrum of 3 GHz-18 GHz as shown in Fig. 4.

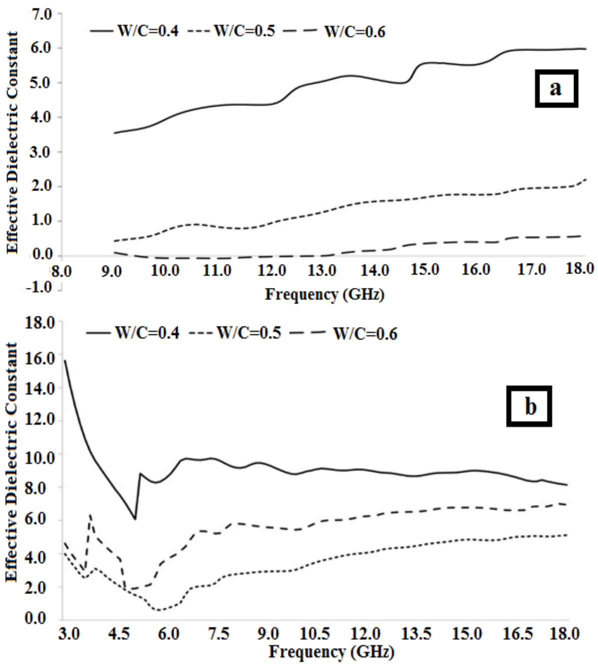

Fig. 3. Effective dielectric constants of cement with various w/c ratios for the: (a) 28th day and (b) 2nd month after casting.

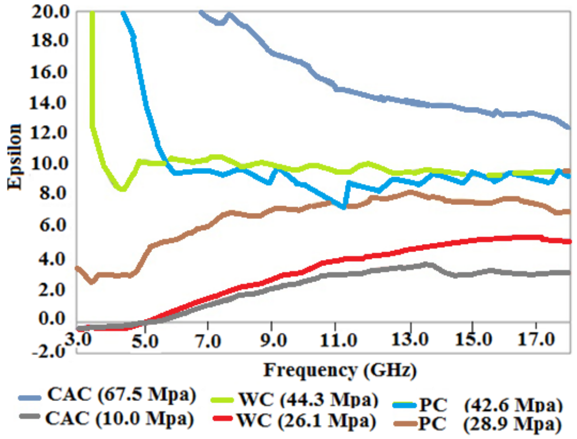

Fig. 4. Effective dielectric constants of different cement types under various pressures.

The measurements are carried out for calcium aluminat cement (CAC) under 67.5 MPa and 10 MPa pressure, white cement (WC) under the pressure of 44.3 MPa and 26.1 MPa and portland cement (PC) under the pressure of 42.6 MPa and 28.9 MPa. The higher values of pressure result in higher effective dielectric constants for each material under test for all types of cements. This is due to the increment of the density of the concrete. The reason is that the higher values of density results in higher values of dielectric constant. In addition, the effect of pressure on dielectric constant is much determinable with respect to the type of cement in concrete. Hence, it is possible to determine the applied pressure on concrete by microwave nondestructive method independent from the cement type. The effective dielectric constants at 17 GHz are around 14, 10, 9, 7.5, 4, 2 for calcium aluminat cement under 67.5 MPa pressure, white cement under 44.3 Mpa pressure, portland cement under 42.6 MPa pressure, portland cement under 28.9 MPa pressure, white cement under 26.1 MPa pressure and calcium aluminat cement under 10 MPa pressure, respectively. As a result, the cement type and pressure values can be determined by a microwave device operating at a constant frequency. Test results showed that there is a direct relation between epsilon values and compressive strengths. As seen in the figure, WQ increment in compressive strength causes increment in epsilon values (no matter which type of cement added into the concrete). Besides, as it can be seen in Fig. 4, the real part of dielectric constant is negative for two different types of calcium aluminat cement in the frequency range of 3 GHz-5 GHz. The negative value of dielectric constant is caused by the aluminat calcium aluminat cement with the metallic characteristics. With this novel measurement method, compressive strengths of the concretes are predictable and comparable without destructing concrete samples. In addition, having an idea about compressive strengths of the concrete samples allows predicting other mechanical and transport properties of the concretes as mentioned above.

IV. CONCLUSION

In this paper, Agilent brand 2-Port PNA-L Network Analyzer having the range from 10 MHz to 43.5 GHz is used for obtaining the scattering parameters and electromagnetic properties of the specially prepared concrete specimens. As it is well determined that the EM property of the concrete is one of the most important properties of the concrete that allows monitoring strength parameters and therefore, transport characteristics of the concrete because its EM characteristics is directly related to intensity of the sample which is concrete in this study. Although other traditional methods such as magnetic resonance imaging are also used to analyze properties of cement, the advantage of the proposed method is that the characteristic of the cement can be determined by a portable device which must be developed depending on the electromagnetic properties of the material under test.

According to test result, following conclusions can be drawn:

- A correlation between compressive strength and epsilon parameter is determined.
- Determining epsilon parameters would provide predicting strength of a concrete sample non-destructively. This nondestructive method provides faster determination of the strength of the concrete with respect to the destructive methods since this

procedure can be achieved in a few minutes.

- Correlation between compressive strength and epsilon parameters means also correlation between epsilon parameters and splitting tensile strength, abrasion resistance, water absorption, high pressure water penetration and other concrete properties.

Whereas concrete analysis and material content determination is realized by using microwave near field reflection property of the material under test in the study [4], the proposed method in this study get in contact with effective permittivity and mechanical properties of the material by using NRW method. Although the relationship between electrical and mechanical properties are also determined in another study by free space method up to 13 GHz [5], this study constitute this relationship by using another free space method (NRW method) in a wider frequency range up to 18 GHz. Nicolson Ross Weir method based microwave technique is used to characterize and retrieve electrical properties (dielectric constant) of concrete with various water/cement ratios and under different pressure levels in microwave frequency spectrum. The dielectric constant values for each material under test are evaluated from the measured values of reflection and transmission in the frequency range of 3 GHz-18 GHz. According to the results of the experimental investigations, the suggested nondestructive microwave method exhibits a reasonable difference and relationship between the mechanical and electrical properties of the concrete for the certain frequency points in the spectrum. Thus, the NRW technique is useful in the construction procedure of microwave devices/sensors operating at a constant frequency. In the case of water/cement ratio variation in concrete, the effective dielectric constant is inversely proportional within the entire frequency spectrum. Hence, the dielectric constant can be used to estimate w/c ratio in concrete. Besides, some of the mechanical properties related with w/c can also be determined. The effect of the ageing on the effective dielectric constant with respect to the water/cement ratio is also investigated for the 28 days and two months cured samples. The aging of the concrete sample results in an increment in the effective dielectric constants of the concrete with the same water/cement ratio due to settlement of density. The pressure effect on effective dielectric constant after the manufacturing process for different cement types in concrete is also carried out in the same frequency spectrum. It is also revealed that the increment of pressure also increases the effective dielectric constant due to higher density in unit cell. The pressure effect is more than the cement type. It is observed that a constant frequency of 17 GHz can be used to estimate the applied pressure by measuring the dielectric constant nondestructively. After all, microwave base techniques could be utilized more to be a good candidate for several nondestructive testing applications such as sensor, microwave devices, microwave tomography and so on.

REFERENCES

[1] P. C. Chang, A. Flatau, and S. C. Liu, "Review paper: Health monitoring of Civil infrastructure," *Structural Health Monitoring*, vol. 2, pp. 257-267, 2003.

[2] R. Zoughi, S. D. Gray, and P. S. Nowak, "Microwave nondestructive estimation of cement paste compressive strength," *ACI Materials Journal*, vol. 92, pp. 64-70, 1995.

[3] P. O. Moore, "American Society for Nondestructive Testing," Nondestructive Testing Handbook, 1999.

[4] M. Jamil, M. K. Hassan, H. M. A. Al-Mattarneh, and M. F. M. Zain, "Concrete dielectric properties investigation using microwave nondestructive techniques," *Materials and Structures*, vol. 46, pp. 77-87, 2013.

[5] K. J. Bois, A. D. Benally, and R. Zoughi, "Microwave near-field reflection property analysis of concrete for material content determination," *IEEE Transactions on Instrumentation and Measurement*, vol. 49, pp. 49-55, 2000.

[6] H. Boudjefdjouf, H. R. E. H. Bouchekara, F. de Paulis, M. K. Smail, A. Orlandi, and R. Mehasni, "Wire fault diagnosis based on time-domain reflectometry and backtracking search optimization algorithm," *ACES Journal*, vol. 31, pp. 340-347, 2016.

[7] B. Helifa, M. Feliachi, I. K. Lefkaier, F. Boubenider, A. Zaoui, and N. Lagraa, "Characterization of surface cracks using Eddy current NDT simulation by 3D-FEM and inversion by neural network, *ACES Journal*, vol. 31, pp. 187-194, 2016.

[8] A. M. Nicolson and G. Ross, "Measurement of intrinsic properties of materials by time domain techniques," *IEEE Transactions on Instrumentation and Measurement*, vol. 19, pp. 377-382, Nov. 1970.

[9] W. B. Weir, "Automatic measurement of complex dielectric constant and permeability at microwave frequencies," *Proceedings of the IEEE*, vol. 62, pp. 33-36, 1974.

[10] J. Němeček, V. Králík, V. Šmilauer, L. Polívka, and A. Jäger, "Tensile strength of hydrated cement paste phases assessed by micro-bending tests and nanoindentation,"*Cement and Concrete Composites*, vol. 73, pp. 164-173, 2016.

[11] V. H. Arakelian and Z. S. Gevorkian, "Radiation in systems with near zero dielectric constant," *Nuclear Instruments and Methods in Physics Research Section B: Beam Interactions with Materials and Atoms*, vol. 269, pp. 229-231, 2011.

[12] M. Esen, I. Ilhan, M. Karaaslan, E. Unal, F. Dincer, and C. Sabah, "Electromagnetic absorbance properties of a textile material coated using filtered arc-physical vapor deposition method," *Journal of Industrial Textiles*, vol. 45, no. 2, pp. 298-309, 2015.

[13] F. Dincer, M. Karaaslan, E. Unal, O. Akgol, and C. Sabah, "Multi-band metamaterial absorber: Design, experiment and physical interpretation," *ACES Journal*, vol. 29, no. 3, pp. 197-202, 2014.

[14] E. Dogan, E. Unal, D. Kapusuz, M. Karaaslan, and C. Sabah, "Microstrip patch antenna covered with left handed metamaterial," *ACES Journal*, vol. 28, no. 10, pp. 9999-1004, 2013.

Murat Öztürk received B.S. degree from Gaziantep University and M.S. degree from Iskenderun Technical University. He is currently with Iskenderun Technical University as Research Assistance. His research interests include electromagnetic behaviors of concrete.

Oguzhan Akgol received the B.Sc. degree from Inonu University, Turkey, the M.Sc. degree from Polytechnic University, Brooklyn, NY, USA, and the Ph.D. degree from University of Illinois at Chicago, (UIC), Chicago, IL, USA, all in Electrical and Electronics Engineering, in 2000, 2004, and 2011, respectively. He is currently working with Iskenderun Technical University, Hatay, Turkey. His research interests include EM scattering, antennas, and metamaterials.

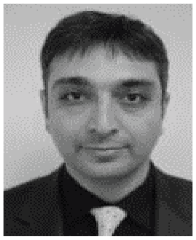

Muharrem Karaaslan received the Ph.D. degree in Physics Department from the University of Cukurova, Adana, Turkey, in 2009. He is the co-author of about 120 scientific contributions published in journals and conference proceedings. His research interest are applications of metamaterials, analysis and synthesis of antennas, and waveguides.

Emin Ünal received the Ph.D. degree in Electrical and Electronics Engineering from University of Gaziantep, Turkey, in 1994. He is the co-author of about 90 scientific contributions published in international books, journals and peer-reviewed conference proceedings. His research interest includes Frequency selective surfaces and metamaterials.

Umur Korkut Sevim received the Ph.D. degree in Civil Engineering Department from the University of Cukurova, Adana, Turkey, in 2003. He is currently working with Iskenderun Technical University, Hatay, Turkey. His research interest are concrete, construction materials and concrete admixture.

Performance of Beamwidth Constrained Linear Array Synthesis Techniques Using Novel Evolutionary Computing Tools

Chowdary S.R. Paladuga [1], **Chakravarthy V.S.S.S. Vedula** [1], **Jaume Anguera** [2,3],
Rabindra K. Mishra [4], **and Aurora Andújar** [2,3]

[1] Department of Electronics & Communication Engineering
Raghu Institute of Technology, Visakhapatnam, India
satishchowdary@ieee.org, sameervedula@ieee.org

[2] Department of Electronics and Telecommunications
University Ramon Llull, Barcelona, Spain

[3] Fractus Antennas, Barcelona, Spain
jaume.anguera@fractusantennas.com, aurora.andujar@fractusantennas.com

[4] Department of Electronics, Berhampur University
Berhampur, Odisha, India
r.k.mishra.ieee@gmail.com

Abstract ─ Antenna array synthesis for desired radiation characteristics is a challenging field of research in electromagnetics. When an array synthesis problem is visualized as an optimization problem several design parameters involved in synthesis process are considered as degrees of freedom. Every combination of design parameters forms a synthesis technique. In this paper, certain emphasis is given to analyse the techniques of linear array (LA) design using evolutionary computing tools. Novel computing tools like Flower Pollination Algorithm is used for LA synthesis using different degrees of freedom and compared with a conventional Tchebycheff method. Accelerated Particle Swarm Optimization (APSO) is also employed to study the consistency of the technique with the employed computing tool. Radiation patterns are generated with optimized SLL and Tchebycheff beamwidth constraint.

Index Terms ─ Antenna optimization, array synthesis, flower pollination algorithm, particle swarm optimization.

I. INTRODUCTION

Radiating elements for modern wireless communications needs to possess certain features like high directivity, good control on sidelobe level (SLL), control on beam width (BW) and beam steering (BS) capabilities [1]. Single element antenna fail to achieve the above, as they exhibit poor directivity and no control on SLL and BW. Impetus to highly directive communication systems is made possible with the advent of the antenna arrays are capable of controlling radiation pattern for desired main BW, half power BW and SLL with proper modifications of geometrical and electrical properties of the array [2]. Among different array geometries, linear array is the simplest form of the array in which all the elements are arranged on a straight line. Many conventional numerical techniques which are derivative based are proposed for such array synthesis. These conventional techniques are time consuming with complex numerical steps and always tend to stick in the local minima. Also, they fail to handle multimodal or multi objective problems. In the recent past, several meta-heuristic algorithms are proposed to overcome the computational complexity and its drawback. These algorithm are versatile and also robust. They are capable of handling multimodal problems with ease. Many algorithm like genetic algorithm (GA) [3], particle swarm optimization (PSO) [4], simulated annealing (SA) [5], fire fly (FF) [6], and Teaching Learning Based Optimization [7] and have already been successfully applied for antenna design. An antenna array synthesis problem involves in determining weights for the geometrical properties like spacing (d) between elements or electrical properties like current excitation and phase excitation that produces desired radiation pattern. The evolutionary computing tools are efficient and robust to synthesize antenna array of any geometry like linear, circular and conformal [8]. Also, capable of producing wide variety of radiation patterns for several applications like beamforming, mono-pulse radar etc. [9].

An array synthesis problem can be addressed as an optimization problem which involves in determining the

Submitted On: February 19, 2017
Accepted On: January 4, 2018

optimal weights for one or more array parameters in order to produce the desired radiation pattern. Amplitude only technique is one of the simple strategy to obtain the design criteria which involves in obtaining the amplitudes of coefficients of current excitation at each element in the array [10]. However, including spacing as additional parameter for synthesis of array is another intelligent way to achieve the convergence quickly. In this paper, such an attempt is made to investigate the advantage in adding additional parameter to the synthesis process and compare the results with the process involving only one parameter. In this regard, amplitude and spacing between the elements are considered in a two-parameter method while amplitude only is used in a one-parameter method. It is concluded from the literature that incorporating newly proposed heuristic approaches which are widely accepted in other disciplines for antenna array synthesis is a predominant part of research in electromagnetics. This consistently helped antenna engineers to take on the challenges of pattern synthesis for wireless applications. Accordingly, in this paper, two new algorithms namely APSO and Flower Pollination Algorithm (FPA) have been chosen. Further a comparative study is performed to analyze the performance of these algorithms over existing popular numerical technique called Tchebycheff technique. Several objectives are considered for synthesis of linear arrays in this work. Obtaining a very low SLL of -50dB with narrowest possible BW that is equal to the TBW for the same SLL is one of the major objective of investigation. The other objectives is to study the synthesis process using both amplitude only and amplitude-space techniques. Symmetrical linear arrays is considered in all the cases mentioned in this work.

II. DESIGN FORMULATION

Array design formulation and the corresponding fitness formulation for the desired objectives are presented in this Section as follows.

A. Array factor formulation

Linear array design problem involves in generating optimal set of design parameters like amplitudes or inter-element spacing or both that yields radiation pattern with optimum SLL with predefined BW. The geometry of the array is as shown in Fig. 1.

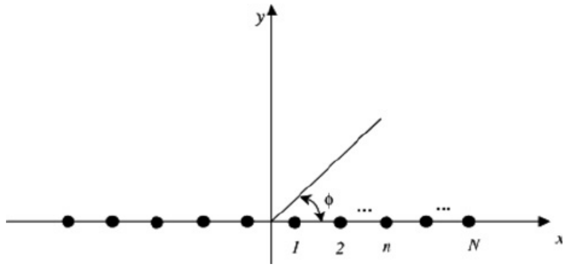

Fig. 1. Geometry of linear array antenna.

The LA geometry specified in the Fig. 1 has the centre of the array length as the reference and the elements are symmetrical arranged around the reference point. The array factor of such a linear symmetric array is given as (1) [11]:

$$AF(\theta)=2\sum_{n=1}^{N} A_n \cos[\mathrm{kd}_n \cos\theta+\beta_n], \tag{1}$$

where

n refers to nth element and n=1,2…..N,

N is the total number of elements in the array,

k is wave number given as 2Π/λ,

θ is observation angle,

A$_n$ refers to the amplitude of excitation of nth element,

d$_n$ refers to the spacing between the nth element and the reference point.

B. Fitness formulation

The formulation of fitness function incorporates the objective of SLL reduction and BW control. The radiation pattern is the distribution computed array factor (AF) values for every interval of azimuthal angle (θ) over a range of -90^0 to 90^0. Hence, the fitness is formulated as a function of AF values in order to obtain the desired patterns:

$$SLL_{diff} = SLL_{des} - \max[\,|\,\mathrm{AF}(\theta)\,|_{-90}^{\theta_0-\frac{BW_{obt}}{2}}\,], \tag{2}$$

$$\mathrm{BW}_{diff} = |\,\mathrm{BW}_{Cheb} - \mathrm{BW}_{obt}\,|, \tag{3}$$

$$\begin{aligned} \mathrm{f}_1 &= SLL_{diff} && if\ SLL_{diff} > 0 \\ &= 0 && otherwise \end{aligned}, \tag{4}$$

$$\begin{aligned} \mathrm{f}_2 &= SLL_{diff} && if\ SLL_{diff} > 0 \\ &= 0 && otherwise \end{aligned}, \tag{5}$$

$$f = c_1\,\mathrm{f}_1 + c_2\,\mathrm{f}_2, \tag{6}$$

where, SLL$_{diff}$ is the difference between the desired SLL (SLL$_{des}$) and the obtained SLL (SLL$_{obt}$). BW$_{diff}$ is the difference between the desired TBW (BW_{Cheb}) and the obtained beamwidth (BW_{obt}). In this case f$_1$ is responsible for SLL reduction and f$_2$ controls the BW of the array. The final fitness f value calculated as summation of f$_1$ and f$_2$, where c$_1$ and c$_2$ are two constant biasing weighting factors such that:

$$c_1 + c_2 = 1. \tag{7}$$

However, in the current work no biasing is applied and the objectives are provided with equal weight, such that c$_1$=c$_2$.

III. ARRAY DESIGN USING FLOWER POLLINATION ALGORITHM

The FPA mimics the flower pollination phenomenon [12] through biotic and abiotic processes which is essential for reproduction in floral plants. Pollination is the process by which pollens migrate and meet the pollen of another flower of same plant or other plant of same species resulting in successful fertilization. Pollination can be local or global. Self pollination can be treated as local pollination in which the pollen of a flower is shared by same flower or another flower of the same plant. Biotic cross pollination, which takes place over long distances is known as global pollination. Reproduction and evolution of the plant species is greatly affected by several aspects like fertilization, floral constancy and mutualism. Mutualism limits the memory and energy consumption of the pollinators and often leads to successful fertilization. Each individual member of the population refers to an array. After initialization radiation pattern is computed for each individual using the array factor formulation for linear arrays. Using the fitness function, the cost is evaluated for each individual. Best individual with minimum cost is chosen and its characteristics for convergence is obtained to validate the optimum solution. If the convergence is achieved then the process is terminated and the best individual's weights are considered for the objective. If the convergence is not achieved the weights of each individual are modified according to the FPA structure as given in next section. Demonstration of the FPA implementation for LA synthesis is as shown in Fig. 2. Like every population based algorithm the starting point of FPA is population initialization. *M* individuals are used as population. Each individual has its own solution in the *N*-dimensional solution space. *N* also refers to number of design variables. Hence, each solution is a set of *N*-dimensional vector which is given as:

Initial population:

$$pop=[x_1(k),x_2(k)....], \tag{8}$$

where *k* is the iteration number,

$$\begin{bmatrix} x_1 \\ x_2 \\ . \\ x_M \end{bmatrix} = \begin{bmatrix} I_1^1, I_1^2, ..., I_1^N \\ I_2^1, I_2^2, ..., I_2^N \\ .... \\ I_M^1, I_M^2, ..., I_M^N \end{bmatrix}. \tag{9}$$

Equation (9) is used to represent the initial population for amplitude only technique in which *I* is current excitation coefficient and d is inter-element spacing.

When both current excitation and inter element spacing are used the (9) is modified to (10) in such a way that *x* is vector of dimension 2N. The first N values are used as current excitations and the remaining N are used as inter element spacing for the corresponding element. Implementation of the algorithm for array synthesis involves in considering each individual that corresponds to an array of *N* elements.

The algorithm was implemented using MATLAB® software. Numerical value representing the element is the current excitation coefficient of that element:

$$\begin{bmatrix} x_1 \\ x_2 \\ . \\ x_M \end{bmatrix} = \begin{bmatrix} I_1^1, I_1^2, ..., I_1^N, d_1^1, d_1^2, ...d_1^N \\ I_2^1, I_2^2, ..., I_2^N, d_2^1, d_2^2, ...d_2^N \\ .... \\ I_M^1, I_M^2, ..., I_M^N, d_M^1, d_M^2, ...d_M^N \end{bmatrix}. \tag{10}$$

Finally the fitness is evaluated for each individual and the best among them is supposed to be the individual with minimum fitness. This is given as [11,12]:

$$x^*(\mathrm{k}) = \arg \min_{m=1,....M} f(\mathrm{x}_m(\mathrm{k})). \tag{11}$$

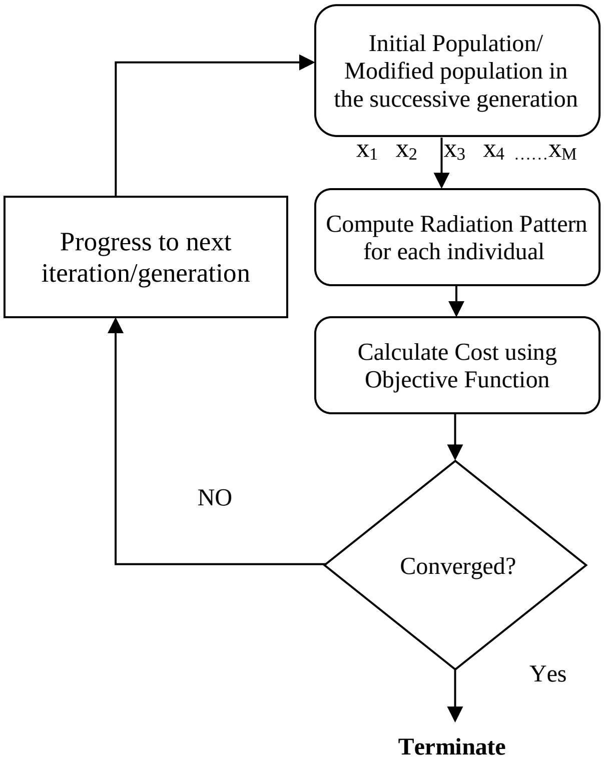

Fig. 2. Flowchart demonstrating the implementation of FPA for linear array synthesis.

IV. RESULTS AND DISCUSSIONS

Results pertaining to the TBW constrained SLL reduction using FPA and APSO are presented in this section using both amplitude only (Amp-only) and amplitude-spacing (Amp-Sp) techniques. Case 1 presents the radiation patterns obtained using the three synthesis methods using amplitude only, while Case 2 refers to similar but using Amp-Sp technique. In both the cases the number of elements in the LA are considered to be 8 and 32. The proposed simulation based experimental frame work is useful in evaluating the performance of the technique using both the algorithms. However, the performance of both the algorithms assumed to be at par with each other, while the inference is the adaptability of the evolutionary tools in incorporating any technique of synthesis. For the simulation study, both the algorithms are tuned for array synthesis problem. Parameters like initial population, termination criterion and other algorithm specific parameters play a vital role in finding solution to the problem. These parameters and their values are listed in Table 1 and Table 2.

Table 1: Algorithm specific parameters used in APSO for the simulation study

Parameter	Value
Initial Population (number of birds)	60
Convergence speed determinants α, β, and γ	0.2, 0.5, 0.95
Termination Criterion	Min cost (0) or max number of generations (1000)

Table 2: Algorithm specific parameters used in FPA for the simulation study

Parameter	Value
Initial Population	25
Probability of switching	0.8
Termination Criterion	Minimum cost (0) or maximum number of generations (1000)

The initial population in APSO is larger than the FPA because of the fact that, the APSO uses only the global search while FPA employs both global and local search techniques using switching parameter. Hence, for better convergence choice of large population is always useful.

A. Case-1

The radiation pattern plots for the linear array with N=8 and 32 and their corresponding convergence plots are presented in Fig. 3, Fig. 4, Fig. 5 and Fig. 6. The SLL obtained using APSO and FPA are well maintained at the same level as that of Tchebycheff with the constraint of the Tchebycheff beam width (BW). It can be inferred from both the converegence plots that APSO and FPA have similar converegence characteristics. However, the FPA consumed relevantly less number of iterations with respect to APSO because of the search capability. Inspite of this, the convergence time of APSO is better than FPA as the APSO employs only the global search technique.

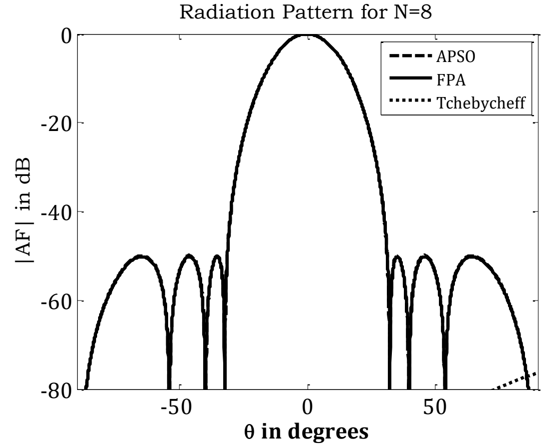

Fig. 3. Comparison of radiation pattern of 8 element LA with non-uniform amplitude distribution.

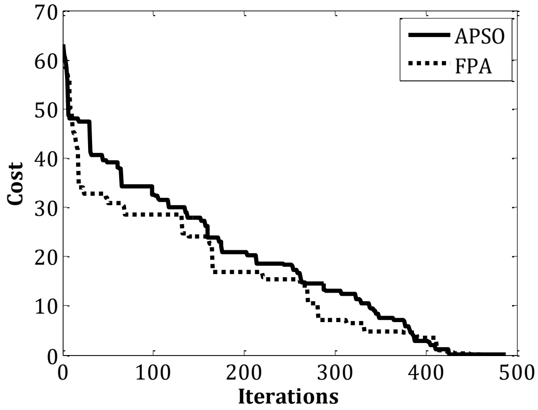

Fig. 4. Comparison of convergence characteristics for 8 element LA.

B. Case-2

In this case, the amplitude-spacing technique is employed to synthesize linear array of 8 and 32 element size. The simulated radiation pattern plots using APSO, FPA and Tchebycheff methods along with the convergence plots are presented in Fig. 7, Fig. 8, Fig. 9 and Fig. 10. The convergence trend is similar to the previous case. The FPA is consumed less number of iterations than APSO while the computation time is better in the case of APSO. The non-uniform amplitude distribution for Amp-Only technique and the corresponding non-uniform amplitude and non-uniform spacing in Amp-Sp technique are presented in Table 3 and Table 4.

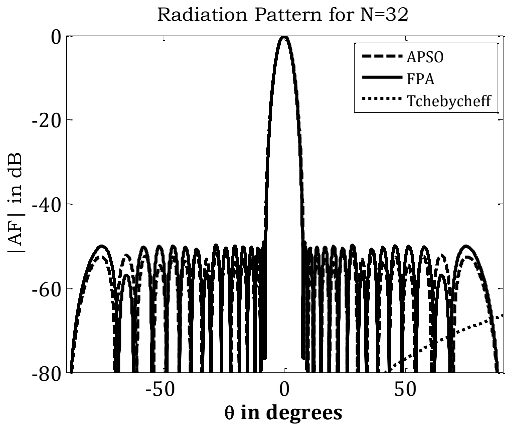

Fig. 5. Comparison of radiation pattern of 32 element LA with non-uniform amplitude distribution.

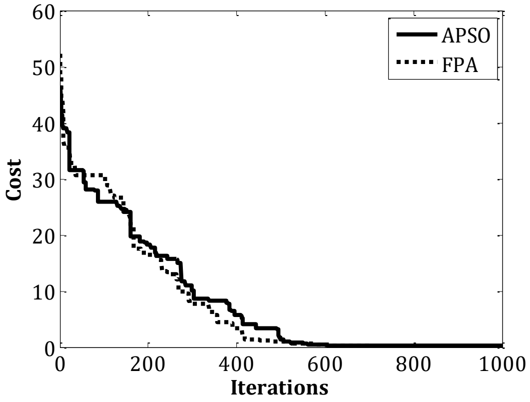

Fig. 6. Comparison of convergence characteristics for 32 element LA.

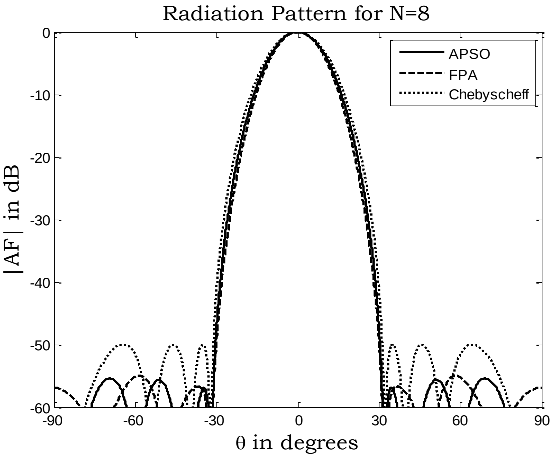

Fig. 7. Comparison of radiation pattern of 8 element LA with non-uniform amplitude and space distribution.

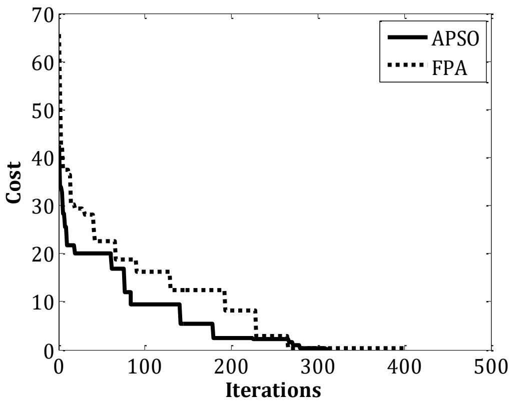

Fig. 8. Convergence plot for 8 element linear array synthesized using amplitude-spacing technique.

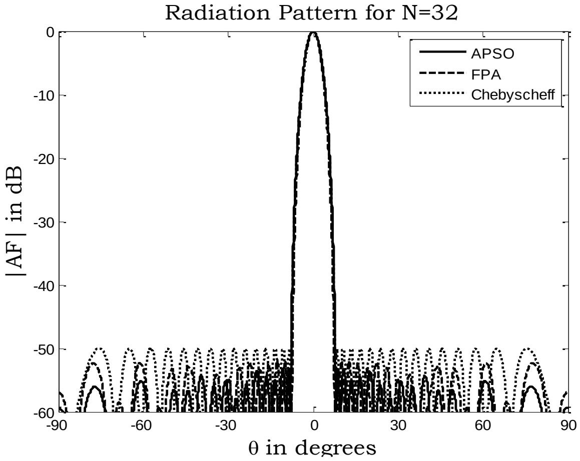

Fig. 9. Comparison of radiation rattern of 32 element LA with non-uniform amplitude and space distribution.

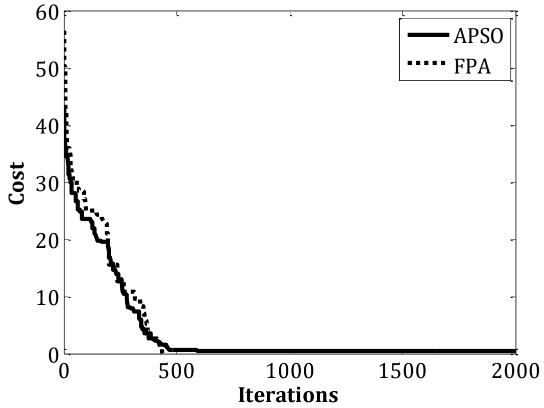

Fig. 10. Convergence plot for 32 element linear array synthesized using amplitude-spacing technique.

Table 3: Non-uniform amplitude distribution and amplitude-spacing distribution for Fig. 3 and Fig. 5 radiation patterns

Element Number	Fig. 3			Fig. 5	
	Amp			Amp (Sp in λ)	
	APSO	FPA	Tcheb	APSO	FPA
1 & 1’	0.932	0.954	1.00	0.92 (0.48)	0.83 (0.61)
2 & 2’	0.670	0.684	0.71	0.72 (0.50)	0.55 (0.61)
3 & 3’	0.326	0.332	0.34	0.37 (0.53)	0.22 (0.62)
4 & 4’	0.088	0.089	0.09	0.09 (0.56)	0.04 (0.63)

Table 4: Non-uniform amplitude distribution and amplitude-spacing distribution for Fig. 4 and Fig. 6 radiation patterns

Element Number	Fig. 4			Fig. 6	
	Amp			Amp (Sp in λ)	
	APSO	FPA	Tcheb	APSO	FPA
1 & 1’	0.944	0.926	1.000	0.98 (0.45)	0.69 (0.55)
2 & 2’	0.925	0.910	0.979	0.95 (0.46)	0.74 (0.59)
3 & 3’	0.884	0.871	0.939	0.82 (0.41)	0.71 (0.63)
4 & 4’	0.827	0.818	0.882	0.99 (0.46)	0.62 (0.62)
5 & 5’	0.757	0.749	0.811	0.54 (0.41)	0.44 (0.56)
6 & 6’	0.676	0.677	0.728	0.98 (0.41)	0.35 (0.41)
7 & 7’	0.588	0.590	0.639	0.94 (0.64)	0.42 (0.51)
8 & 8’	0.496	0.505	0.546	0.63 (0.61)	0.35 (0.59)
9 & 9’	0.409	0.418	0.455	0.46 (0.48)	0.22 (0.52)
10 & 10’	0.325	0.340	0.367	0.36 (0.47)	0.20 (0.45)
11 & 11’	0.250	0.263	0.287	0.33 (0.46)	0.18 (0.58)
12 & 12’	0.184	0.195	0.215	0.29 (0.59)	0.10 (0.55)
13 & 13’	0.127	0.142	0.154	0.16 (0.61)	0.08 (0.44)
14 & 14’	0.084	0.095	0.105	0.08 (0.44)	0.07 (0.64)
15 & 15’	0.051	0.060	0.066	0.08 (0.52)	0.03 (0.60)
16 & 16’	0.036	0.043	0.050	0.04 (0.66)	0.01 (0.45)

The corresponding SLL obtained with the BW constraint using amplitude only technique and the amplitude spacing technique were presented in Table 5.

Table 5: SLL using amplitude only and Amp-Sp techniques

S.No	No. of Elements	SLL (dB) Using FPA		SLL (dB) Using APSO	
		Amp Only	Amp-Sp	Amp Only	Amp-Sp
1	8	-50.0	-56.7	-51.4	-57
2	32	-50.0	-52.3	-51.4	-53.2

From the radiation pattern plots and the corresponding SLL using both the techniques it is clear that there’s respectable amount of SLL suppression in Amp-Sp which is better than Amp-Only technique. The response is consistent even when the adopted algorithm is changed from FPA to APSO.

V. CONCLUSION

The study involved in using two improved evolutionary computing tools for effective design of linear arrays which has not been attempted earlier. In the investigation, both conventional and evolutionary computing techniques have been presented for distinct cases. It may be mentioned that inclusion of additional parameter of antenna in conventional design makes the task more complicated. However, it is determined that the use of new evolutionary computing tools made it possible to include inter element spacing in the design which has yield improved performance.

REFERENCES

[1] Randy L. Haupt, *Antenna Arrays: A Computational Approach*. Wiley New York, 2010.

[2] Rabindra K. Mishra, *Optimization Techniques for Planar Antennas*. 3rd ed., vol. 2, John Wiley & Sons Ltd, pp. 79-86, 2011.

[3] D. Goldberg, *Genetic Algorithms in Search, Optimiz-ation, and Machine Learning*. Pearson Education, 1989.

[4] J. Kennedy and R. Eberhart, “Particle swarm optimization,” *Neural Networks, 1995, Proceedings, IEEE International Conference on*, vol. 4, pp. 1942, 1948, vol. 4, Nov./Dec. 1995, doi: 10.1109/ICNN.1995.488968

[5] S. Kirkpatrick, C. D. Gelatt, and M. P. Vecchi, “Optimization by Simulated Annealing,” *Science 220* (4598), 671-680, 1989.

[6] X.-S. Yang, “Firefly algorithm, stochastic test functions and design optimisation,” *International Journal of Bio-Inspired Computation*, pp. 78-84, 2010.

[7] V. V. S. S. S. Chakravarthy, K. Naveen Babu, S. Suresh, P. Chaya Devi, and P. Mallikarjuna Rao, “Linear array optimization using teaching learning based optimization,” *Advances in Intelligent Systems and Computing, AISC 338*, pp. 183-187, 2015.

[8] S. K. Irfanullah and B. D. Braaten, “Improvement of the broadside radiation pattern of a conformal antenna array using amplitude tapering,” *ACES Journal*, vol. 32, no. 6, June 2017.

[9] S. Mubeen, A. M. Prasad, and A. Jhansi Rani, “On the beam forming characteristics of linear array using nature inspired computing techniques,” *ACES Expresss Journal*, vol. 1, no. 6, June 2016.

[10] V. S. S. S. Chakravarthy Vedula, S. R. Chowdary Paladuga, and M. Rao Prithvi, “Synthesis of circular array antenna for sidelobe level and aperture size control using flower pollination algorithm,” *International Journal of Antennas and Propagation*, vol. 2015, Article ID 819712, 9 pages, 2015.

[11] V. V. S. S. S. Chakravarthy, P. S. R. Chowdary, G. Panda, J. Anguera, A. Andújar, and B. Majhi, “On the linear antenna array synthesis techniques for sum and difference patterns using flower pollination algorithm,” Arab J. Sci. Eng., 1-13, 2017. doi: 10.1007/s13369-017-2750-5

[12] X.-S. Yang, M. Karamanoglu, and X. Hi, “Flower pollination algorithm: A novel approach for multi-objective optimization,” *Engineering Optimization*, vol. 46, no. 9, Sep. 2011.

Extreme Learning Machine with a Modified Flower Pollination Algorithm for Filter Design

Li-Ye Xiao, Wei Shao, Sheng-Bing Shi, and Zhong-Bing Wang

School of Physics
University of Electronic Science and Technology of China, Chengdu, 610054, China
liyexiao@std.uestc.edu.cn, weishao@uestc.edu.cn, shengbing77@163.com, bzwang@uestc.edu.cn

Abstract **─** In this paper, a modified flower pollination algorithm (FPA) based on the steepest descent method (SDM) is proposed to set the optimal initial weights and thresholds of the extreme learning machine (ELM) for microwave filter design. With the proposed SDM-FPA, the model trained by the ELM can achieve higher accuracy with smaller training datasets for electromagnetic modeling, comparing to that achieved by traditional artificial neural network. The validity and efficiency of this proposed method is confirmed by a parametric modeling example of filter design.

Index Terms **─** Extreme learning machine (ELM), filter design, flower pollination algorithm (FPA), steepest descent method (SDM).

I. INTRODUCTION

In the design of microwave components or circuits, an optimization algorithm is often employed and it usually invokes the electromagnetic simulations repeatedly. The time-consuming full-wave simulations result in a heavy computational burden to complete the design. Fortunately, the artificial neural network (ANN) has been introduced to learn the relationship between geometrical variations and electromagnetic (EM) responses by a training process [1-3]. Once the geometrical parameters are imported into a trained ANN, it can fast obtain the accurate EM responses. An advanced study, which combines the neural network and transfer function (TF), was developed to model the EM behavior of embedded passive components [4]. In [4], the neural network is used for mapping the geometrical variations of the components onto the TF coefficients without having to rely on prior knowledge.

The most time-consuming part of ANN model construction is the collection of training and testing samples for model training and testing. How to reduce computation time and save more costs of model construction is a problem worth studying.

In the training process, the value of initial weights and thresholds is an important factor to determine the convergence of ANN. With the optimal initial weights and thresholds determined, the initial error is substantially smaller and therefore number of training samples that come from the time-consuming EM simulations to achieve the error criterion is reduced [5]. In general, the optimal initial weights and thresholds of ANN can be obtained through an optimization process.

In this paper, an effective ANN model, the extreme learning machine (ELM), is presented for filter design. By fixing input weights and hidden layer bias of a single-hidden layer feed-forward neural network (SLFN), ELM transforms the learning of SLFN into a matrix calculation, which largely improves the learning speed over the traditional feed forward network learning algorithms [6]. To further reduce computation time and save more training costs, a modified flower pollination algorithm (FPA) based on the steepest descent method (SDM) is developed to determine the optimal initial weights and thresholds of ELM. The SDM-FPA-ELM is used to learn the relationship between the geometrical variations of filters and the TF coefficients through the training process. Compared with the ANN model in [7], the proposed ELM can achieve the trained model with small training dataset and accurate results due to its good iterative learning ability. The validity of this proposed model is confirmed with the design of a quadruple-mode filter.

II. PROPOSED MODEL

A. Modified FPA: SDM-FPA

FPA has powerful global exploration and exploitation abilities, and its convergence speed in early period of optimization is fast [8]. However, during the late period of optimization, its convergence speed becomes slow and its accuracy is imprecise. To overcome the weakness and improve the optimized performance of FPA, a new modified FPA based on the steepest descent method (SDM) is developed in this work.

Let $\boldsymbol{x}^{iter}$ be the positions of flowers in FPA, where *iter* represents the current iteration number. Generally, $\boldsymbol{x}^{iter}$ is input into the fitness function directly to evaluate the current best value. To improve the local search ability of FPA, an SDM circulation is added in FPA. In

Submitted On: May 2, 2017
Accepted On: January 22, 2018

this circulation, $\boldsymbol{x}^{iter}$ will be the initial value to continue searching with the steepest descent direction $-\nabla f\left(\boldsymbol{x}_j^{iter}\right)$ and steplength λ_j^{iter}. This iterative loop could be presented as:

$$\boldsymbol{x}_{j+1}^{iter} = \boldsymbol{x}_j^{iter} + \lambda_j^{iter}\boldsymbol{d}_j^{iter}, \left(j = 0, 1, \cdots, M-1\right), \qquad (1)$$

where $\boldsymbol{d}_j^{iter} = -\nabla f\left(\boldsymbol{x}_j^{iter}\right)$, and M is the total number of SDM iterations.

After processing the SDM circulation, a new position of $\boldsymbol{x}_M^{iter}$ is obtained. $\boldsymbol{x}_M^{iter}$ is input into the fitness function to evaluate a value as the current best result. Then $\boldsymbol{x}_M^{iter}$ is updated to $\boldsymbol{x}_0^{iter+1}$ according to the FPA rules [8]. Meanwhile, to keep the results from trapping in local optimums, a lot of experiments have been done to select the total iteration number *M*. Finally we find that when *M* is set in the region from 4 to 6, the optimization performance is good. If *M* is less than 4, the rate of convergence may not be enhanced. And if *M* is greater than 6, the results are easily trapped in local optimums.

The statistics of optimal objectives for ten test functions [9] are tabulated in Table 1, and the best results are formatted in bold. It is clear in Table 1 that SDM-FPA works well and it is superior to the traditional FPA.

Table 1: Statistic of optimal objective values for the test functions

Test Function	Method	Min	Mean
Sphere function	FPA	7.0241×10^{-33}	8.2901×10^{-27}
	SDM-FPA	4.4521×10^{-63}	4.6425×10^{-61}
Beale function	FPA	6.4625×10^{-27}	9.6821×10^{-24}
	SDM-FPA	0	0
Griewank's function	FPA	6.3672×10^{-8}	6.5645×10^{-6}
	SDM-FPA	7.5485×10^{-67}	6.4654×10^{-64}
Matyas function	FPA	5.0086×10^{-42}	5.8247×10^{-28}
	SDM-FPA	2.5498×10^{-68}	5.0834×10^{-53}
Schaffer function	FPA	0	0
	SDM-FPA	0	0
Rastrigin's function	FPA	6.5643×10^{-16}	8.7436×10^{-10}
	SDM-FPA	0	2.8594×10^{-72}
Schwefel function	FPA	1.5549×10^{-6}	1.1032×10^{-5}
	SDM-FPA	1.5516×10^{-14}	1.5543×10^{-12}

B. Proposed ELM: SDM-FPA-ELM

ELM is a powerful and fast learning algorithm based on the modification of the traditional SLFNN [10]. It has been proved that the ELM network has better accuracy performance than the ANNs and the support vector machine [11].

Here, the network weights $\boldsymbol{\omega}$ between the input layer and the hidden layer are defined as:

$$\boldsymbol{\omega} = \begin{bmatrix} \omega_{11} & \omega_{12} & \omega_{13} & \cdots & \omega_{1n} \\ \omega_{21} & \omega_{22} & \omega_{23} & \cdots & \omega_{2n} \\ \vdots & \vdots & \vdots & & \vdots \\ \omega_{l1} & \omega_{l2} & \omega_{l3} & \cdots & \omega_{ln} \end{bmatrix}_{l\times n}, \qquad (2)$$

where *l* is the number of the hidden neurons and *n* is the number of the input neurons. The network weights $\boldsymbol{\beta}$ between the hidden layer and the output layer are defined as:

$$\boldsymbol{\beta} = \begin{bmatrix} \beta_{11} & \beta_{12} & \beta_{13} & \cdots & \beta_{1m} \\ \beta_{21} & \beta_{22} & \beta_{23} & \cdots & \beta_{2m} \\ \vdots & \vdots & \vdots & & \vdots \\ \beta_{l1} & \beta_{l2} & \beta_{l3} & \cdots & \beta_{lm} \end{bmatrix}_{l\times m}, \qquad (3)$$

where *m* is the number of the output neurons. And the thresholds $\boldsymbol{b}$ of the hidden layer are defined as:

$$\boldsymbol{b} = \left[b_1, b_2, \cdots, b_l\right]_{l\times 1}^T. \qquad (4)$$

At the beginning of the training process, the initial values of $\boldsymbol{\omega}$, $\boldsymbol{\beta}$ and $\boldsymbol{b}$ are set randomly. However, the final results of ELM are strongly dependent on the initial weights and thresholds, and the bad initial weights and thresholds may lead to a slow convergence of the optimal value in ELM. To avoid wasting more training costs, in this paper, an optimization method is proposed to determine the initial weights and thresholds based on SDM-FPA.

There are two processes in SDM-FPA-ELM: the optimization of the values of $\boldsymbol{\omega}$, $\boldsymbol{\beta}$ and $\boldsymbol{b}$ and ELM training. The structure of SDM-FPA-ELM is shown in Fig. 1.

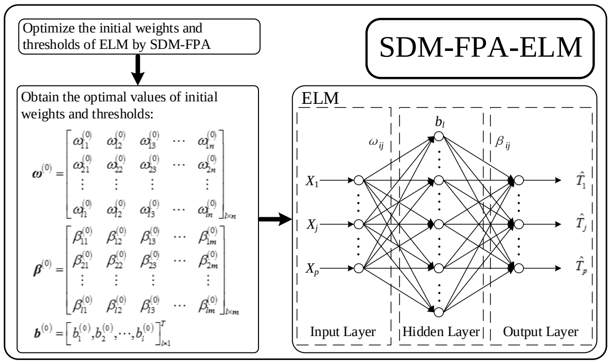

Fig. 1. Structure of SDM-FPA-ELM.

The fitness function in SDM-FPA is expressed as follows:

$$f\left(\boldsymbol{\omega}, \boldsymbol{\beta}, \boldsymbol{b}\right) = \min\left|\boldsymbol{T} - \hat{\boldsymbol{T}}\left(\boldsymbol{\omega}, \boldsymbol{\beta}, \boldsymbol{b}\right)\right|. \qquad (5)$$

Here, the elements in $\boldsymbol{T}$ are the actual values of the real and imaginary parts of *S*-parameters:

$$\boldsymbol{T}=\begin{bmatrix} t_{11} & t_{12} & t_{13} & \cdots & t_{1P} \\ t_{21} & t_{22} & t_{23} & \cdots & t_{2P} \\ \vdots & \vdots & \vdots & & \vdots \\ t_{m1} & t_{m2} & t_{m3} & \cdots & t_{mP} \end{bmatrix}_{m\times P}, \tag{6}$$

and $\hat{\boldsymbol{T}}(\boldsymbol{\omega},\boldsymbol{\beta},\boldsymbol{b})$, which represents the outputs of the ELM network, is defined as:

$$\begin{aligned}&\hat{\boldsymbol{T}}(\boldsymbol{\omega},\boldsymbol{\beta},\boldsymbol{b})= \\ &\left[\hat{\boldsymbol{t}}_1(\boldsymbol{\omega},\boldsymbol{\beta},\boldsymbol{b}),\hat{\boldsymbol{t}}_2(\boldsymbol{\omega},\boldsymbol{\beta},\boldsymbol{b}),\cdots,\hat{\boldsymbol{t}}_P(\boldsymbol{\omega},\boldsymbol{\beta},\boldsymbol{b})\right]\end{aligned}, \tag{7}$$

where

$$\hat{\boldsymbol{t}}_j(\boldsymbol{\omega},\boldsymbol{\beta},\boldsymbol{b})=\begin{bmatrix}\hat{t}_{1j}\\ \hat{t}_{2j}\\ \vdots\\ \hat{t}_{mj}\end{bmatrix}_{m\times1}=\begin{bmatrix}\sum_{i=1}^{l}\beta_{i1}g\left(\boldsymbol{\omega}_i\boldsymbol{X}_j+b_i\right)\\ \sum_{i=1}^{l}\beta_{i2}g\left(\boldsymbol{\omega}_i\boldsymbol{X}_j+b_i\right)\\ \vdots\\ \sum_{i=1}^{l}\beta_{im}g\left(\boldsymbol{\omega}_i\boldsymbol{X}_j+b_i\right)\end{bmatrix}_{m\times1}, \tag{8}$$

where

$$\boldsymbol{X}_j=\left[X_{1j},X_{2j},X_{3j},\cdots,X_{n-1j},X_{nj}\right]^T,\left(j=1,2,3,\cdots,P\right).$$

The elements in $\boldsymbol{X}$ are the inputs of ELM, such as the operation frequency, geometrical sizes and material parameters of microwave passive components.

When an iteration of SDM-FPA finishes, the current best values of $\boldsymbol{\omega}$, $\boldsymbol{\beta}$ and $\boldsymbol{b}$ are updated and substituted into ELM. After the input of $\boldsymbol{X}$ and output of $\boldsymbol{T}$ are applied to this ELM, the fitness function could be employed to evaluate this series of weights and thresholds.

This process will proceed till the objective tolerance of SDM-FPA is satisfied. And the obtained optimal values of weights and thresholds will be set as the initial ones of ELM, named as $\boldsymbol{\omega}^{(0)}$, $\boldsymbol{\beta}^{(0)}$ and $\boldsymbol{b}^{(0)}$.

The details of the next training process of ELM algorithm are shown in [10].

C. SDM-FPA-ELM-TF model

In this paper, the pole-residue-based transfer function, an effective TF form used in EM simulations, is chosen for our proposed model. The transfer function is presented as follows

$$H(s)=\sum_{i=1}^{N}\frac{r_i}{s-p_i}, \tag{9}$$

where p_i and r_i represent the poles and residues of the transfer function, respectively, and N is the function order [7].

The whole process of the SDM-FPA-ELM-TF model in Fig. 2 is as follows:

1) Collect the training and testing data with full-wave EM simulations.
2) Use SDM-FPA to optimize $\boldsymbol{\omega}$, $\boldsymbol{\beta}$ and $\boldsymbol{b}$, and set the initial values of weights and thresholds of ELM, named as $\boldsymbol{\omega}^{(0)}$, $\boldsymbol{\beta}^{(0)}$ and $\boldsymbol{b}^{(0)}$, with the optimal values.
3) Build the SDM-FPA-ELM-TF model for a passive component. The transfer function is used to represent the EM responses versus frequency. SDM-FPA-ELM is used to learn the relationship between the geometrical variations of the component and the coefficients of transfer functions through the training process.
4) Train the SDM-FPA-ELM-TF model with collected training data to find the optimal values of weights and thresholds of ELM.
5) Test the SDM-FPA-ELM-TF model with collected testing data.

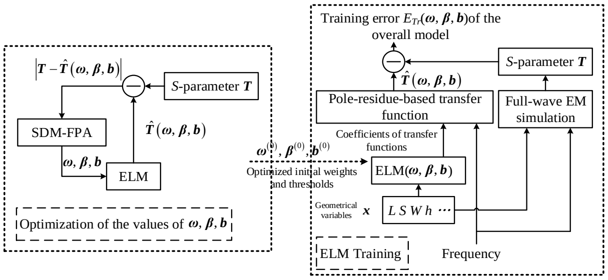

Fig. 2. SDM-FPA-ELM-TF model.

III. APPLICATION EXAMPLES

In this section, a quadruple-mode filter is used as an application example to evaluate the proposed SDM-FPA-ELM model. The *HFSS* 15.0 software performs the full-wave EM simulation and generates the training and testing data for modeling. The design of experiments (DOE) method is used for sampling [12]. All calculations in this paper are performed on an Intel i7-4870 2.50 GHz machine with 16 GB RAM.

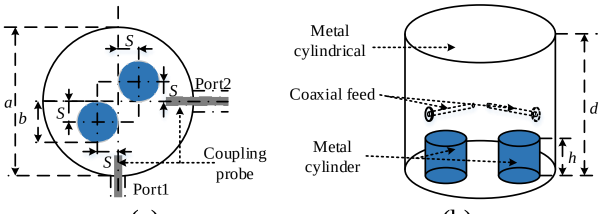

(a) (b)

Fig. 3. Structure of the quadruple-mode filter. (a) Top view. (b) Three dimensional view.

The structure of a quadruple-mode filter is illustrated in Fig. 3, where the height and diameter of the cavity are d and a, the height and diameter of the two perturbation metal cylinders of the intra-cavity are h and b, and the distance between the two metal cylinders is $2\sqrt{2}S$ [13]. The model has five input geometrical variations, i.e., $\boldsymbol{x}$ = $[a\ b\ S\ h\ d]^T$. Frequency is an additional input parameter with an original range of 1-5

GHz. The model has two outputs, i.e., $\boldsymbol{y} = [R_{S11}\ I_{S11}]^T$, where R_{S11} is the real part of S_{11} and I_{S11} is the image part of S_{11}.

Table 2: Definition of training and testing data for the quadruple-mode filter

Geometrical Variations	Training Data (49 Samples)			Testing Data (25 Samples)		
	Min	Max	Step	Min	Max	Step
a (mm)	44	56	2	45	53	2
b (mm)	12	18	1	12.5	16.5	1
S (mm)	2	8	1	2.5	6.5	1
h (mm)	14	20	1	14.5	18.5	1
d (mm)	44	56	2	45	53	2

The DOE method with seven levels defines the training samples, i.e., a total of 49 training samples, and DOE with five levels defines the testing data, i.e., a total of 25 testing samples. The information of training data and testing data is shown in Table 2. The total CPU time for training-data generation from EM simulations is about 1.225 hours, and the total time for testing-data generation is about 0.625 hours. After the modeling process, the average training percentage error is 0.385%, while the average testing percentage error is 0.587%.

Table 3: Comparison between the reference model and proposed model for the quadruple-mode filter

49 Training Samples and 25 Testing Samples	Average Training Error	Average Testing Error
Reference model in [7]	2.904%	4.862%
Proposed model	0.385%	0.587%
81 Training Samples and 49 Testing Samples	Average Training Error	Average Testing Error
Reference model in [7]	1.431%	1.509%
Proposed model	0.407%	0.598%

The model in [6] is employed for comparison here. The DOE methods with nine levels (81 samples) and seven levels (49 samples) are respectively used for training and testing in the reference model. The total time for training-data generation from EM simulations is about 2 hours, and the total time for testing-data generation is about 1.225 hours. With 49 training samples, as shown in Table 3, the proposed model achieves the acceptable accuracy, but the desired accuracy cannot be obtained with the reference model. When the number of training sample rises to 81, the accuracy of reference model is enhanced. It is observed that fewer training samples are needed for the proposed model to obtain an accurate trained model. It means that, to achieve the same accuracy, considerable simulation time could be saved with the proposed model for sample collection, as illustrated in Table 4.

Table 4: Running time of the two models for the quadruple-mode filter

	CPU Time of Model Development	
	Reference Model in [7]	Proposed Model
Training process	4 hours (81 samples)	2.45 hours (49 samples)
Testing process	2.45 hours (49 samples)	1.25 hours (25 samples)
Total	6.45 hours	3.7 hours

Figure 4 shows the outputs of two different test geometrical samples of the quadruple-mode filter with the proposed model, comparison model and HFSS simulation. The geometrical variables for the two samples in the range of the training data are $\boldsymbol{x}_1 = [45.6\ 15.6\ 7.2\ 17.1\ 48.1]^T$ and $\boldsymbol{x}_2 = [52.3\ 11.8\ 6.3\ 19.4\ 45.8]^T$. It is observed that the proposed model can achieve good accuracy for different geometrical samples even though these samples are never used in training.

Meanwhile, two other test geometrical samples, which are selected out of the range of the training data, are chosen to evaluate the proposed model. The geometrical variations for the two samples are $\boldsymbol{x}_1^{'} = [40\ 10\ 0\ 12\ 40]^T$ and $\boldsymbol{x}_2^{'} = [40\ 9\ 10\ 22\ 60]^T$. From Fig. 5, it is observed that our model can achieve good accuracy for different geometrical samples even though these samples are out of the range of the training data.

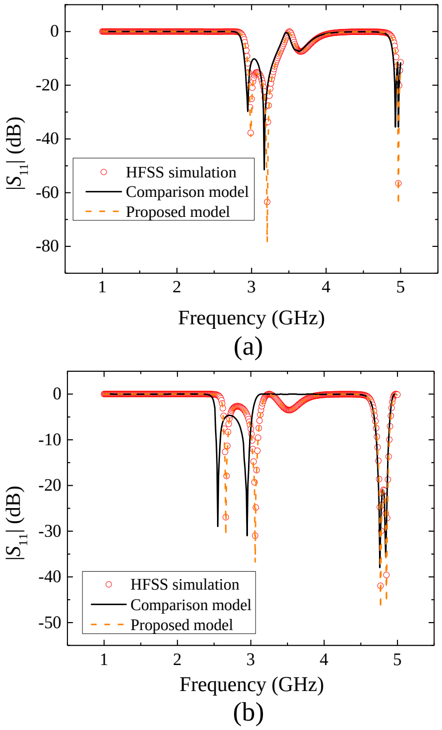

Fig. 4. Comparison of S_{11}: (a) Sample 1 and (b) Sample 2, where the samples are in the range of training data.

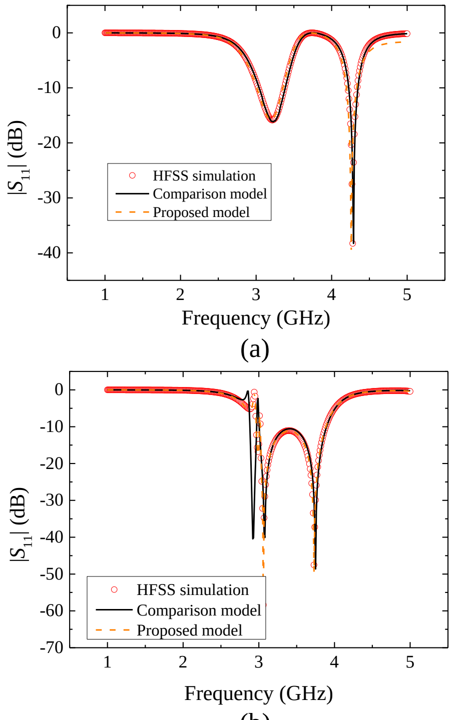

(a)

(b)

Fig. 5. Comparison of S_{11}: (a) Sample 1 and (b) Sample 2, where the samples are out of the range of training data.

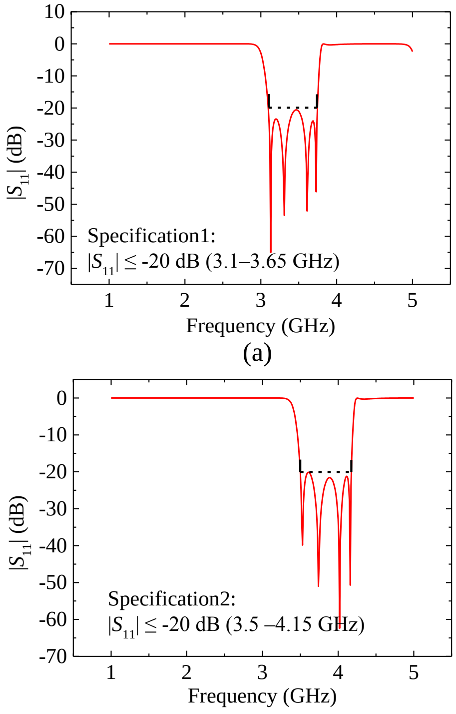

(a)

(b)

Fig. 6. Optimization results of S_{11} from the proposed model: (a) Filter 1 and (b) Filter 2.

Once the proposed model training is completed, the trained model which is a substitute for the time-consuming EM simulation can be applied to the design optimization. As an example of filter design, two separate filters are optimized to reach two different design specifications. The optimization objectives and results are shown in Fig. 6. The initial values are $\boldsymbol{x}$ = $[50\ 15\ 4\ 17\ 50]^T$. The optimization with SDM-FPA of the quadruple-mode filter is performed by calling the trained model repeatedly. The optimized geometrical values for the two separate filters are: $\boldsymbol{x}_{\text{opt1}}$ = $[50.0234\ 14.4081\ 7.4103\ 14.8103\ 44.9081]^T$ and $\boldsymbol{x}_{\text{opt2}}$ = $[49.9802\ 13.9841\ 7.2004\ 14.7903\ 45.3094]^T$.

The optimization spends only about 30 seconds to achieve the optimal solution for each filter, shown in Table 5. The proposed model could save considerable time in optimization design compared with the calling of EM simulations.

Table 5: Running time of the direct EM optimization and the proposed model

	CPU Time of Model Development	
	Direct EM Optimization	SDM-FPA-ELM-TF Model
Filter 1	10 hours	30 s
Filter 2	11 hours	30 s
Total	21 hours	3.7 hours (training)+60 s

IV. CONCLUSION

In this paper, an efficient ELM model based on a modified SDM-FPA is proposed to enhance the learning effectiveness in EM simulations. SDM-FPA is developed to set the optimal initial weights and thresholds of ELM and it saves more training costs. In this method, SDM-FPA-ELM is used to learn the relationship between the geometrical variations of filters and the coefficients of transfer functions through the training process. Compared with the reference model, the proposed model can achieve the trained model with small training samples due to its good iteration learning ability. A quadruple-mode filter is employed as a parametric modeling example to confirm its validity. The proposed model provides its powerful computing ability, especially in the field of EM optimization design.

ACKNOWLEDGMENT

This work was supported by the National Natural Science Foundation of China (No. 61471105) and 973 Project (No. 613273).

REFERENCES

[1] J. E. Rayas-Sánchez, “EM-based optimization of microwave circuits using artificial neural networks: The state-of-the-art,” *IEEE Trans. Microw. Theory Techn.*, vol. 52, no. 1, pp. 420-435, Jan. 2004.

[2] V. Rizzoli, A. Costanzo, D. Masotti, A. Lipparini,

and F. Mastri, “Computer-aided optimization of nonlinear microwave circuits with the aid of electromagnetic simulation,” *IEEE Trans. Microw. Theory Techn*., vol. 52, no. 1, pp. 362-377, Jan. 2004.

[3] X. Ding, V. K. Devabhaktuni, B. Chattaraj, M. C. E. Yagoub, M. Deo, J. Xu, and Q. J. Zhang, “Neural-network approaches to electromagnetic based modeling of passive components and their applications to highfrequency and high-speed nonlinear circuit optimization,” *IEEE Trans. Microw. Theory Techn*., vol. 52, no. 1, pp. 436-449, Jan. 2004.

[4] Q. J. Zhang, K. C. Gupta, and V. K. Devabhaktuni, “Artificial neural networks for RF and microwave design—From theory to practice,” *IEEE Trans. Microw. Theory Techn.*, vol. 51, no. 4, pp. 1339-1350, Apr. 2003.

[5] Y. F. Yam, T. W. S. Chow, and C. T. Leung, “A new method in determining initial weights of feed forward neural networks for training enhancement,” *Neurocomputing*, vol. 16, pp. 23-32, 1997.

[6] G. B. Huang, Q. Y. Zhu, and C. K. Siew, “Extreme learning machine: Theory and applications,” *Neurocomputing*, vol. 70, no. 1-3, pp. 489-501, 2006.

[7] F. Feng, C. Zhang, J. Ma, and Q. J. Zhang, “Parametric modeling of EM behavior of microwave components using combined neural networks and pole-residue-based transfer functions,” *IEEE Trans. Microw Theory Techn.*, vol. 64, no. 1, pp. 60-77, Jan. 2016.

[8] X. S. Yang, “Flower pollination algorithm for global optimization,” in *Proc. of the 11th Int'l. Conf. on Unconventional Computation and Natural Computation (UCNC)*, Orléans, France, pp. 242-243, Sept. 2012.

[9] E. Nabil, “A modified flower pollination algorithm for global optimization,” *Expert. Syst. Appl.*, vol. 57, pp. 192-203, 2016.

[10] G. B. Huang, Q. Y. Zhu, and C. K. Siew, “Extreme learning machine: Theory and applications,” *Neurocomputing*, vol. 70, no. 1-3, pp. 489-501, 2006.

[11] X. Shi, J. Wang, G. Liu, L. Yang, X. Ge, and S. Jiang, “Application of extreme learning machine and neural networks in total organic carbon content prediction in organic shale with wire line logs,” *J. Nat. Gas. Sci. Eng.*, vol. 33, pp. 687-702, 2016.

[12] S. R. Schmidt and R. G. Launsby, “Understanding Industrial Designed Experiments,” Colorado Springs, CO, USA, Air Force Academy, 1992.

[13] S. W. Wong, S. F. Feng, L. Zhu, and Q. X. Chu, “Triple- and quadruple-mode wideband bandpass filter using simple perturbation in single metal cavity,” *IEEE Trans. Microw Theory Techn.*, vol. 63, no. 10, pp. 1-9, Oct. 2015.

Li-Ye Xiao received the B.S. degree in Electronic Information Science and Technology from the University of Electronic Science and Technology of China (UESTC), Chengdu, China, in 2015. Currently, he is working toward the Ph.D. degree in Radio Physics at UESTC.

His research interest is neural network, optimization algorithm and computational electromagnetics.

Wei Shao received the B.E. degree in Electrical Engineering from UESTC in 1998, and received M.Sc. and Ph.D. degrees in Radio Physics from UESTC in 2004 and 2006, respectively.

He joined the UESTC in 2007 and is now a Professor there. From 2010 to 2011, he was a Visiting Scholar in the Electromagnetic Communication Laboratory, Pennsylvania State University, State College, PA. From 2012 to 2013, he was a Visiting Scholar in the Department of Electrical and Electronic Engineering, Hong Kong University. His research interests include computational electromagnetics and antenna design.

Sheng-Bing Shi received the B.S. degree in Physics from the Yangtze University, Jingzhou, China, in 2013. Currently, he is working toward the Ph.D. degree in Radio Physics at UESTC.

His research interest is computational electromagnetics.

Bing-Zhong Wang received the Ph.D. degree in Electrical Engineering from UESTC in 1988.

He joined the UESTC in 1984 where he is currently a Professor. He has been a Visiting Scholar at the University of Wisconsin-Milwaukee, a Research Fellow at the City University of Hong Kong, and a Visiting Professor in the Electromagnetic Communication Laboratory, Pennsylvania State University, State College, PA. His current research interests are computational electromagnetics and antenna theory.

Modelling of Interbranch Coupled 1:2 Tree Microstrip Interconnect

B. Ravelo [1], A. Normand [2], and F. Vurpillot [2]

[1] Normandy University, UNIROUEN, ESIGELEC, IRSEEM EA 4353
Technopole du Madrillet, Avenue Galilée, BP 10024, F-76801 Saint Etienne du Rouvray, France

[2] Normandy University UNIROUEN, GPM UMR 6643, F-76000 Rouen, France
ravelo@esigelec.fr

Abstract **─** A computational method of unbalanced single-input two-output (1:2) interconnect with coupled interbranch is introduced. The circuit theory is built with the topology constituted by the octopole Z-matrix represented by the coupled lines. The voltage transfer functions (VTFs) and the input impedance of the input-output electrical path of the unbalanced 1:2 tree with interbranch coupled lines are established. The computation model is verified with proofs of concept (POC) constituted by unbalanced 1:2 tree microstrip structure with and without interbranch coupled phenomenon. The POCs are loaded by resistors and capacitors. Good agreements between the simulated and modelled VTFs and the overall structure input impedances were obtained from 0.1-to-2 GHz.

Index Terms **─** Circuit theory, coupled lines, microstrip interconnect, modelling methodology, transmission line, tree network,

I. INTRODUCTION

With the increase of the integration density and design complexity, the printed circuit board (PCB) performance depends on the interconnect effects [1]. The PCB interconnects play important roles during the design and manufacturing. The PCB design technological roadblocks consist in the interconnect effects modelling. The high-density interconnects cause unintentionally the transmitted signal distortions, latency due to the degradation generated by unwanted perturbations. To predict these breakthroughs, intensive research works have been performed high speed PCB signal distribution interconnect computational methods [2-4]. The PCB interconnect design requires consistent transmission line (TL) model. It enables to predict the signal degradation and unintentional effects. The PCB interconnect computation becomes one of the most attractive research topics of electronic design and manufacturing [2-4]. Initially, the PCB, packaged and integrated circuits (ICs) interconnect network was modeled with first order approximation of the equivalent transfer function by Elmore in 1948 [5]. The initial computational model is elaborated with RC-network. It presents advantages in terms of simplicity and its possibility for fast delay estimation of different paths of integrated system. However, the Elmore model accuracy is drastically decreasing when the signal speed is increased. Therefore, this computation method is limited to simple interconnect networks. Therefore, further improvement is required to increase the accuracy. In late 1970s, improved RC network model was introduced by Wyatt [6-7]. In 1980s, the improved model was widely used. Significant performance of the signal delay modelling for the typically linear RC-meshes of tree networks was performed [7-8]. In 1990s, the RC-model was extended to the prediction of the behaviors of more complex networks as dominant time constant MOS VLSI circuit design and manufacturing [9]. The employed computation algorithm for estimating the propagation delay times for multi-levels of tree mesh networks composed of cascaded RC-cells is to sum the delays at each node of the circuits. Nevertheless, the RC-tree network model is less efficient when the PCB operating signal speed is increased.

Recently, more accurate second order approximated RLC model taking into account the inductance effect with closed form of delay times (propagation, rise/fall and settling time delays) were developed [10-11]. The modelling method allowing to determine the unit step response of RLC tree networks from second moments of the polynomial transfer function was proposed [11]. More accurate tree model promising to approximate the over- or under-damped responses and the basic characteristics as the second order propagation delay expression were also deployed [11]. Moreover, modelling and simulation techniques of TL networks were suggested [12]. The second order model was also employed for estimating the delay associated to non-monotone time-domain responses of high speed tree interconnect networks [13-14]. The RLC-model was extended to the modelling of high performance interconnection structures as on-chip architecture buses,

Submitted On: July 10, 2017
Accepted On: October 4, 2017

multiphase multiplexer clock system [15] and arbitrary level high-speed digital-analog converters [16]. However, the accuracy of these models and the computation time needs to be improved when the tree distribution level is higher. To face out this limitation, more general behavioral model for extracting the analytical transfer function of multi-levels of signal distributed tree networks was developed in [17-19]. This PCB tree interconnect network model is fundamentally consisted of cascaded L-cells and distributed TLs. By using the transfer matrix theory, the whole network transfer function was expressed. However, the available model of PCB tree interconnects does not integrate the electromagnetic (EM) crosstalk and coupling problem between the interconnect line branches [20-21]. The crosstalk affects the system of serial links as in the mobile terminal emitter [21].

For this reason, the unbalanced tree interconnects modelling with interbranch EM coupling effect is developed in this paper. Section II describes the computational theory of interbranch coupled unbalanced single-input double-output (1:2) tree. Section III is the unbalanced 1:2 tree input impedance and the voltage transfer functions (VTFs) model validations with Advanced Design System (ADS®) simulations. Section IV is the conclusion.

II. INTERBRANCH COUPLED 1:2 TREE INTERCONNECTS MODEL

The proposed computational method is aimed to the determination of the input impedance and the unbalanced tree interconnect VTFs. In difference with the existing models, the proposed one integrates the coupling phenomenon interbranch of the unbalanced tree interconnects. In more concrete view, the tree under study is composed of elementary TLs configured as depicted in Fig. 1.

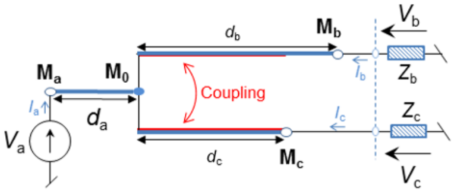

Fig. 1. Unbalanced tree interconnect structure.

The electrical network is constituted by three branches TL_{MaM0}, TL_{M0Mb} and TL_{M0Mc}. The characteristic impedances and physical lengths are respectively (Z_a,d_a), (Z_b,d_b) and (Z_c,d_c) by supposing that $d_b > d_c$. Moreover, the output branches TL_{M0Mb} and TL_{M0Mc} are implicitly with EM coupling phenomenon.

A. Equivalent circuit topology

The posed problem can be traduced by the unbalanced 1:2 tree interconnect modelling. It consists in the transformation of the initial tree network introduced in Fig. 1 into the systemic model depicted in Fig. 2. The voltages across the nodes M_a, M_b and M_c are respectively denoted $V_a=V_{Ma}$, $V_b=V_{Mb}$ and $V_c=V_{Mc}$.

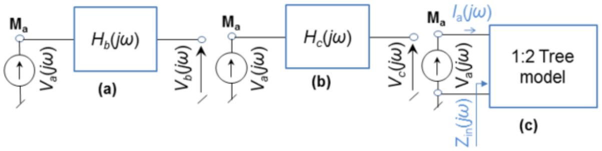

Fig. 2. VTF equivalent circuit systemic view: (a) H_a, (b) H_b, and (c) input impedance Z_{in}.

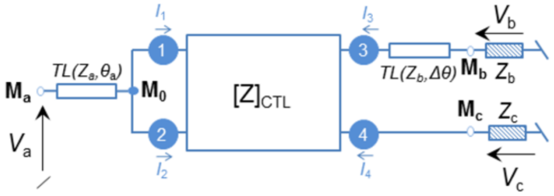

Fig. 3. Equivalent circuit diagram of the unbalanced tree interconnect including the CTL Z-matrix.

The system VTFs and overall input impedance are defined by:

$$H_b(j\omega)=V_{M_b}(j\omega)/V_{M_a}(j\omega)=V_b(j\omega)/V_a(j\omega)\,, \tag{1}$$

$$H_c(j\omega)=V_{M_c}(j\omega)/V_{M_a}(j\omega)=V_c(j\omega)/V_a(j\omega)\,, \tag{2}$$

$$Z_{in}(j\omega)=V_a(j\omega)/I_a(j\omega)\,, \tag{3}$$

with ω is the angular frequency. The equivalent circuit diagram of the unbalanced 1:2 tree can be elaborated by considering the impedance- or Z-matrix of the coupled TL (CTL). The modelling method can be established from the equivalent circuit diagram presented in Fig. 3. The unbalanced tree structure can be transformed as an electrical network mainly constituted by elementary TLs. We assume that the input is connected the TL TL_{MaM0} characterized by $TL(Z_a(j\omega),\gamma_a(j\omega))$. TL_{M0Mb} and TL_{M0Mc}, respectively characterized by $TL(Z_b(j\omega),\gamma_b(j\omega))$ and $TL(Z_c(j\omega),\gamma_c(j\omega))$ constitute the output branches. With $\xi=\{a,b,c\}$, $Z_\xi(j\omega)$ is the characteristic impedance and $\gamma_\xi(j\omega)=\alpha_\xi(\omega)+j\beta_\xi(\omega)$ is the propagation constant (ω is the angular frequency, α_ξ is the attenuation constant, β_ξ phase constant associated to the electrical length $\theta_\xi=\beta_\xi d_\xi$). These output networks can be represented by the coupled TL matrix $[Z]_{CTL}$ and the output TL $TL(Z_b(j\omega),\Delta\gamma(j\omega))$ associated to the electrical length $\Delta\theta$. This CTL structure is assumed as an octopole with Ports ❶ and ❷ interconnected, and Ports ❸ and ❹ are connected to output loads R_b and R_c. Each access port m ($m=\{1,2,3,4\}$) is traversed by branch currents I_m.

Let us denote C the coupling coefficient between the coupled lines connecting Ports ❶ and ❷, and Ports

❸ and ❹ and $Z_0(j\omega)$ is the characteristic impedance of each elementary line. According to the TL theory, the even- and odd-characteristic impedances of the associated coupled lines constituting the unbalanced 1:2 tree is defined as $Z_e=Z_0[(1+C)/(1-C)]^{0.5}$ and $Z_o=Z_0[(1-C)/(1+C)]^{0.5}$. The lengths of the input and output TLs can be characterized by the resonance angular frequencies ω_ξ which are linked to the physical length by the relation $d_\xi=2\pi v/\omega_\xi$ with $\xi=\{a,b,c\}$ and the wave speed v. Moreover, the physical length difference $\Delta d=d_b-d_c$ between the TL_{M0Mb} and TL_{M0Mc} corresponding to the quarter wavelengths $\lambda_b/4$ and $\lambda_c/4$ is also equivalent to the electrical length analogue to the overlength TL connecting Port ❸ and node M_b. The equivalent electrical length is associated to Δd. It is analytically equal to $\Delta\theta=\beta_b\Delta d=\beta_b(d_b-d_c)$. It implies the relation $\Delta\theta=\pi\omega(\omega_c-\omega_b)/(2\omega_b\cdot\omega_c)$. The associated input impedance, which is spontaneously related to the TL characteristic impedance $Z_0(j\omega)$, is given by $Z(j\omega)=Z_0(j\omega)/\tanh\left[\Delta\gamma(j\omega)\right]$.

B. Z-Matrix of the coupled output branches and access line ABCD or transfer matrices

The adopted methodology to solve the posed-problem is fundamentally based on the calculation of the branch currents. The Z-matrix of the tree coupled branches and the access line ABCD matrices must be expressed in function of the interconnect structure parameters. The four-port CTL structure constituting the unbalanced 1:2 tree can be represented by the equivalent 4×4 Z-matrix analytically expressed as:

$$[Z]=\begin{bmatrix} Z_{11} & Z_{12} & Z_{13} & Z_{14}\\ Z_{21} & Z_{22} & Z_{23} & Z_{24}\\ Z_{31} & Z_{32} & Z_{33} & Z_{34}\\ Z_{41} & Z_{42} & Z_{43} & Z_{44}\end{bmatrix}. \quad (4)$$

By denoting α the attenuation constant and d the physical length, based on the microwave theory and due to the symmetry, the matrix elements are defined as:

$$\begin{cases} Z_{11}=Z_{22}=Z_{33}=Z_{44}=\dfrac{Z_e+Z_o}{2\tanh(\alpha d+j\theta)}\\ Z_{12}=Z_{21}=Z_{34}=Z_{43}=\dfrac{Z_e-Z_o}{2\tanh(\alpha d+j\theta)}\\ Z_{13}=Z_{31}=Z_{24}=Z_{42}=\dfrac{Z_e-Z_o}{2\sinh(\alpha d+j\theta)}\\ Z_{14}=Z_{41}=Z_{23}=Z_{32}=\dfrac{Z_e+Z_o}{2\sinh(\alpha d+j\theta)}\end{cases}, \quad (5)$$

with $\theta=\pi\omega/(2\omega_c)$. Furthermore, the ABCD matrices analytically equivalent to the TL connecting the node M_a-Port ❶, and Port ❸-node M_b are respectively defined as [17-18]:

$$[T_a]=\begin{bmatrix} A_a & B_a\\ C_a & D_a\end{bmatrix}=\begin{bmatrix} \cosh(\gamma_a) & Z_a\sinh(\gamma_a)\\ \sinh(\gamma_a)/Z_a & \cosh(\gamma_a)\end{bmatrix}, \quad (6)$$

$$[T_b]=\begin{bmatrix} A_b & B_b\\ C_b & D_b\end{bmatrix}=\begin{bmatrix} \cosh(\Delta\gamma) & Z_{b_0}\sinh(\Delta\gamma)\\ \sinh(\Delta\gamma)/Z_{b_0} & \cosh(\Delta\gamma)\end{bmatrix}. \quad (7)$$

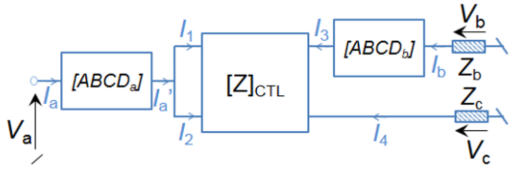

Fig. 4. Reduced two-port equivalent network of the circuit introduced in Fig. 2.

The abstracted topology equivalent to the unbalanced 1:2 tree structure under study can be represented as highlighted in Fig. 4. This topology enables to realize the theorization of the problem with the analogue mathematical concept. The branch currents $[I_1,I_2,I_3,I_4,I_a,I_b]$ are assumed as the unknown variables which must be expressed in function of the input excitation source V_a. Meanwhile, the problem solution can be reformulated as the calculation of the tree branch currents I_a, I_a', I_1, I_2, I_3, I_4 and I_b. The algebraic solution can be determined from linear equations derived via the combination of the impedance- and ABCD-matrices in (4), (6) and (7), and the Ohm's laws applied to the output loads Z_b and Z_c:

$$V_b=-Z_b\cdot I_b, \quad (8)$$

$$V_4=-Z_c\cdot I_4. \quad (9)$$

Moreover, at the junction node M_0, we have the relation $I_a'=I_1+I_2$ and $V_1=V_2$. By taking this condition into account, the following synthetic equation system can be deduced from the access line ABCD matrices associated to (8) and (9):

$$\begin{cases} V_a=A_aV_1+B_a(I_1+I_2)\\ I_a=C_aV_1+D_a(I_1+I_2)\\ V_3=A_bV_b-B_bI_b=-(A_bZ_b+B_b)I_b\\ I_3=C_bV_b-D_bI_b=-(C_bZ_b+D_b)I_b\end{cases}. \quad (10)$$

The voltage and current vectors $[V]=[V_1V_2V_3V_4]$ and $[I]=[I_1\,I_2\,I_3\,I_4]$ corresponding to the configuration of the coupled lines presented in the circuit diagram of Fig. 3 are linked to the Z-matrix defined in (4) by the equation system:

$$[V]=[Z]_{CPTL}[I]\Leftrightarrow\begin{cases}V_1=Z_{11}I_1+Z_{12}I_2+Z_{13}I_3+Z_{14}I_4\\V_1=Z_{21}I_1+Z_{22}I_2+Z_{23}I_3+Z_{24}I_4\\V_3=Z_{31}I_1+Z_{32}I_2+Z_{33}I_3+Z_{34}I_4\\V_4=Z_{41}I_1+Z_{42}I_2+Z_{43}I_3+Z_{44}I_4\end{cases}. \quad (11)$$

C. VTF and input impedances of the tree input-output electrical path

The combination of (10) and (11) implies the following synthetic characteristic equation system of the posed-problem mathematical solution knowing the excitation source V_a in (12). The main access branch currents I_a and I_b can be yielded from the solutions via the ABCD matrices of TLs TL$_{\text{MaM0}}$ and TL$_{\text{Port❸-Mb}}$ in (13). Consequently, the unbalanced 1:2 tree characteristic matrix derived from (12) and (13) can be written in (14):

$$\begin{cases}(Z_{11}+\dfrac{B_a}{A_a})I_1+(Z_{12}+\dfrac{B_a}{A_a})I_2+Z_{13}I_3+Z_{14}I_4=\dfrac{V_a}{A_a}\\(Z_{21}+\dfrac{B_a}{A_a})I_1+(Z_{22}+\dfrac{B_a}{A_a})I_2+Z_{23}I_3+Z_{24}I_4=\dfrac{V_a}{A_a}\\Z_{31}I_1+Z_{32}I_2+(Z_{33}-\dfrac{A_bZ_b+B_b}{C_bZ_b+D_b})I_3+Z_{34}I_4=0\\Z_{41}I_1+Z_{42}I_2+Z_{43}I_3+(Z_{44}+Z_c)I_4=0\end{cases}, \quad (12)$$

$$\begin{cases}I_a=\left[C_aV_a+(D_aA_a-B_a)(I_1+I_2)\right]/A_a\\I_b=-I_3/(C_bZ_b+D_b)\end{cases}, \quad (13)$$

$$\begin{bmatrix}\dfrac{V_a}{A_a}\\\dfrac{V_a}{A_a}\\0\\0\\\dfrac{C_a}{A_a}V_a\\0\end{bmatrix}=\begin{bmatrix}Z_{11}+\dfrac{B_a}{A_a} & Z_{12}+\dfrac{B_a}{A_a} & Z_{13} & Z_{14} & 0 & 0\\Z_{21}+\dfrac{B_a}{A_a} & Z_{22}+\dfrac{B_a}{A_a} & Z_{23} & Z_{24} & 0 & 0\\Z_{31} & Z_{32} & Z_{33}-\dfrac{A_bZ_b+B_b}{C_bZ_b+D_b} & Z_{34} & 0 & 0\\Z_{41} & Z_{42} & Z_{43} & Z_{44}+Z_c & 0 & 0\\\dfrac{B_a}{A_a}-D_a & \dfrac{B_a}{A_a}-D_a & 0 & 0 & 1 & 0\\0 & 0 & 1 & 0 & 0 & C_bZ_b+D_b\end{bmatrix}\begin{bmatrix}I_1\\I_2\\I_3\\I_4\\I_a\\I_b\end{bmatrix}. \quad (14)$$

By taking $x=\tanh(\alpha d+j\theta)$, the VTF through the 1:2 tree electrical path M$_a$M$_b$ can be expressed as:

$$H_b(j\omega)=\frac{Z_b(j\omega)I_b(j\omega)}{-V_a(j\omega)}=\frac{2Z_eZ_b(Z_c+xZ_o)\sqrt{1-x^2}}{\chi_2^bx^2+\chi_1^bx+\chi_0^b}, \quad (15)$$

where

$$\begin{cases}\chi_2^b=2Z_o\begin{bmatrix}B_a((B_b+A_aZ_b)-(D_b+C_bZ_b)Z_c)\\-A_a(D_b+C_bZ_b)Z_e^2\end{bmatrix}\\\chi_1^b=\begin{Bmatrix}A_a(A_aZ_b+B_b-(D_b+C_bZ_b)Z_c)Z_e^2\\+4B_a(B_b+A_aZ_b)Z_c\\+\begin{bmatrix}A_a(4A_aZ_b+B_b)-(4B_a(D_b+C_bZ_b)\\+A_aD_bZ_c+A_aC_bZ_bZ_c)\end{bmatrix}Z_oZ_e\end{Bmatrix}\\\chi_0^b=2Z_eB_a\begin{bmatrix}B_a(B_b+A_aZ_b)+Z_c(A_aB_b-B_aD_b\\+(A_a^2-B_aC_b)Z_b))\end{bmatrix}\end{cases}. \quad (16)$$

Similarly, the VTF equivalent to the electrical path M$_a$M$_c$ can be written as:

$$H_c(j\omega)=\frac{Z_c(j\omega)I_4(j\omega)}{-V_a(j\omega)}=\frac{2Z_cZ_e\sqrt{1-x^2}\left[Z_ox(C_bZ_b+D_b)+B_b+A_aZ_b\right]}{\chi_2^bx^2+\chi_1^bx+\chi_0^b}. \quad (17)$$

The overall structure input impedance can be extracted from (3).

III. VALIDATION RESULTS

This section is focused on the validations of the developed unbalanced 1:2 model. Two POC of unbalanced 1:2 trees are designed by considering the aspects with and without interbranch coupled branches. The POC modelled computed results are compared with simulations run in the ADS® environment of the electronic circuit designer and simulator. AC simulations are considered by assigning the voltage excitation source V_a with 201 frequency samples from 0.1 GHz to 2 GHz.

A. Description of the POC

The POC represented in 3D view in Figs. 5 are microstrip passive distributed circuits which are interconnect passive structures of unbalanced 1:2 tree networks. The arbitrarily chosen structures with and without output interbranch coupling are respectively shown in Fig. 5 (a) and Fig. 5 (b).

These microstrip structures were printed on the dielectric substrate Kapton® polyimide film provided by DuPont® with characteristics relative permittivity ε_r=3.3, loss tangent tan(δ)= 0.008, thickness h=125 µm, conductivity σ=58 MS/m and thickness t=17 µm. Both sides of the film were laminated with copper layer, forming the ground plane for the unbalanced 1:2 tree interconnects circuit, and the layer on which the circuit was patterned respectively. Knowing the POC characteristics, the demonstrator circuit was designed with elementary lines presenting arbitrary physical parameters. The POCs with and without interbranch coupling presents physical sizes are respectively 28 mm×75 mm and 122 mm×29 mm.The POC structures are excited by the AC voltage source V_a and loaded by Z_b and Z_c connected at the output nodes M_b and M_c. Acting as an AC or frequency analysis, the input voltage source was fixed equal to constant V_a=1 V for the discrete frequency f varied from 0.1-to-2 GHz with 201 frequency samples.

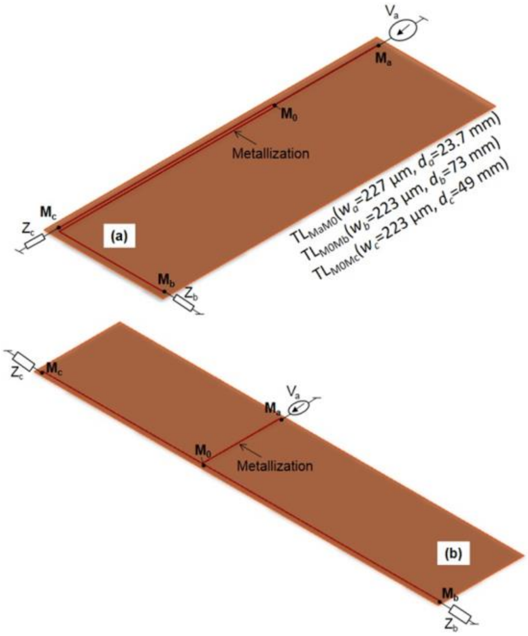

Fig. 5. 3D design of the POC asymmetrical 1:2-tree microstrip structure: (a) with and (b) without output interbranch coupling.

B. POC circuit physical, electrical and EM characteristics

The POC were designed with arbitrary parameters which prove the influence of the interbranch coupling on the two VTFs. The microstrip line effective permittivity and characteristic impedances were extracted based on the microstrip TL theory. The coupled branch parameters (C=-10 dB, Z_e=69.37 Ω, Z_o=36.04 Ω, s=40 µm) were extracted. The modelling and simulations were performed with these different parameters. However, the entire proposed model computed results were realized with Matlab programming. During the calculations, the ideal parameters were supposed independent to the frequency and the TL losses were neglected. The equivalent model was developed by assuming the TL_{MaM0}(w_a=227 µm, d_a=23.7 mm, Z_a=50 Ω) with the frequency quarter wavelength f_a=2 GHz and the coupled lines TL_{M0Mb}(w_b=223 µm, d_b=73 mm, Z_b=56.5 Ω) and TL_{M0Mc}(w_c=223 µm, d_c=49 mm, Z_c=56.5 Ω) are defined with the frequency quarter wavelengths f_b=1 GHz and Δf=2 GHz. The minimal physical width of the microstrip structure which can be fabricated with the equipment available in our laboratory is limited to 300 µm. For this reason, the POC fabricated prototypes are not available for the present study. The branch currents were computed.

C. Applications with resistive loaded unbalanced tree

In this case, the impedance loads are assigned as lumped resistors with nominal values Z_b=50 Ω and Z_c=100 Ω. The VTF magnitudes $|H_a|$ and $|H_b|$ are respectively displayed in Fig. 6 (a) and Fig. 6 (b). These results illustrate the relevance and effective of the developed model for the interbranch coupling phenomenon prediction. Without coupling, more accentuated resonance effects are observed at the terminal M_a and M_b. The interbranch coupling effects can be predicted by the proposed computation method in good agreement with the simulations from very low frequencies to 2 GHz. The same remark is found with the input impedance magnitude $|Z_{in}|$ of the overall structure plotted in Fig. 7. The VTF model accuracy presents error absolute maximal value of about 1 dB. The highest absolute differences between the simulations and modelled results are reasonably appeared around the resonance frequencies. The main difference between the model and the reference simulations are caused by the characteristics of the elementary TLs constituting the unbalanced tree structure. Furthermore, these discrepancies increase at higher frequencies. Such effects are mainly due to the influence of the frequency on the TL EM and electrical parameters as the skin depth effect and the substrate dispersion.

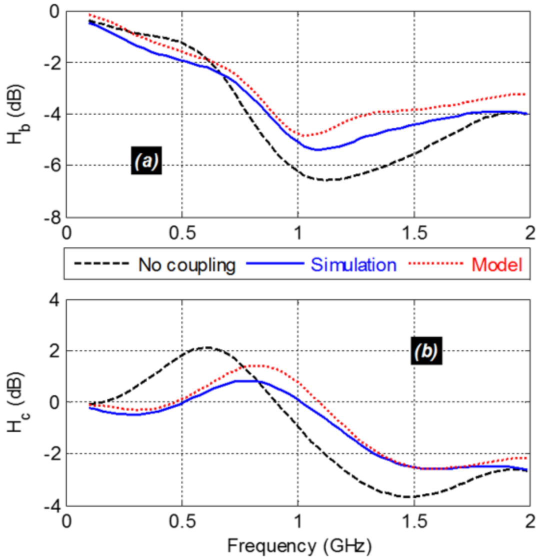

Fig. 6. Comparison of modelled and simulated resistive loaded tree interconnect VTF magnitudes: (a) $|H_b|$ and (b) $|H_c|$.

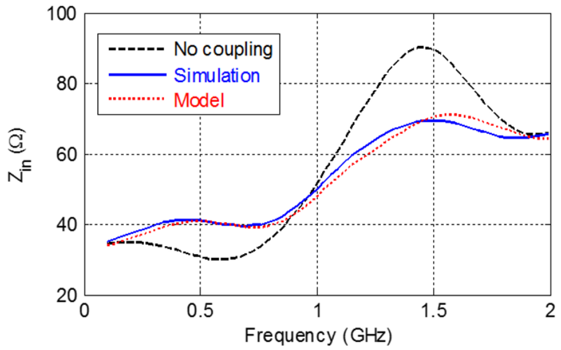

Fig. 7. Comparison of the modelled and simulated resistive loaded tree interconnect input impedance magnitude $|Z_{in}|$.

These computation errors are also added to the numerical computation inaccuracies.

To generate the modelled computed results with the assigned samples, the computation speed was less than one millisecond by using a PC equipped a single-core processor Intel® Core^{TM} i3-3120M CPU @ 2.50 GHz and 8 GB physical RAM with 64-bits Windows 7.

D. Applications with capacitive loaded unbalanced tree

In this case, the impedance loads are constituted by arbitrary chosen lumped resistor Z_b=50 Ω and capacitor Z_c=1 pF. The frequency simulations were carried out with the unbalanced 1:2 tree structure by sweeping the AC source V_a frequency. Then, comparison between the simulations and computed models is realized. The obtained VTF magnitudes $|H_a|$ and $|H_b|$ are respectively displayed in Fig. 8 (a) and Fig. 8 (b). Once again, without coupling, the resonance effects are occurred slightly at lower frequencies.The simulated and modelled VTFs are in good agreement for the different types of output loads Z_b and Z_c. A notable well-correlated behavior of the VTFs versus frequency is observed with simulations and the developed modelling methods in the considered broadband frequency band. The comparison between the associated input impedances magnitude $|Z_{in}|$ can be seen in Fig. 9. Similar to the previous case, the interbranch coupling influences obviously, the unbalanced tree frequency responses notably when the frequency is higher than 0.5 GHz. Despite the coherent behavior between the modeled and simulated results, numerical discrepancies appear around the resonance frequency situated between 0.5 GHz and 1 GHz.

This noteworthy deviation is mainly due to the approximation of the TL electrical and EM characteristics which are assumed to be independent to the frequency during the computation process.

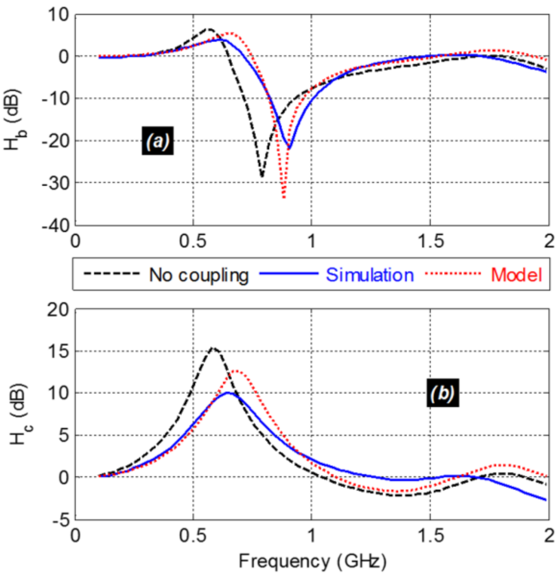

Fig. 8. Comparison of the modelled and simulated capacitive loaded tree interconnect VTF magnitudes: (a) $|H_b|$ and (b) $|H_c|$.

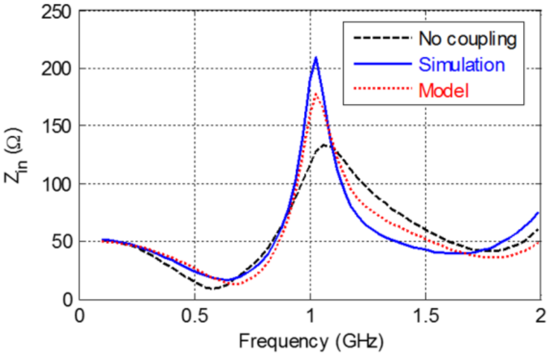

Fig. 9. Comparison of the modelled and simulated capacitive loaded tree interconnect input impedance magnitude $|Z_{in}|$.

IV. CONCLUSION

A circuit theory on 1:2 tree interconnects with interbranch coupling is established. The model is built with the combination of the coupled lines octopole impedance matrix and the access line ABCD matrices. The equivalent topology enables to traduce the system into the problem mathematical abstraction. The VTF of the tree input-output electrical path and the overall circuit input impedance are established. Two POCs constituted by unbalanced 1:2 tree with and without interbranch coupling are designed. The modeled and simulated tree input-output VTFs and also the input impedance are compared via AC simulations from 0.1-to-2 GHz. Good agreements between simulations and the models are observed. The proposed computation method is more efficient in terms of precision with the EM coupling influence compared to the methods available in [17-19] which are dedicated to the linear tree VTF modelling.

ACKNOWLEDGMENT

Acknowledgement is made to the Normandy Region for the BRIDGE project support of this research work through the FEDER fund.

REFERENCES

[1] C. Schuster and W. Fichtner, “Parasitic modes on printed circuit boards and their effects on EMC and signal integrity,” *IEEE Trans. EMC*, vol. 43, no. 4, pp. 416-425, Nov. 2001.

[2] H. Husby,“High Density Interconnect,”White Paper, Data Response. Available Online [2016]. http://www.datarespons.com/high-density-interconnect/

[3] B. Archambeault and A. E. Ruehli, “Analysis of power/ground-plane EMI decoupling performance using the partial-element equivalent circuit technique,” IEEE Trans. EMC, vol. 43, no. 4, pp. 437-445, Nov. 2001.

[4] K. M. C. Branch, J. Morsey, A. C. Cangellaris and A. E. Ruehli, “Physically consistent transmission line models for high-speed interconnects in lossy dielectrics,” *IEEE Trans. Advanced Packaging*, vol. 25, no. 2, pp. 129-35, Aug. 2002.

[5] W. C. Elmore, “The transient response of damped linear networks,” *J. Appl. Phys*., vol. 19, pp. 55-63, Jan. 1948.

[6] L. Wyatt, Circuit Analysis, Simulation and Design. North-Holland. The Netherlands: Elsiever Science, 1978.

[7] D. Standley and J. L. Wyatt, Jr., “Improved Signal Delay Bounds for RC Tree Networks,” VLSI Memo, No. 86-317, MIT, Cambridge, MAS (USA), May 1986.

[8] J. Rubinstein, P. Penfield, Jr., and M. A. Horowitz, “Signal delay in RC tree networks,” *IEEE Trans. CAD*, vol. 2, no. 3, pp. 202-211, July 1983.

[9] L. Vandenberghe, S. Boyd, and A. El Gamal, “Optimizing dominant time constant in RC circuits,” *IEEE Trans CAD*, vol. 17, no. 2, pp. 110-125, Feb. 1998.

[10] A. B. Kahng and S. Muddu, “An analytical delay model of RLC interconnects,” *IEEE Trans. CAD*, vol. 16, pp. 1507-1514, Dec. 1997.

[11] A. Ligocka and W. Bandurski, “Effect of inductance on interconnect propagation delay in VLSI circuits,” *Proc. of 8th Workshop on SPI*, Heidelberg, Germany, pp. 121-124, 9-12 May 2004.

[12] A. Deutsch, et al., “High-speed signal propagation on lossy transmission lines,” *IBM J. Res. Develop*., vol. 34, no. 4, pp. 601-615, July 1990.

[13] J. Cong, L. He, C. K. Koh, and P. H. Madden, “Performance optimization of VLSI interconnect layout,” *Integration VLSI J*., vol. 21, no. 1-2, pp. 1-94, Nov. 1996.

[14] L. Xiao-Chun, M. Jun-Fa, and T. Min, “High-speed clock tree simulation method based on moment matching,” *Proc. of Prog. In Electromagnetics Research Symposium (PIERS) 2005*, Hangzhou, China, vol. 1, no. 2, pp. 142-146, 22-26 Aug. 2005.

[15] L. Hungwen, S. Chauchin, and L. J. Chien-Nan, “A tree-topology multiplexer for multiphase clock system,” *IEEE Trans. CAS I: Regular Papers*, vol. 56, no. 1, pp. 124-131, Feb. 2009.

[16] N. Rakuljic and I. Galton, “Tree-structured DEM DACs with arbitrary numbers of levels,” *IEEE Trans. CAS I: Regular Papers*, vol. 52, no. 2, pp. 313-322, Feb. 2010.

[17] B. Ravelo, “Behavioral model of symmetrical multi-level T-tree interconnects,” *Prog. In Electromagnetics Research B*, vol. 41, pp. 23-50, 2012.

[18] B. Ravelo,“Modelling of asymmetrical interconnect T-tree laminated on flexible substrate,” *Eur. Phys. J. Appl. Phys*., vol. 72, no. 2 (20103), pp. 1-9, Nov. 2015.

[19] B. Ravelo and O. Maurice, “Kron-Branin modelling of Y-Y-tree interconnects for the PCB signal integrity analysis,” *IEEE Trans. EMC*, vol. 59, no. 2, pp. 411-419, Apr. 2017.

[20] D. S. Gao, A. T. Yang, and S. M. Kang, “Modeling and simulation of interconnection delays and crosstalks in high-speed integrated circuits,” *IEEE Trans. CAS I*, vol. 37, no. 1, pp. 1-9, Jan. 1990.

[21] M. Voutilainen, M. Rouvala, P. Kotiranta, and T. Rauner, “Multi-gigabit serial link emissions and mobile terminal antenna interference,” *Proc of 13th IEEE Workshop on SPI*, Strasbourg, France, pp. 1-4, May 2009.

B. Ravelo holds his Ph.D. degree in 2008 from Univ. Brest and his HDR in 2012 from Univ. Rouen. He is currently Associate Professor at ESIGELEC/IRSEEM in Rouen (France). His research interests cover the microwave circuit design, EMC, and signal/power integrity (SI/PI) engineering. He is a pioneer of the negative group delay (NGD) concept for RF/analog and digital circuits and systems. He is (co)-author of more than 200 national/international papers. His current publication h-index is 15 (Reference: Google Scholar 2017).

A. Normand is born in Normandy (France), where he is confronted with his first experiment in scientific instrumentation. He joined the laboratory GPM UMR 6634 where he had the opportunity to develop several technical aspects of the tomographic atom probe (SAT). In 2005, he has worked for few months in the Laboratory of Materials Analysis in Göttingen (Germany) to develop a 3D field ion microscope. After receiving master's degree in Scientific Instrumentation from the Univ. Rouen in 2007, he integrated, as an Instrumental Design Engineer, the ERIS Research Team to develop the SAT and its correlative techniques.

F. Vurpillot is currently a Professor at GPM UMR 6634, Univ. Rouen. His research interest is on the SAT scientific instrumentation.

High Isolation UWB-MIMO Compact Micro-strip Antenna

Ze-Lin Song, Zhao-Jun Zhu, and Lu Cao

Institute of Applied Physics
University of Electronic Science and Technology of China, Chengdu, 610054, China
Songzelin0208@126.com, uestc98@163.com, cl_stella@163.com

***Abstract* ─** A compact four-unit ultra-wideband multiple-input multiple-output (UWB-MIMO) antenna with very high isolation, dual polarization, notched structure, and achieving dual-state operation, along with smaller volume, is proposed in this paper. The proposed MIMO antenna element consists of two parts: the front patch composed of four symmetrical trapezoidal radiating elements and feeder, and the back composed of a rectangular annular ground. The offset of antenna operating frequency band is achieved by adjusting the rectangular patch in the middle of the back side, and by introducing an X-shaped metal narrow strip on the top side and an X-shaped slit on the bottom side to improve the isolation in the single port feeding state of antenna. Finally, the dimension of the antenna is $32 \times 32mm^2$. Under the frequency from 3.1 GHz to 10.6 GHz, the isolation in the condition of differential mode can below -30 dB, which is very high, and also can work in the single port inputting state, showing a dual mode operation. In addition, a trapezoidal slit is introduced to obtain a notch structure. The measured results and simulation results are consistent.

***Index Terms* ─** Dual polarization, dual-state operation, micro-strip, notch band, UWB-MIMO antenna.

I. INTRODUCTION

Multi-input multiple-output (MIMO) technology has the advantage of regarding the multi-path radio channel with the transmitter and receiver as a whole to optimize, so as to achieve high communication capacity and spectrum utilization rate. MIMO technology is a kind of near-optimal diversity to the spatial and temporal congregation and technique of interference cancellation, making it receive more and more attention in recent years. The U.S. Federal Communications Commission has released a 3.1-10.6 GHz bandwidth as Ultra-wideband (UWB) in 2002 [1], a new type of wireless Communication technology, which has many advantages including wide bandwidth, high-data-rate wireless transmission, high capacity, and low-power consumption. The combination of UWB technology with MIMO technology, the use of space multipath, parallel transmission of multiple signals, can obtain obvious multiplexing gain and diversity gain, and achieve a stable signal transmission in distance. Isolation is one of the most important performance indicators of MIMO antennas, achieving high isolation and small size is also a challenge. Several UWB-MIMO antennas are reported recently [2-4]. But, especially for the compact UWB antenna, their components is very difficult to reduce, so compared with narrowband antennas' mutual coupling, which is difficult to realize the isolation degree is higher than 20 dB [4].Two differential feed antenna reported recently also has high isolation [5, 6], while they have a common problem, both antennas are only able to operate in differential mode, and cannot work in others condition. The antenna proposed in this paper has two pairs of ports and symmetrical structure, work well with a very high degree of isolation in the differential mode excitation state, but when working in the single port feeding state, it can also work normally, thus making the antenna have a wider range of applications and the volume on the basis of the original reduced very much. Additionally, in order to facilitate the application, attaching the trapezoidal gap to the antenna patch can achieve the notched structure [7-9], can perfectly cover 5.2 and 5.8 GHz WLAN signal. The details of the antenna design and simulation, measurement results are as follows.

II. UWB-MIMO ANTENNA DESIGN

As shown in Fig. 1, the four radiation units of the Antenna-A are placed tightly and symmetrically on the top side of the substrate to reduce the size of antenna. Each radiating element consists of a trapezoidal patch and a feeder of the same size. In the state of differential mode inputting, two pairs of differential ports are orthogonal to each other. In theory, infinite isolation can be achieved under differential input conditions, furthermore dual polarization can be achieved. The back of the substrate consists of a rectangular ring ground and a rectangular patch in the middle, and the four units of the antenna share the rectangular radiation gap on the back, and the central rectangular patch and the four rectangular holes in the middle of the annular ground are used to adjust the left and right offset of the antenna band.

Submitted On: November 1, 2017
Accepted On: January 9, 2018

In order to make the antenna work properly in the single port feeding mode, introduction of the X-shaped metal narrow strip on the top side and the X-shaped slit on the bottom side can improve the isolation in single port feeding state of antenna. The final parameters for antenna are listed in Table 1.

Table 1: Parameter of the Antenna-A

Parameter	L	h	Wf	Lc	Wc
Value (mm)	32	0.508	1	2	3
Parameter	Lf	L1	L2	W1	Li
Value (mm)	2.9	7.7	9.5	2	26.1
Parameter	L2	Wp	Wg		
Value (mm)	9	0.1	0.1		

The total size of the antenna is just $32 \times 32mm^2$, reduced very much compared with others, much smaller than the recent published antennas.

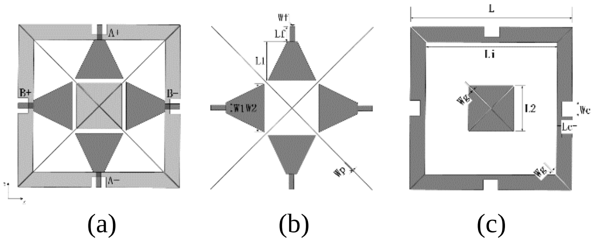

(a) (b) (c)

Fig. 1. Configuration of the proposed Antenna-A: (a) whole geometric structure, (b) the top view, and (c) the bottom view.

For the differential mode, the grounding line is symmetrical along two differential ports. Under differential excitation mode, the Port-A and Port-B of the MIMO antenna are symmetrical along the X-axis and Y-axis. Figure 2 shows the electric field distribution in the low frequency, intermediate frequency and high frequency of the Antenna-A part when only the Port-A of the Antenna-A is differential inputted. It is obvious that the virtual ac of Port-A is distributed along the Y-axis in the entire frequency band, while Port-B is arranged on the virtual ac ground of Port-A. The minimum value of current on virtual communication is zero. Because the Port-B is symmetrical in the same, so the Port-A is situated on the ac ground of the Port-B, so either the Port-A or Port-B is excited, the other has no signal. In this way, the theoretical differential isolation between Port-A and Port-B is not limited.

With reference to the [10], the differential coupling between the two differential Ports A and B can be calculated by:

$$S_{ba} = S_{11} - S_{41} - S_{32} + S_{42}, \tag{1}$$

$$S_{ba} = S_{13} - S_{14} - S_{23} + S_{24}. \tag{2}$$

Since the antenna is symmetrical, then S_{ab} should theoretically equal to S_{ba}. Figure 3 shows the simulated and measured differential coupling between the two adjacent ports of the Antenna-A. Because the result is obtained by calculation, the machining error and measurement environment error are further magnified in the calculation, so the measurement result and the simulation result will produce some error. But the manufactured antennas still achieve a very high differential isolation at up to 30 dB over the entire frequency band.

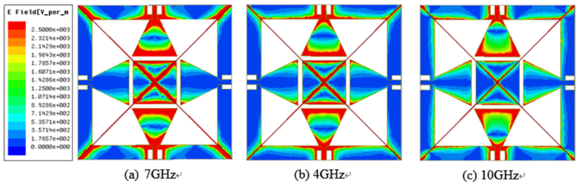

(a) 7GHz (b) 4GHz (c) 10GHz

Fig. 2. The distribution of E-field of Antenna-A at different frequencies with only differential Port-A excited.

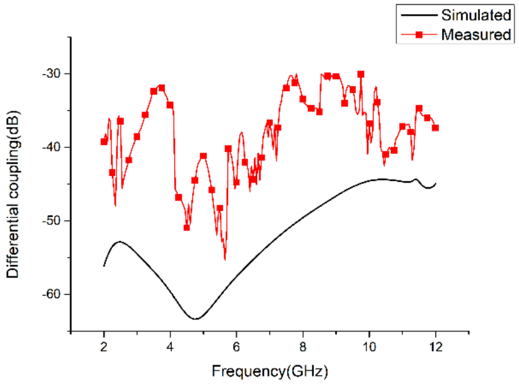

Fig. 3. The simulated and measured differential coupling between Port-A and Port-B.

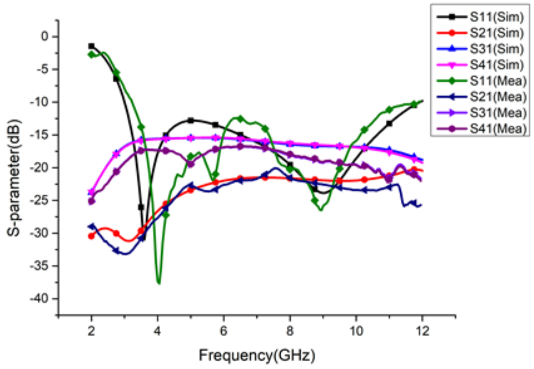

Fig. 4. The Simulated and measured S-parameter of the Antenna-A in the single port feeding state.

Just as mentioned earlier, the isolation of two recently reported differential mode feed antennas is relatively high, but they cannot work well under single port excitation conditions, which will undoubtedly limit the condition of usage, bringing inconvenience to users. The antenna mentioned in this paper not only have an ultra-high isolation of -45 dB below in the differential feeding conditions, but also can work in the single port feeding conditions. The X-shaped metal narrow strip on the top and the X-shaped slit on the bottom are introduced to improve the isolation in single port feeding state enable the antenna to operate normally. The single port feeding state of the antenna is shown in Fig. 4. This greatly facilitate convenience to the customer, and also expand the performance of antenna.

III. NOTCHED STRUCTURE

In order to avoid interfering with the wireless local area network (WLAN) system (5.2 GHz, 5.8 GHz) and facilitate people's using, a half-wavelength slit resonator was introduced, Antenna-B shown in Fig. 5, to achieve a 4.5-6.3 GHz notch structure. The sizes of slits and antennas are shown in Table 2.

Table 2: Parameter of the Antenna-B

Parameter	L	h	Wf	Lc	Wc
Value (mm)	32	0.508	1.3	1.8	2.2
Parameter	Lf	L1	L2	W1	Li
Value (mm)	2.8	8	9.8	1.5	27
Parameter	L2	Wp	Wg	Ls1	S
Value (mm)	9.8	0.1	0.1	4.5	0.1
Parameter	W2	Ws1	hs	Ws2	
Value (mm)	8.1	2.34	2	5.2	

At 5.2 GHz and 5.8 GHz, the current mainly flows along the half-wavelength slit etched in the trapezoidal patch which leads to the impedance matching of the antenna being deteriorating seriously. Consequently, the antenna hardly radiates at these frequencies, the band-notched characteristic is obtained.

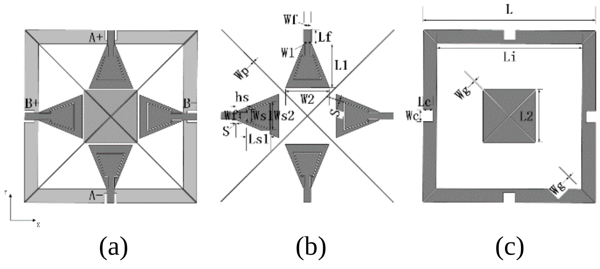

(a) (b) (c)

Fig. 5. Configuration of the proposed Antenna-B: (a) whole geometric structure, (b) the top view, and (c) the bottom view.

IV. RESULT AND DISCUSSION

As shown in Fig. 6, the proposed Antenna-A and Antenna-B are made of a substrate with relative permittivity of 2.2 and thickness of 0.508 mm. Especially, the proposed antenna is much smaller than the previously reported UWB antennas. The comparison is presented in Table 3.

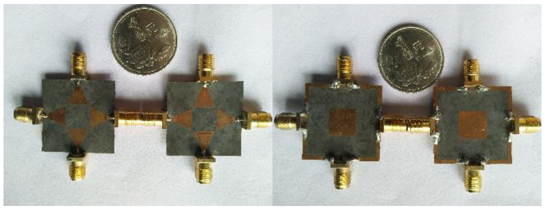

Fig. 6. Photograph of the fabricated Antenna-A and Antenna-B.

Table 3: Comparison of the related UWB-MIMO antennas

Antenna	Measured Isolation (dB)	Notched Bands (GHz)	Electrical Size ($\lambda_g * \lambda_g$)
[2]	-15	No	1.87*1.87
[3]	-15	5.5	2.06*2.06
[5]	-35	5.8/7.4	1.03*1.03
[6]	-13	5.2/5.8	0.43*0.43
This work	-30	5.2/5.8	0.47*0.47

Referring to [10], the odd mode reflection coefficient can be calculated by:

$$S_{dd} = (S_{11} - S_{12} + S_{22} - S_{21})/2. \tag{3}$$

Figure 7 is the odd mode reflection coefficient of the simulation and measurement of the two antennas. We can clearly see that the simulation results of Antenna-A and Antenna-B are both below -10 dB in the 3.1GHz-10.6 GHz, which can perfectly cover the ultra-broadband frequency band, as well as Antenna-B notch-band (4.5– 6.3 GHz) and with a measured -10 dB impedance bandwidth from 3.6 to 10.6 GHz, as well as notch-band (4.9–6.2 GHz); although the measured results and simulated results have some errors, but based on processing and environment of measurement impact, these errors within the acceptable range. In general, the measurement results and simulation results are consistent.

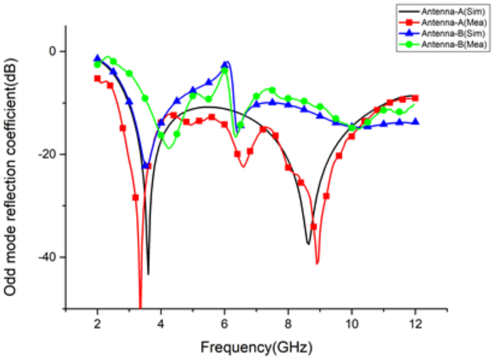

Fig. 7. Simulated and measured odd mode reflection coefficients of Antenna-A and Antenna-B.

The radiation patterns of Antenna-B at 4 GHz, 7 GHz and 10 GHz is shown in Fig. 8. It can be seen that the proposed Antenna-B represents an omnidirectional radiation pattern in the H-plane, and the radiation pattern maintains the shape of the E-plane shown in Fig. 7 in the whole frequency band. Because of the normalized cross-polarization components in H-plane and E-plane simulations are all lower than -40 dB, the normalized cross-polarization components in H-plane and E-plane simulations are all lower than -40 dB.

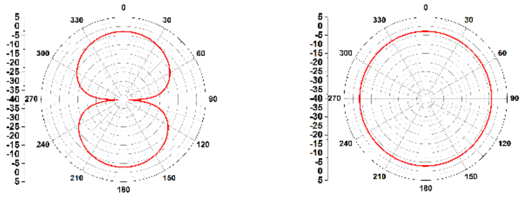

E-plane at 4 GHz H-plane at 4 GHz

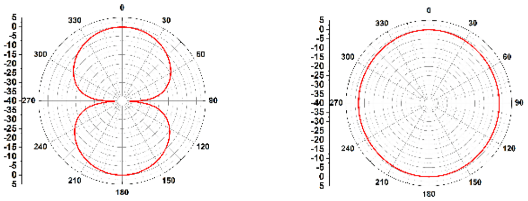

E-plane at 7 GHz H-plane at 7 GHz

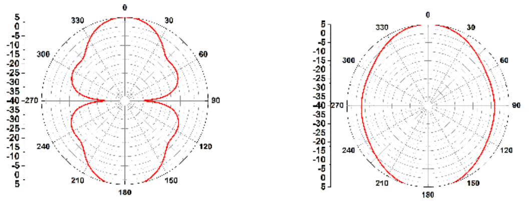

E-plane at 10 GHz H-plane at 10 GHz

Fig. 8. Normalized radiation patterns of the proposed Antenna-B when Port-A is excited and Port-B is terminated with 50Ω load.

The Envelope correlation coefficient (ECC) is an important parameter to measure the performance of MIMO system, which can be calculated using the radiation pattern [11] or the S-parameter. Now, we use the S parameter to calculate the ECC by:

$$ECC = \frac{\left|S_{11}^{*}S_{12}+S_{21}^{*}S_{22}\right|^{2}}{\left(1-\left|S_{11}\right|^{2}-\left|S_{21}\right|^{2}\right)\left(1-\left|S_{22}\right|^{2}-\left|S_{12}\right|^{2}\right)}. \quad (4)$$

In real life, the mobile system requirements for the ECC is less than 0.5. As can be seen from Fig. 9, since the degree of isolation between the adjacent differential ports is very high, we can calculate the ECC of the MIMO Antenna-B is less than 0.0001 in non-notch band, For the mobile system, the antenna is proposed in this paper is excellent.

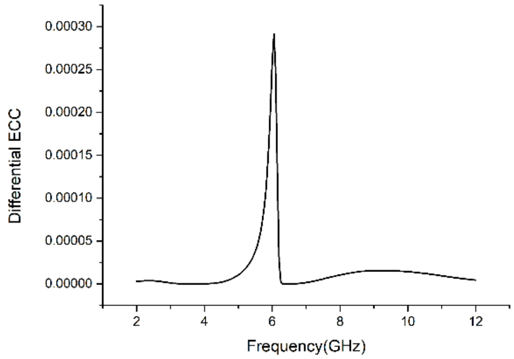

Fig. 9. Calculated ECC of the proposed Antenna-B.

V. CONCLUSION

This paper introduces a compact four-unit UWB-MIMO antenna that enables dual-state operation and is much smaller. Dual orthogonal polarization and pretty high differential isolation can be obtained by arranging two pairs of differential ports in the virtual ac ground lines of each other. An X-shaped metal narrow strip on the top side and an X-shaped slit on the bottom side were introduced to improve the isolation in the single port feeding state of antenna. To realize notch-band characteristic, the half-wavelength slits were introduced. The measurement results and simulation results are consistent, so we can conclude that the proposed antenna is suitable for UWB communication systems.

ACKNOWLEDGEMENT

This work is supported by "National Natural Science Foundation of China (Grant No. 61101042)".

REFERENCES

[1] Federal Communications Commission, "First report and order in the matter of revision of part 15 of the commission's rules regarding ultra-wideband transmission systems," ET-Docket 98-153, Apr. 22, 2002.

[2] E. A. Daviu, M. Gallo, B. B. Clemente, and M. F. Bataller, "Ultra-wideband slot ring antenna for diversity applications," *Electron Lett.*, vol. 46, pp. 478-480, 2010.

[3] P. Gao, S. He, X. B. Wei, Z. Q. Xu, N. Wang, and Y. Zheng, "Compact printed UWB diversity slot antenna with 5.5-GHz band-notched characteristics," *IEEE Antennas Wireless Propag. Lett.*, vol. 13, pp. 237-240, 2014.

[4] J. F. Li, Q. X. Chu, Z. H. Li, and X. X. Xia, "Compact dual bandnotched UWB MIMO antenna with high isolation," *IEEE Trans. Antennas Propag.*, vol. 61, pp. 4759-4766, 2013.

[5] W. A. Li, Z. H. Tu, and Q. X. Chu, "Compact, high isolation and dual-polarized differential dual-

[6] notched UWB-MIMO slot antenna," *IEEE Microw. Opt. Technol. Lett*., vol. 57, no. 11, pp. 2609-2614, Nov. 2015.

[7] Y. Y. Liu and Z. H. Tu, "Compact differential band-notched stepped-slot UWB-MIMO antenna with common-mode suppression," *[J]. IEEE Antennas & Wireless Propagation Letters*, 16 (99):1-1, 2017.

[8] J. R. Kelly, P. S. Hall, and P. Gardner, "Band-notched UWB antenna incorporating a microstrip open-loop resonator," *IEEE Trans. Antennas Propag*., vol. 59, no. 8, pp. 3045-3048, Aug. 2011.

[9] Y. Sung, "Triple band-notched UWB planar monopole antenna using a modified H-Shaped resonator," *IEEE Trans. Antennas Propag*., vol. 61, no. 2, pp. 953-957, Feb. 2013.

[10] T. G. Ma and J. W. Tsai, "Band-rejected ultra-wideband planar monopole antenna with high frequency selectivity and controllable bandwidth using inductively coupled resonator pairs," *IEEE Trans. Antennas Propa*g., vol. 58, no. 8, pp. 2747-2752, Aug. 2010.

[11] Q. Xue, S. W. Liao, and J. H. Xu, "A differentially-driven dual-polarized magneto-electric dipole antenna," *IEEE Trans. Antennas Propag*., vol. 61, pp. 425-430, 2013.

[12] R. G. Vaughan and J. B. Andersen, "Antenna diversity in mobile communications," *IEEE Trans. Veh. Technol*., vol. 36, pp. 149-172, 1987.

Zelin Song was born in Tianjin city, China, in 1991. He received the B.S. degree in Physics from the UESTC in 2015, and is working toward the M.D. degree in the UESTC. He research interests include the design of microwave and millimeter-wave circuits.

Zhaojun Zhu was born in Sichuan, China, in 1978. He received the B.S. degree and the Ph.D. degree in Physical Electronics in UESTC, Chengdu, in 2002 and 2007 respectively. Since 2012, he has been an Associate Professor with the UESTC. His research interests include the design of microwave and millimeter-wave circuits.

Lu Cao was born in Jiangxi Province, China, in 1993. She received the B.S. degree in Physics from Gannan Normal University, in 2015, and is currently working toward the M.D. degree in UESTC. Her research interests include the design of microwave and millimeter-wave circuits.

Performance of Multiple-Feed Metasurface Antennas with Different Numbers of Patch Cells and Different Substrate Thicknesses

Niamat Hussain and Ikmo Park

Department of Electrical and Computer Engineering
Ajou University, Suwon 16499, Republic of Korea
ipark@ajou.ac.kr

Abstract ─ The design and performance of low-profile, multiple-feed metasurface antennas with different numbers of patch cells and different substrate thicknesses at a terahertz frequency are presented in this paper. The utilized antenna designs consist of a periodic array ($N \times M$) metallic square-patch metasurface and a planar feeding structure, which are both patterned on an electrically thin, high-permittivity GaAs substrate. The antenna gain increased in a linear fashion with an increasing number of patch cells, which were directly fed by the slit feedline. A 3-dB gain increment was observed irrespective of the substrate thickness when the number of patch cells was doubled. However, the 3-dB gain bandwidth as well as the radiation efficiency changed significantly with varying substrate thicknesses. The described antenna structure offers useful characteristics by means of a combination of different substrate thicknesses and patch numbers. In addition, the proposed antenna design features a number of benefits, including a low profile, mechanical robustness, easy integration into circuit boards, and excellent suitability for low-cost mass production.

Index Terms ─ Antenna array, metamaterials, metasurface, terahertz antennas, wide gain bandwidth.

I. INTRODUCTION

In recent years, metasurfaces have facilitated new approaches for manipulating the wavefronts of electromagnetic waves [1]. A metasurface is a two-dimensional structure that is composed of a periodic array of small scattering elements whose dimensions and periods are small when compared with the operating wavelength [2]. Due to their succinct planar structure, easy fabrication, and low cost, metasurfaces are widely used in the design of planar antennas. The main benefits of metasurface antennas are their ability to provide enhanced performance in terms of gain, radiation pattern, and bandwidth with an ultra-low profile design [3], [4]. The extraordinary properties of such antennas, which render them suitable for the application at hand, from the microwave to the terahertz band, have previously been presented [5]–[15].

In particular, researchers have focused on terahertz (THz) metasurface antennas, since the THz band has exhibited significant potential in relation to emerging applications in the fields of imaging, sensing, and astronomy, as well as defense and security [16]. This band offers many additional advantages, including an extremely high data transmission rate, wide bandwidth, high resolution, and improved spatial directivity with system compactness in wireless communication systems. Recently, a wide-gain-bandwidth metasurface antenna fed by a single open-ended, leaky-wave slit at terahertz frequencies was reported [17]. However, the higher atmospheric losses and attenuation of the THz band may restrict its usage due to its low gain. Therefore, low-profile antennas featuring high gain characteristics are highly recommended for terahertz applications.

Typically, planar antennas are coupled with lenses in order to realize high gain and wide bandwidth characteristics in the THz frequency range. Yet, lens-coupled antennas have a number of limitations, including their bulky size and low radiation efficiency [18]. Fabry-Perot antennas are designed to obtain a high gain, although such antennas face the design challenges associated with a low 3-dB gain bandwidth, especially when coupled with high-permittivity substrates [19]–[21]. THz antennas fed by slot waveguides also present high gain properties due to their low feeding losses. However, the manufacturing cost of such antennas is generally very high, since they usually consist of a complicated three-dimensional structure built with metallic walls [22], [23].

In this paper, we present the design of planar, low-profile, multiple-feed metasurface antennas with different numbers of patch cells and different substrate thicknesses in the THz frequency band in order to obtain high gain characteristics.

The remainder of this paper is organized as follows. Section II describes the geometry of the proposed antennas. Section III characterizes the detailed simulation setup as well as the conditions adopted during the numerical analysis of the antennas. Section IV presents

Submitted On: July 21, 2017
Accepted On: January 1, 2018

the antenna characteristics for different numbers of patch cells at different substrate thickness values. Finally, our conclusions are drawn in Section V.

II. SIMULATION SETUP

The majority of antenna analysis techniques can be categorized into two methods, namely a full-wave analysis method and an approximation method based on simplifying assumptions. The term “full-wave” generally refers to electromagnetic solutions that include all the applicable wave mechanisms. Such solutions allow for the implications of the boundary conditions to an accuracy limit, while the approximation methods do not enforce boundary conditions and thus do not consider surface wave effects, mutual coupling, or perhaps even radiation. Different analysis techniques and their respective limitations in terms of analyzing metasurfaces have previously been presented [24]. For high-frequency electromagnetic applications, full-wave time-domain simulation methods are highly desirable, especially when broadband results are required [25].

In our simulations, the full three-dimensional structures of the antennas were modeled, while the characteristics were investigated using the finite-integration time-domain commercial simulator CST Microwave Studio [26]. The antennas were excited by means of a discrete port located at the gap in the short dipole, which results in a default Gaussian-shaped excitation signal being passed into the gap in the slit line at its center. This setup guarantees the stability of the simulation regardless of the simulation time. A transient time-domain solver with a hexahedral mesh type was selected, while the accuracy level was set at -40 dB. This solver allows the complete characterization of the performance of antennas at multiple frequencies during one simulation run. The simulation time is inversely proportional to the size of the smallest mesh cell, which needs to be sufficiently fine to capture all the detail of the unit cell of the metasurface. In the simulation setup, the maximum mesh size was set at approximately 2.5 µm, which is one-twentieth of a free space wavelength at 0.3 THz. CST simulates each port independently, which means that the simulation time for each antenna is linearly proportional to its number of ports. Far-field monitors were set up for frequencies ranging from 0.3 THz to 0.42 THz. Moreover, open boundaries with some added space ($\lambda_o/4$) were used for the accurate calculation of the far-field results. The number of mesh cells in the computational domain for the antenna at $H = 40$ µm with a patch number of 5 × 5 was approximately 1.53×10^6, occupying 1.0 GB of memory. It took about 50 minutes when using 20 threads of parallelization in the Xeon E5-2660-V2 server with a clock speed of 2.2 GHz.

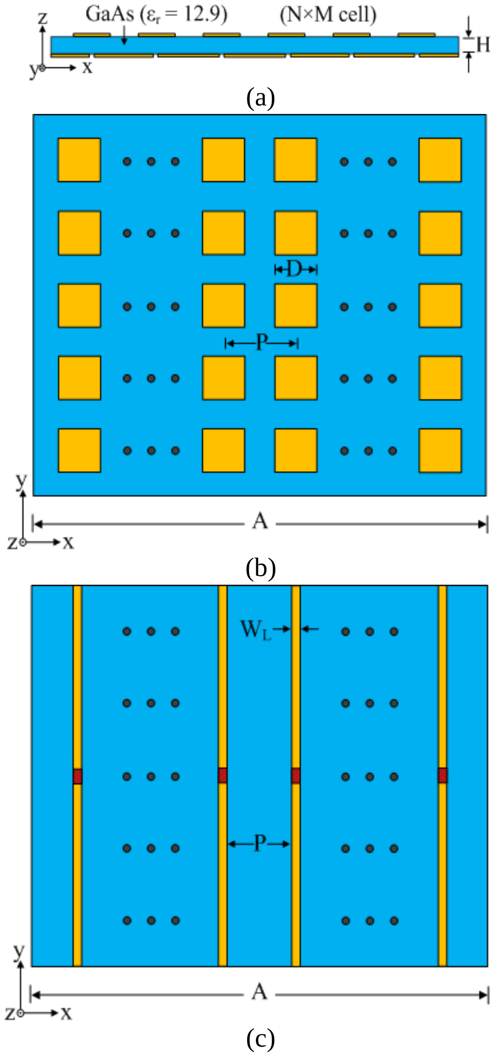

Fig. 1. Antenna geometry: (a) side view, (b) front view of top surface, and (c) front view of bottom surface.

Table 1: Common antenna design parameters

Parameter	Dimension (µm)
A	$5 \times P + D/2$
W_L	15
L_D	10
g	10

Table 2: Design parameters for different substrate thickness (H) values

Substrate Thickness (*H*)	Periodicity *(P)*	Patch Length *(D)*
80 µm	330 µm	195 µm
40 µm	340 µm	200 µm
20 µm	360 µm	210 µm

III. ANTENNA GEOMETRY

The geometry of the proposed metasurface antenna with a multiple-feeding structure is shown in Fig. 1. The antenna was patterned on both sides of a GaAs substrate with a dielectric constant of $\varepsilon_r = 12.9$ and a loss tangent of $\tan\delta = 0.006$. The metasurface, which comprised an array of periodic $M \times N$ symmetrical metallic square patches, was patterned on the upper side of the substrate. The number of patches along the vertical axis (*y*-axis) was designated as *M*, while *N* represents the patches along the horizontal axis (*x*-axis). The periodicity and patch length of the square patch array were defined as *P* and *D*, respectively. The feeding structure, which comprised an array of open-ended, leaky-wave slits with a width of W_L, was etched on the lower side of the substrate. The number of feeding slits was equal to *M*, while the distance between the slits was *P*, which is equal to the periodicity *(P)* of the patch array. The chosen structure ensures the excitation of every patch column of the metasurface. The thickness and conductivity of the metal layer used in the ground plane and the patches were 0.35 μm and 1.6×10^7 S/m, respectively. The overall dimensions of the antenna were $A \times A \times H$ μm^3. Each feeding slit was fed by a short dipole at its center, which had a gap and a width of *g* and L_D, respectively. A discrete port was placed at the center of the feed gap of each slit in order to excite the antenna. The antenna was optimized at each substrate thickness value ($H = 20$ μm, $H = 40$ μm, and $H = 80$ μm) for different numbers of patch cells ($M \times N$) by changing only the periodicity and the patch size. The design parameters of the antennas that result in the optimum broadside gain and 3-dB gain bandwidth are summarized in Tables 1 and 2. The designed antenna can be realized by feeding it with a femtosecond laser pump. The laser pulses could be simultaneously focused on the short dipole gap of each slit of the antenna so as to achieve the advantages of a low profile, high gain, and wide bandwidth characteristics.

IV. ANTENNA CHARACTERISTICS

Figure 2 shows the performance of the multiple-feed metasurface antennas in terms of the boresight gain for different numbers of patch cells and various substrate thickness values. We fixed the number of patch cells along the vertical axis because the leaky-wave slit can effectively excite up to five patch cells. Increasing the number of patch cells in the vertical direction had no significant effect on the enhancement of antenna gain [27]. Thus, we fixed the number of patch cells in the vertical direction and only increased the number of patch cells in the horizontal direction. When the number of patch cells was increased from 5 × 3 to 5 × 6 to 5 × 12 for different substrate thickness values ($H = 20$ μm, $H = 40$ μm, and $H = 80$ μm), the antenna gain increased in a linear fashion. The gain increased in 3-dB increments regardless of the substrate thickness when the total number of patches was increased twice. The gain observed for 5 × 3 patch cells at $H = 20$ μm was 12.5 dBi, which increased to 15.5 dBi and 18.5 dBi when the number of patch cells was increased to 5 × 6 and 5 × 12, respectively. Similarly, at substrate thicknesses of $H = 40$ μm and $H = 80$ μm, the antenna gain increased from 13.5 to 19.5 dBi in a 3-dB increment when the number of patch cells increased from 5 × 3 to 5 × 6 and 5 × 12, respectively. These results showed that a peak gain occurs for each substrate thickness value, while the antenna gain increases with an increasing number of patch cells. Moreover, the central frequency shifted downwards for thicker substrates due to the increase in the effective dielectric constant. It was approximately 0.385 THz at $H = 20$ μm, although it shifted to 0.375 and 0.33 THz for $H = 40$ μm and $H = 80$ μm, respectively. It was interesting to observe that the 3-dB gain bandwidth and central frequency changed significantly with varying substrate thicknesses, whereas the patch number had a negligible influence on both. The 3-dB gain bandwidth was low, being approximately 8% and 10% for $H = 20$ μm and $H = 80$ μm, respectively, although it was wide, being almost 17.3% for $H = 40$ μm regardless of the patch number. In fact, the antennas with thick substrates faced the design challenges associated with a low 3-dB gain bandwidth at terahertz frequencies due to the substrate resonance. This problem can be solved by reducing the substrate thickness to $\lambda_o/20$, where $\lambda_{o,}$ is the free-space wavelength [28]. A substrate thickness of 40 μm is approximately $\lambda_o/20$ with respect to its central operating frequency. Hence, it exhibited the wide gain bandwidth.

Figure 3 presents the radiation efficiency of the multiple-feed metasurface antennas with different numbers of patch cells at various substrate thickness values. The radiation efficiency increased with an increasing substrate thickness, although it was not affected by different patch numbers (5 × 3, 5 × 6, and 5×12), especially within the 3-dB gain bandwidth. The radiation efficiency calculated for $H = 20$ μm was 57%, which increased to 73% and 85% for $H = 40$ μm and $H = 80$ μm, respectively. It was observed that the number of patch cells only influenced the gain enhancement, without significantly changing the other antenna characteristics, whereas the substrate thickness determined both the 3-dB gain bandwidth and the radiation efficiency. This therefore provides a simple method for determining the specific antenna characteristics in terms of both gain and bandwidth by choosing a specific combination of patch number ($M \times N$) and substrate thickness.

The radiation patterns of the metasurface antennas with different substrate thicknesses and different patch numbers were plotted at their central frequencies as shown in Figs. 4–6. All the antennas exhibited directive radiation patterns with low sidelobe and backlobe levels in both the *xz*- and *yz*-planes. Generally, the *yz*-plane showed clean profile patterns with lower sidelobe levels when compared to the *xz*-plane. Furthermore, the number of sidelobe levels in the *xz*-plane increased with an increasing number of patch cells. The antennas yielded low back radiation throughout the entire gain bandwidth due to the successful implementation of the metasurface, even though the leaky-wave slit is open to free space. However, the gain value associated with both back radiations increased with an increase in the number of patch cells. Interestingly, the back radiation decreased when the substrate thickness increased.

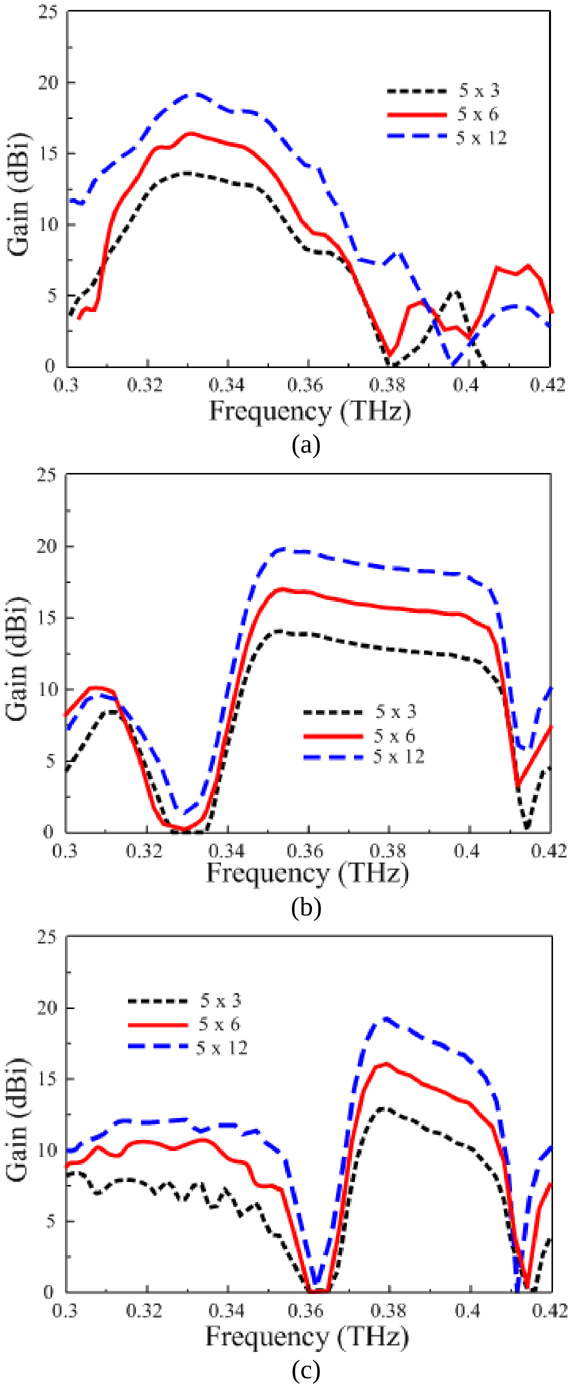

(a)

(b)

(c)

Fig. 2. Antenna gain with different numbers of patch cells and different substrate thicknesses: (a) H = 80 μm, (b) H = 40 μm, and (c) H = 20 μm.

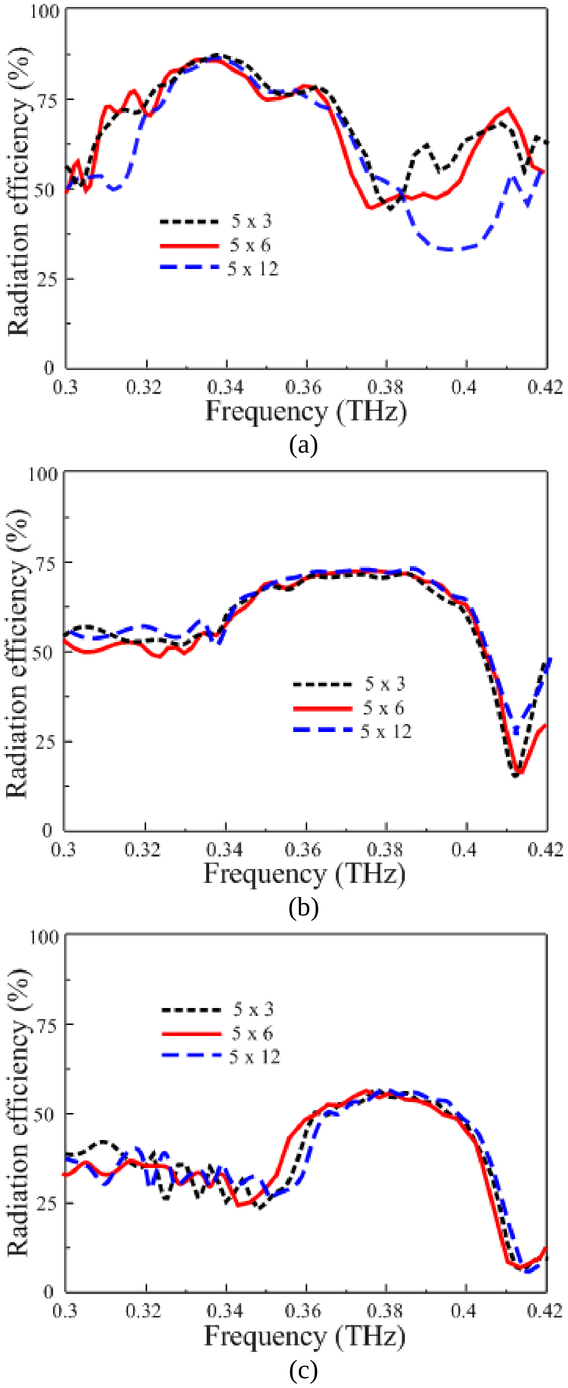

(a)

(b)

(c)

Fig. 3. Antenna radiation efficiency with different numbers of patch cells and different substrate thicknesses: (a) H = 80 μm, (b) H = 40 μm, and (c) H = 20 μm.

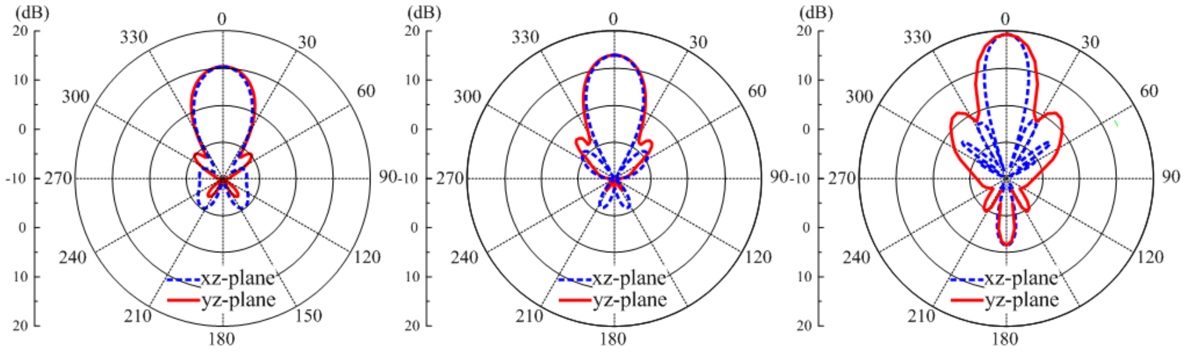

(a) (b) (c)

Fig. 4. Antenna radiation patterns for different numbers of patch cells at H = 80 μm: (a) 5×3, (b) 5×6, and (c) 5×12.

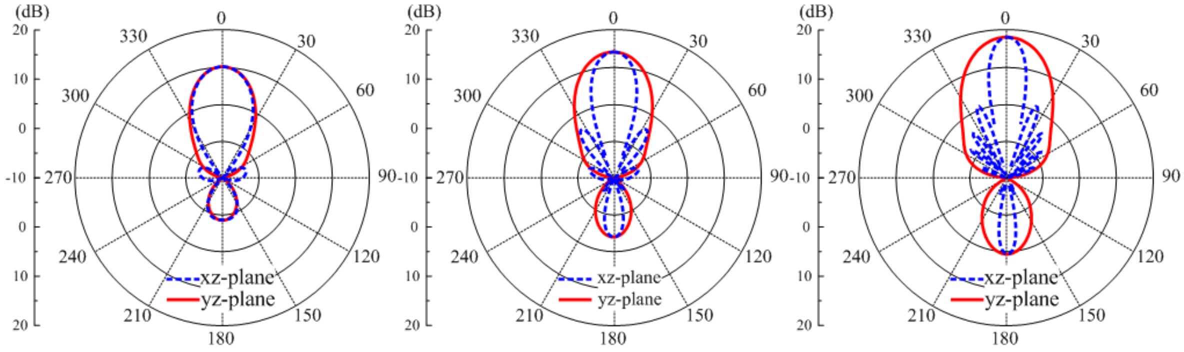

(a) (b) (c)

Fig. 5. Antenna radiation patterns for different numbers of patch cells at H = 40 μm: (a) 5×3, (b) 5×6, and (c) 5×12.

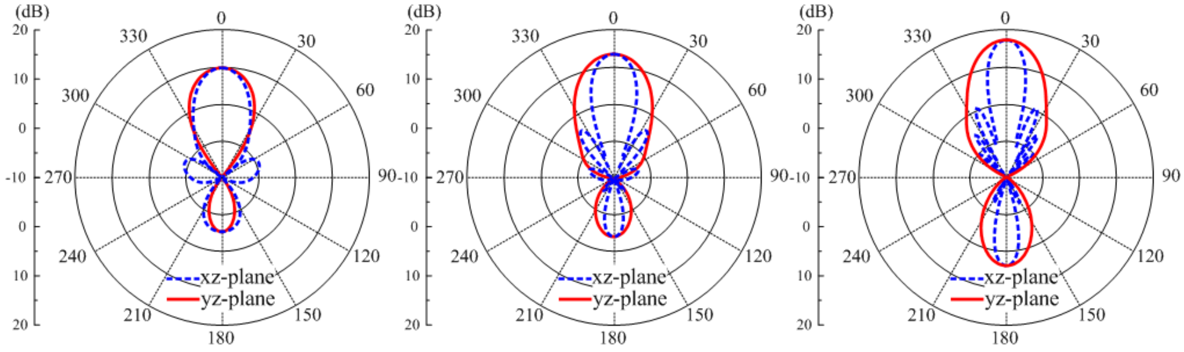

(a) (b) (c)

Fig. 6. Antenna radiation patterns for different numbers of patch cells at H = 20 μm: (a) 5×3, (b) 5×6, and (c) 5×12.

V. CONCLUSION

The design of multiple-feed metasurface antennas with different numbers of patch cells and different substrate thicknesses, as well as the associated radiation characteristics, were studied over the THz frequency band. The antennas were composed of a patch array and multiple feeding structures, both of which were patterned on a high-permittivity, electrically thin GaAs substrate. Regardless of the substrate thickness, the antenna gain increased linearly in increments of 3 dB when the number of patches was increased twice. The radiation efficiency and 3-dB gain bandwidth were mainly determined by the substrate thickness. The 3-dB gain bandwidth was 7%, 17.3%, and 10% for the substrate thicknesses of H = 20 μm, H = 40 μm, and H = 80 μm, respectively. The radiation efficiency increased with increasing substrate thickness. The efficiency was calculated as 57% at H = 20 μm, and it increased to 73% for H = 40 μm and

85% for $H = 80$ µm. The different combinations of patch numbers and substrate thicknesses provide freedom in terms of choosing the desired gain values and 3-dB gain bandwidth for various antenna applications, which increases their value for THz applications. Furthermore, these antennas offer a number of other promising features, including a low profile, mechanical robustness, suitability for low-cost mass production, and easy integration into circuit boards.

ACKNOWLEDGMENTS

This work was supported in part by Institute for Information & Communications Technology Promotion (IITP) grant funded by the Korea government (MSIP) (No. 2017-0-00959, University ICT Basic Research Lab), in part by "Human Resources Program in Energy Technology" of the Korea Institute of Energy Technology Evaluation and Planning (KETEP), granted financial resource from the Ministry of Trade, Industry & Energy, Republic of Korea (No. 20164030201380), and in part by the National Research Foundation of Korea (NRF) grant funded by the Korea government (MEST) (2016R1A2B100932).

REFERENCES

[1] N. Yu and F. Capasso, "Flat optics with designer metasurfaces," *Nat. Mater.*, vol. 13, no. 2, pp. 139-150, 2014.

[2] J. P. Turpin, J. A. Bossard, K. L. Morgan, D. H. Werner, and P. L. Werner, "Reconfigurable and tunable metamaterials: A review of the theory and applications," *Int. J. Antennas Propag.*, vol. 2014, 429837, pp. 1-18, 2014.

[3] Y. Dong and T. Itoh, "Metamaterial-based antennas," *Proc. IEEE*, vol. 100, no. 7, pp. 2271-2285, 2012.

[4] C. L. Holloway, E. F. Kuester, J. A. Gordon, J. O'Hara, J. Booth, and D. R. Smith, "An overview of the theory and applications of metasurfaces: The two-dimensional equivalents of metamaterials," *IEEE Antennas Propag. Mag.*, vol. 54, no. 2, pp. 10-35, 2012.

[5] M. Koutsoupidou, I. S. Karanasiou, and N. Uzunoglu, "Rectangular patch antenna on split-ring resonators substrate for THz brain imaging: Modeling and testing," *IEEE Int. Conf. on Bio-informatics and Bioengineering*, Chania, Greece, pp. 1-4, Nov. 2013.

[6] M. E. Badawe, T. S. Almoneef, and O. M. Ramahi, "A true metasurface antenna," *Sci. Rep.*, vol. 6, 19268, pp. 1-8, 2016.

[7] H. Zhou, J. Dong, S. Yan, Y. Zhou, and X. Zhang, "Generation of terahertz vortices using metasurface with circular slits," *IEEE Photon. J.*, vol. 6, no. 6, 5900107, pp. 1-7, 2014.

[8] Q. Zhang, L. Si, Y. Huang, X. Lv, and W. Zhu, "Low-index-metamaterial for gain enhancement of planar terahertz antenna," *AIP Adv.*, vol. 4, no. 3, 037103, pp. 1-7, 2014.

[9] Y. Huang, L. Yang, J. Li, Y. Wang, and G. Wen, "Polarization conversing of metasurface for the application of wide band low-profile circular polarization slot antenna," *Appl. Phy. Lett.*, vol. 109, 054101, pp. 1-5, 2016.

[10] N. Nasimuddin, Z. N. Chen, and X. Qing, "Bandwidth enhancement of a single-feed circularly polarized antenna using a metasurface: Metamaterial-based wideband CP rectangular microstrip antenna," *IEEE Antennas Propag. Mag.*, vol. 58, no. 2, pp. 39-46, 2016.

[11] X. Gao, X. Han, W. P. Cao, H. F. Ma, H. O. Li, and T. J. Cui, "Ultrawideband and high-efficiency linear polarization converter based on double v-shaped metasurface," *IEEE Trans. Antennas Propag.*, vol. 63, no. 8, pp. 3522-3530, 2015.

[12] A. Mahmood, G. O. Yetkin, and C. Sabah, "Wide-band negative permittivity and double negative fishnet-mushroom-like metamaterial in x-band waveguide," *Int. J. Antennas Propag.*, vol. 2017, 2439518, pp. 1-7, 2017.

[13] S. I. Rosaline and S. Raghavan, "Metamaterial inspired square ring monopole antenna for WLAN applications," *ACES Express J.*, vol. 1, no. 1, pp. 32-35, 2016.

[14] A. Shater and D. Zarifi, "Radar cross section reduction of microstrip antenna using dual-band metamaterial absorber," *ACES J.*, vol. 32, no. 2, pp. 135-140, 2017.

[15] P. Rocca and A. F. Morabito, "Optimal synthesis of reconfigurable planar arrays with simplified architectures for monopulse radar applications," *IEEE Trans. Antennas Propag.*, vol. 63, no. 3, pp. 1048-1058, 2015.

[16] P. H. Siegel, "Terahertz technology," *IEEE Trans. Microw. Theory Tech.*, vol. 50, no. 3, pp. 910-928, 2002.

[17] N. Hussain and I. Park, "Terahertz planar wide-gain-bandwidth metasurface antenna," *Int. Workshop on Metamaterials-by-Design*, Riva del Garda, Italy, pp. 1-2, Dec. 2016.

[18] N. Hussain, T. K. Nguyen, H. Han, and I. Park, "Minimum lens size supporting the leaky-wave nature of slit dipole antenna at terahertz frequency," *Int. J. Antennas Propag.*, vol. 2016, 5826957, pp. 1-8, 2016.

[19] N. Hussain, K. E. Kam, and I. Park, "Performance of a planar leaky-wave slit antenna for different values of substrate thickness," *J. Electromagn. Eng. Sci.*, vol. 17, no. 4, pp. 202-207, Oct. 2017.

[20] T. K. Nguyen, B. Q. Ta, and I. Park, "Design of a planar, high-gain, substrate-integrated Fabry-Perot cavity antenna at terahertz frequency," *Curr. Appl. Phys.*, vol. 15, no. 9, pp. 1047-1053, 2015.

[21] N. Hussain, T. K. Nguyen, and I. Park, "Performance comparison of a planar substrate-integrated Fabry-Perot cavity antenna with different unit cells at terahertz frequency," in *IEEE European Conf. on Antennas and Propagation*, Davos, Switzerland, pp. 1-4, Apr. 2016.

[22] K. M. Luk, S. F. Zhou, Y. J. Li, F. Wu, K. B. Ng, C. H. Chan, and S. W. Pang, "A microfabricated low-profile wideband antenna array for terahertz communications," *Sci. Rep*., vol. 7, 1268, pp. 1-11, 2017.

[23] C. Gu, S. Gao, and B. Sanz-Izquierdo, "Low-cost wideband low-THz antennas for wireless communications and sensing," in *UK-Europe-China Workshop on Millimetre Waves and Terahertz Technologies*, Liverpool, UK, pp. 1-4, Sep. 2017.

[24] F. Costa, A. Monorchio, and G. Manara, "An overview of equivalent circuit modeling techniques of frequency selective surfaces and metasurfaces," *ACES J*., vol. 29, no. 12, pp. 960-976, Dec. 2014.

[25] A. Taflove and S. C. Hagness, *Computational Electromagnetics: The Finite-Difference Time-Domain (FDTD) Method*. Artech House, 3rd ed., 2005.

[26] CST Microwave Studio, https://www.cst.com/

[27] N. Hussain and I. Park, "Design of a wide-gain-bandwidth metasurface antenna at terahertz frequency," *AIP Adv*., vol. 7, no. 5, 055313, pp. 1-8, 2017.

[28] B. A. Munk, *Frequency Selective Surfaces: Theory and Design*. Wiley, New York, 2000.

Niamat Hussain received his B.S. degree in Electronics Engineering from Dawood University of Engineering and Technology, Karachi, Pakistan, in 2014. He is currently studying for his M.S. degree at the Department of Electrical and Computer Engineering at Ajou University, Suwon, Republic of Korea. His research is mainly focused on lens-coupled antennas, metasurface antennas, and terahertz antennas.

Ikmo Park received his B.S. degree in Electrical Engineering from the State University of New York at Stony Brook and his M.S. and Ph.D. degrees in Electrical Engineering from the University of Illinois at Urbana-Champaign. He joined the Department of Electrical and Computer Engineering at Ajou University in 1996. Prior to joining Ajou University, he was with the Device and Materials Laboratory, LG Corporate Institute of Technology, Seoul, Republic of Korea, where he was engaged in research and development of various antennas for personal communication systems, wireless local area networks, and direct broadcasting systems. He has authored and co-authored over 300 technical journal and conference papers. He also holds over 30 patents. His current research interests include the design and analysis of microwave, millimeter-wave, terahertz wave, and nano-structured antennas.

A Low Mutual Coupling MIMO Antenna Using Periodic Multi-Layered Electromagnetic Band Gap Structures

Tao Jiang [1], **Tianqi Jiao** [1], **Yingsong Li** [1,2,*]

[1] College of Information and Communications Engineering
Harbin Engineering University, Harbin 150001, China

[2] National Space Science Center, Chinese Academy of Sciences, Beijing 100190, China
*liyingsong@ieee.org,

Abstract **—** A multi-layered electromagnetic band gap (EBG) structure is proposed and incorporated into a MIMO antenna to reduce unexpected mutual coupling between antenna elements. The proposed multi-layered EBG (ML-EBG) structure is comprised of an improved EBG and three loading patches with a same distance. The proposed ML-EBG structure is designed at 2.55 GHz and it is utilized in a MIMO antenna array with an edge-to-edge distance of 0.13λ to reduce the mutual couplings. The simulated and measured results have been put forward to prove that the mutual coupling has been reduced by 30 dB between the antenna elements compared to the MIMO antenna without the ML-EBG structure.

Index Terms **—** MIMO antenna, multi-layered electromagnetic band gap, mutual coupling reduction.

I. INTRODUTION

Mictrostrip antennas have been becoming an useful technology and a hot topic in wireless communication systems in the past decades [1-4] since they are small, light and low profile. Moreover, the microstrip antennas are easy to incorporate into a practical application to form a conformal antenna and they can be implemented to create multi-band antenna and circular polarization antennas [5-8]. In particular, the microstrip antennas are easy to integrate into a unified component with active devices and microwave circuits [9-10], rendering them suitable for various wireless communication applications.

With the development of the wireless communication techniques, MIMO techniques have been attracting much more attention for next-generation applications [11-12]. MIMO antennas are to use in the future portable devices. Since the space of the portable device is limited, the configuration of the multiple antennas is difficult [13-14] to install in such a limited device. As a MIMO antenna aimed to use in wireless portable terminal, the distances between the antenna elements are narrow. Thus, the mutual coupling between the array elements is high [15-18]. After that, the mutual coupling reduction technology is urgent to be boosted. In recent years, a great number of techniques have been presented to reduce the mutual coupling between MIMO antenna elements, such as orthogonal structure [19], electromagnetic band gap (EBG) [20-26]. However, some of them have large array element distances, while others have high mutual coupling between array elements. Several amazing techniques have been reported to reduce the mutual coupling of a MIMO antenna. In [20], a double-layer EBG structure has been introduced into a MIMO antenna to achieve a low mutual coupling. In [21], a slit-patch EBG structure has been presented, which provides a significant mutual coupling reduction between a wide band UWB antennas. Then, miniaturized convoluted direction opening conversed slits have been proposed for reducing the mutual coupling between PIFA antenna elements. The size of each convoluted slit is about one-quarter wavelength and the convoluted direction opening conversed slits give strong effects on the mutual coupling between the PIFA antenna elements. In [22-23], split-ring structured EBGs have been investigated for MIMO antenna coupling reduction. However, the antenna sizes are large. Then, a soft surface has been designed for antenna array decoupling [24]. The coupling has been reduced by about 9 dB with a large antenna size and three stripes. In [25], a multi-layers EBGs have been proposed with a coupling reduction of 24dB at the center frequency. Then, an improved EBG structure has been resented in [26] for a mutual coupling reduction of 26 dB. We can see that the coupling reductions of these antenna arrays are limited and some of them have large sizes. Additionally, a conformal antenna with a coupling reduction has been reduced by using slots. However, it is an un-planar antenna which is difficult to integrate into a portable terminal [27].

In this paper, a multi-layered electromagnetic band gap (ML-EBG) structure is proposed and it is integrated

Submitted On: June 23, 2017
Accepted On: November 29, 2017

into a two-element MIMO antenna array to verify its effectiveness for array mutual coupling reduction. First, the MIMO antenna supported by two same rectangle patch antennas are presented with an edge-to-edge distance of 0.13λ. Next, a periodic ML-EBG structure is placed in the center of the MIMO antenna array. The ML-EBG is designed to be four layers and each layer is connected via a shorted pin. The proposed MIMO antenna with ML-EBG is created and simulated by using the HFSS, fabricated and measured in a chamber. The simulated and measured results have been put forward to verify that the isolation has been improved by 30 dB between the adjacent antenna elements compared to the MIMO antenna without the ML-EBG structures.

II. ANTENNA DESIGN

A ML-EBG structure is proposed and utilized in a MIMO antenna to reduce the mutual coupling between the MIMO antenna elements. The proposed ML-EBG is a 3-D structure. The first layer of the proposed ML-EBG together with the two rectangle patches are printed on a substrate with a permittivity is 4.4, loss tangent is 0.02, and the thickness of 1.6 mm. The other three layers are loaded on the first layer with a uniform distance of 1.6 mm. All the four layers are connected from the upper layer to the bottom layer via a shorted pin which is connected with the ground plane of the MIMO antenna. A great number of works has been done to optimize the number of the layers and the distance between each layer by using the HFSS. The numbers of the layers and the distance are chosen based on the lowest coupling between the antenna elements with respect to S21. The proposed MIMO antenna with ML-EBG is shown in Fig. 1. It is found that the ML-EBG and the two identical patch antennas are installed on the top of the substrate, while there is a ground plane on the bottom of the substrate. The distance between the edge-to-edges of the two identical patch antennas is 0.13λ. Furthermore, three identical ML-EBG cells are installed on the middle of the two-element MIMO antenna array. In this paper, the MIMO antenna array is operated at 2.55 GHz. The initial patch antenna element is obtained from the results [28] and the two patch antenna elements are symmetrically placed on each side of the ML-EBG structures. The ML-EBG can provide a band gap characteristic on the same frequency of the operating band of the MIMO array. It is worth noting that the upper of the ML-EBG is a general rectangle patch, while the other three layers are rectangle patch with split-ring slots shown in Fig. 1 (c), which is to enhance the performance of the proposed coupling reduction structure. The proposed MIMO with ML-EBG is optimized and the related parameters are: L1=28.3mm, W1=15.5mm, d1=15.5mm, d2=15.5mm, f1=f2=f3=H=1.6mm, L2=W2=14mm, h0=1mm, h1=3mm, h2=2mm, h3=0.4mm, h4=1.4mm.

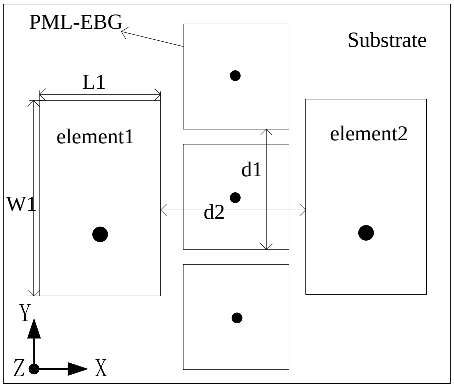

(a) MIMO antenna with ML-EBG structure

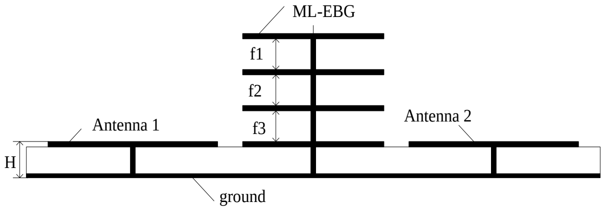

(b) Side view of the MIMO antenna

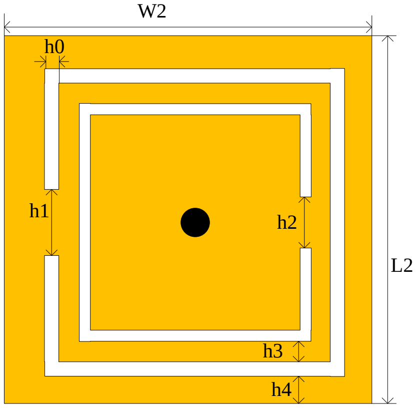

(c) The layers except top of ML-EBG

Fig. 1. Configuration of the proposed MIMO antenna with ML-EBG structures.

III. PERFORMANCE OF THE MIMO ANTENNA WITH ML-EBG STRUCTURES

A. Dispersion diagram of the proposed ML-EBG

Since EBG structure has an ability to suppress surface wave, it can be regarded as an obstacle for special frequency band. Thus, the EBG structure has been used in the middle of a MIMO antenna for coupling reduction applications because the current from one antenna to another antenna will be blocked. The electromagnetic band gap characteristic of the ML-EBG structure shown in Fig. 2 is obtained by the HFSS. T, X and M are the symmetric points in the irreducible Brillouin zone, which can be seen in [28-30]. It can be seen that the frequency band from 2.25 GHz to 3.0 GHz is a band gap which is to suppress the expected surface current.

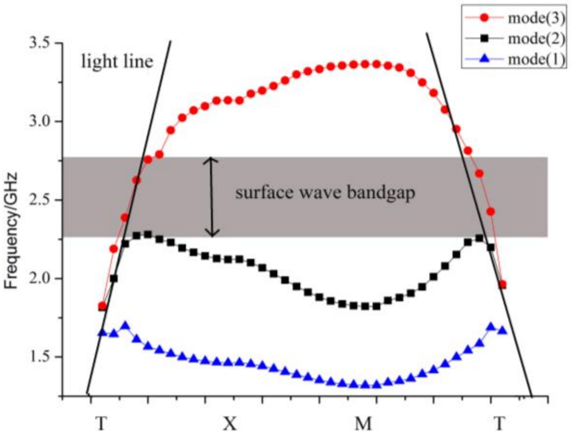

Fig. 2. Characteristic of the proposed ML-EBG.

B. Effects of the ML-EBG

From the characteristic analysis of the proposed ML-EBG, a MIMO antenna is designed, which integrated three ML-EBG cells between the two antennas. Figure 3 illustrates the performance of the MIMO antenna with ML-EBG cells. For the sake of comparison, the MIMO antenna without the designated ML-EBG is also investigated by using the HFSS. The reflection coefficients of both the MIMO antennas with or without the ML-EBG are almost same. It is also found that the bandwidth of the MIMO antenna with ML-EBG cells becomes slightly narrow. However, the mutual coupling of the MIMO antenna with ML-EBG cells between the two antenna elements is reduced according to the S21. It can be seen that the coupling is reduced from -15 dB to -45 dB, which means the isolation of the two-element MIMO antenna achieves an isolation improvement of 30 dB. Thus, the proposed MIMO antenna can provide a high isolation without effects on its bandwidth.

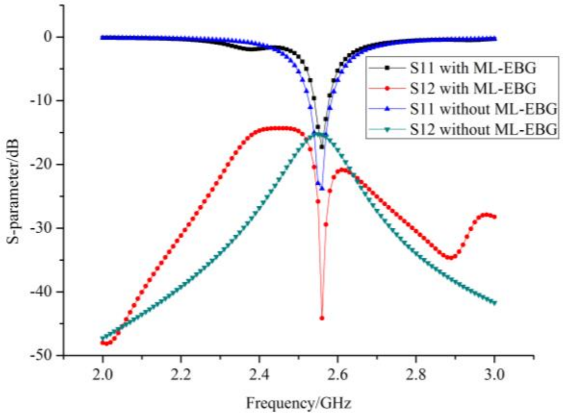

Fig. 3. The MIMO antenna with ML-EBG.

To understand the effects of the ML-EBG, parameter h0,h1,L2 are used for evaluating the performance of the isolation of the MIMO antenna. Figure 4 shows the effects on the isolation with various h0. It is found that the characteristic of the ML-EBG is changed. As h0 ranges from 1.2 mm to 2.0 mm, the band gap rejection frequency moves to high frequency. This is because the h0 changes the resonance characteristics of the split-ring resonator, which results in the band gap frequency shifts to higher frequency from 2.52 GHz to 2.61 GHz. The effects of h1 on the isolation of the MIMO antenna are discussed in Fig. 5. We can also see that the center frequency of rejection band gap frequency band shifts to high frequency. Figure 6 gives the effect of parameter L2 which is the width of the ML-EBG structure. It is observed that the rejection center frequency shifts from high frequency to low frequency with an increment of L2, which is opposite to the shift direction of the h0 and h1. Thus, the ML-EBG can provide a flexible band rejection characteristic to implement the mutual coupling reduction in MIMO antenna array.

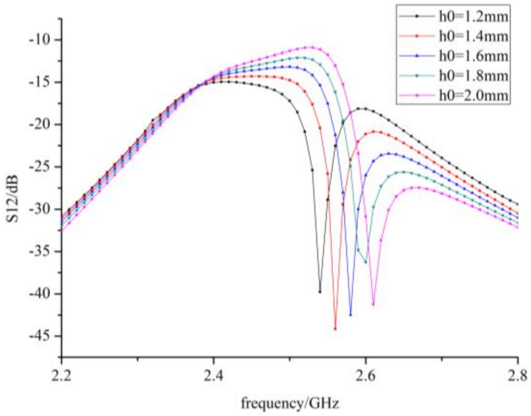

Fig. 4. Effects on the isolation of the MIMO antenna with various h0.

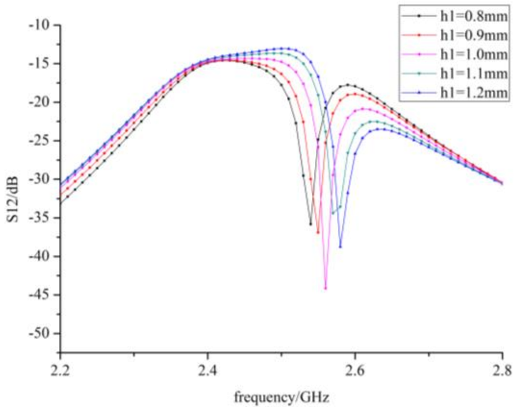

Fig. 5. Effects on the isolation of the MIMO antenna with various h1.

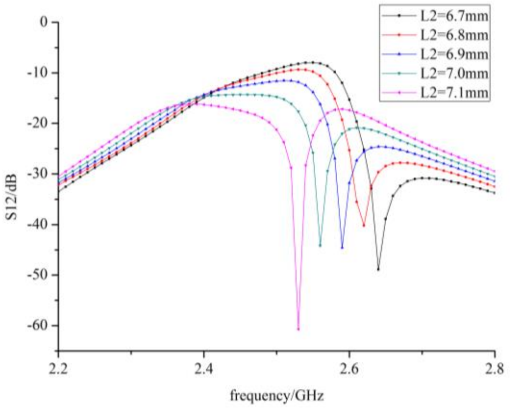

Fig. 6. Effects on the isolation of the MIMO antenna with various L2.

C. Current distribution

The current distributions on the patch antenna of the ground plane and MIMO antenna are shown in Figs. 7 (a) and (b), respectively. Figure 7 (a) shows the current distribution on the ground plane mainly focuses on the left antenna when the MIMO antenna has ML-EBG cells. The current distribution on the ground plane of the MIMO antenna without the ML-EBG flows along the feedings of the two patch antennas. Similarly, the current on the patch antenna concentrates on only one antenna, while the current on the other is very small. However, the currents on the patch antennas of the MIMO antenna without ML-EBG distribute on both antennas. Thus, we can say that the ML-EBG structure effectively suppresses the surface current on the common ground plane of the designed MIMO antenna, and hence, the isolation of the proposed MIMO antenna is significantly improved.

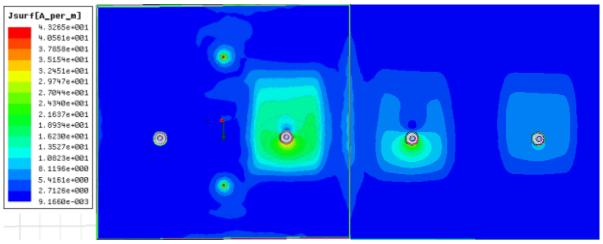

(a) Currents on the ground plane

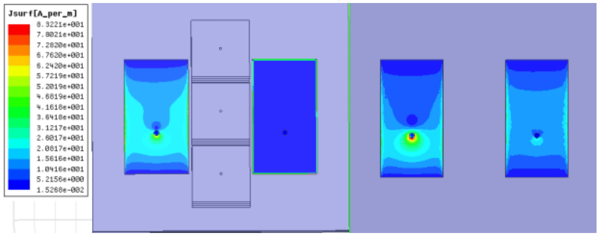

(b) Currents on the patch antennas

Fig. 7. Current distributions of the proposed MIMO antenna.

IV. SIMULATION AND MEASUREMENT RESULTS

In order to fully understand the ML-EBG-based mutual coupling reduction in the MIMO antenna, the optimized MIMO antenna is fabricated and measured in a chamber. The fabricated MIMO antenna integrated with the ML-EBG cells are given in Fig. 8. The results are obtained by using a HP8510C vector network analyzer and the radiation patterns are gotten in a chamber, of the ML-EBG cells. Additionally, the effects of the return loss shift and the radiation patterns may come from the EBGs which affect the wave propagation. In this paper, although the return loss has little effects on the coupling between the two antenna elements has been significantly reduced. The radiation patterns of the proposed MIMO antenna with ML-EBG structure has been measured and shown in Fig. 10. In the measurement, one antenna is excited while the other one is terminated with a 50-Ohm load. It can be seen that the proposed MIMO antenna has independent directional radiation pattern in both E- and H-plane (XOZ- and YOZ- plane). Thus, our proposed antenna is suitable for portable terminal applications.

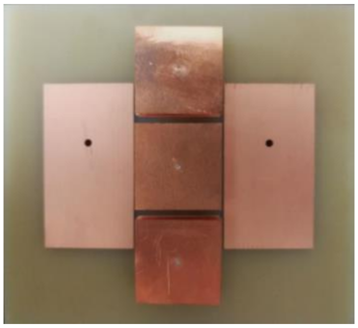

(a) Top view of the fabricated antenna

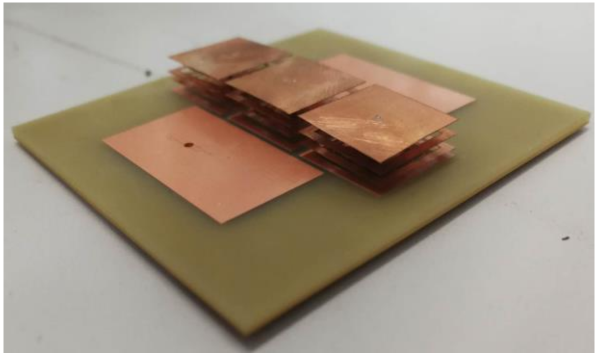

(b) Side view of the fabricated antenna

Fig. 8. Fabricated MIMO antenna with ML-EBG decoupling structures.

The size of the MIMO antenna array and the decoupling effects with different EBGs are compared in Table 1. We can see that the proposed antenna has a smallest edge-to-edge distance of 0.13λ, which is same as that of the referred antenna in [26]. Although the proposed antenna is a little higher than the referred antenna in [26], the proposed antenna has a coupling reduction of 6 dB in comparison with the antenna in [26]. Moreover, the proposed ML-EBG provides the highest isolation for decoupling in a MIMO antenna.

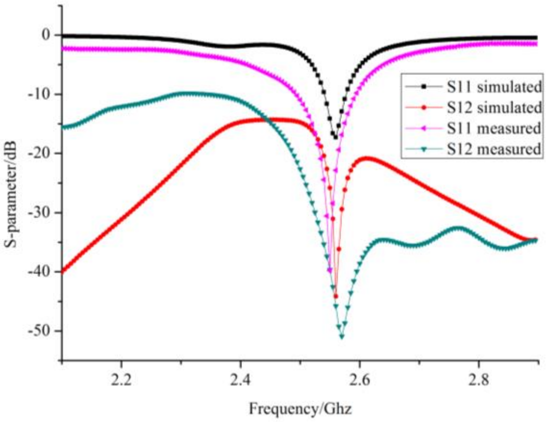

Fig. 9. Measured reflection coefficients and isolation of the proposed MIMO antenna with ML-EBG.

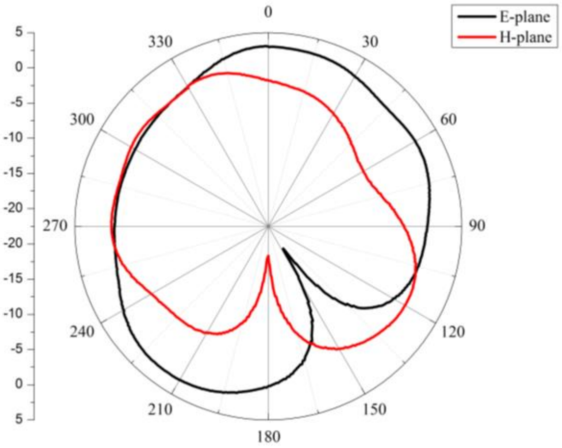

Fig. 10. Radiation patterns of the proposed MIMO antenna with ML-EBG.

Table 1: Comparisons of the decoupling structure with different EBGs

Article	Distance Between Antennas (λ)	Central Frequency (GHz)	Decoupling (dB)
[22]	0.25	5	15
[23]	0.8	13	20
[24]	0.6	1.92	12
[25]	0.47	5.1	20
[26]	0.13	2.55	26
This paper	0.13	2.55	31

V. CONCLUSION

A ML-EBG structure has been proposed and incorporated into a MIMO antenna to verify its performance in surface wave suppression. The band gap characteristics and the key parameters for controlling the ML-EBG has been presented and investigated in detail. The numerical and experimental results have been put forward to verify the effectiveness of the ML-EBG decoupling structure in a two-element MIMO antenna array. The results showed that the two-element MIMO antenna array with an edge-to-edge distance of 0.13λ achieved an isolation of 30 dB by using the proposed ML-EBGs, which means that the mutual coupling reduction is about -30 dB by using the ML-EBG cells. Thus, the proposed antenna can be used for indoor small mobile terminal applications.

ACKNOWLEDGEMENT

This work was also partially supported by the National Key Research and Development Program of China-Government Corporation Special Program (2016YFE0111100), the Science and Technology innovative Talents Foundation of Harbin (2016RAXXJ044), Projects for the Selected Returned Overseas Chinese Scholars of Heilongjiang Province and MOHRSS of China, and the Foundational Research Funds for the Central Universities (HEUCFD1433, HEUCF160815), and China Postdoctoral Science Foundation (2017M620918).

REFERENCES

[1] Y. Li, W. Li, C. Liu and T. Jiang, “Two UWB-MIMO antennas with isolation using sleeve coupled stepped impedance resonators,” *IEEE Asia-Pacific Conference on Antennas and Propagation*, pp. 119-121, 2012.

[2] Y. Li, W. Li, and W. Yu, “A multi-band/UWB MIMO/diversity antenna with an enhance isolation using radial stub loaded resonator,” *Applied Computational Electromagnetics Society Journal*, vol. 28, no. 1, pp. 8-20, 2013.

[3] Y. Li, W. Li, and W. Yu, “A multi-band/UWB MIMO/diversity antenna with an enhance isolation using radial stub loaded resonator,” *Applied Computational Electromagnetics Society Journal*, vol. 28, no. 1, pp. 8-20, 2013.

[4] S. Z. Aziz and M. F. Jamlos, “Compact super wideband patch antenna design using diversities of reactive loaded technique,” *Microwave and Optical Technology Letters*, vol. 58, pp. 2811-2814, Dec. 2016.

[5] N. Kishore, A. Prakash, and V. S. Tripathi, “A multiband microstrip patch antenna with defected ground structure for its applications,” *Microwave and Optical Technology Letters*, vol. 58, pp.

2814-2818, Dec. 2016.

[6] M. Kufa, Z. Raida, and J. Mateu, "Three-element filtering antenna array designed by the equivalent circuit approach," *IEEE Trans. Antennas Propag*, vol. 64. pp. 3831-3839, Sep. 2016.

[7] P. V. Naidu and R. Kumar, "A very small asymmetric coplanar strip fed multi-band antenna for wireless communication applications," *Micro-system Technologies: Micro- and Nanosystems Information Storage and Processing Systems*, vol. 22, pp. 2193-2200, Sep. 2016.

[8] A. Z. Manouare, S. Ibnyaich, A. E. Idrissi, A. Ghammaz, and A. Z. Manouare, "Miniaturized triple wideband CPW-fed patch antenna with a defected ground structure for WLAN/WiMAX applications," *Journal of Microwaves, Optoelectronics and Electromagnetic Applications*, vol. 15 pp. 157-169, Sep. 2016.

[9] C. S. L. Anjaneyulu, "A CPW-fed reconfigurable patch antenna with circular polarization diversity," *International Journal of Microwave and Wireless Technologies*, vol. 7 pp. 753-758, Dec. 2015

[10] S. Ogurtsov and S. Koziel, "Enhancement of circular polarization quality of single-patch two-input microstrip antennas," *Journal of Electromagnetic Wave and Application*, vol. 3, pp. 767-779, 2016

[11] A. A. Razzaqi, B. A. Khawaja, and M. Ramzan, "A triple-band antenna array for next-generation wireless and satellite-based applications," *International Journal of Microwave and Wireless Technologies*, vol. 8, pp. 71-80, Feb. 2016.

[12] S. S. Patel, I. J. Zuazola, and W. G. Whittow, "Antenna with three dimensional 3D printed substrates," *Microwave and Optical Technology Letters*, vol. 58, pp. 741-744, Apr. 2016.

[13] D. F. Guan, Y. S. Zhang, Z. P. Qian, and Y. Li, "Compact microstrip patch array antenna with parasitically coupled feed," *IEEE Trans. Antennas Propag*., vol. 64, pp. 2531-2534, June 2016.

[14] K. Wei, J. Y. Li, L. Wang, and Z. J. Xing, "Mutual coupling reduction by novel fractal defected ground structure bandgap filter," *IEEE Trans. Antennas Propag*., vol. 64, pp. 4328-4335, Oct. 2016.

[15] H. F. Huang and J. F. Wu, "Decoupled dual-antenna with three slots and a connecting line for mobile terminals," *IEEE Antennas and Wireless Propagation Letters*, vol. 14, pp. 1730-1733, 2015.

[16] L. F. Shi, Z. Wei, and C. R. Wang, "EBG combined isolation slots with a bridge on the ground for noise suppression," *International Journal of Electronics*, vol. 103, pp. 1726-1735, Oct. 2016.

[17] N. Rao and D. K. Vishwakarma, "Gain enhancement of microstrip patch antenna using Sierpinski fractal-shaped EBG," *International Journal of Microwave and Wireless Technologies*, vol. 8, pp. 915-919, Sep. 2016.

[18] J. Y. See, S. H, Kim, and J. H. Jang, "Reduction of mutual coupling in planar multiple antenna by using 1-D EBG and SRR structures," *IEEE Trans. Antennas Propag*., vol. 63, pp. 4194-4198, Sep. 2015.

[19] A. Foudazi, M. T. Ghasr, and K. M. Donnell, "Mutual coupling in aperture-coupled patch antennas by orthogonal SIW line," *IEEE International Symposium on Antennas and Propagation (APSURSI)*, pp. 1587-1588, 2016.

[20] Q. Li, A. P. Feresidis, M. Mavridou, and P. S. Hall, "Miniaturized double-layer EBG structures for broadband mutual coupling reduction between UWB monopoles," *IEEE Trans. Antennas Propag*., vol. 63, no. 3, pp. 1168-1171, Mar. 2015.

[21] A. P. Feresudis and Q. Li, "Miniaturised slits for decoupling PIFA array elements on handheld devices," *Electronics Letters*, vol. 48, no. 6, pp. 310-312, Mar. 2012.

[22] M. M. Bait-Suwailam, O. F. Siddiqui, and O. M. Ramahi, "Mutual coupling reduction between microstrip patch antennas using slotted-complementary split-ring resonators," *IEEE Antennas & Wireless Propagation Letters*, vol. 9, pp. 876-878, 2010.

[23] M. S. Alam, M. T. Islam, and N. Misran, "A novel compact split ring slotted electromagnetic bandgap structure for microstrip patch antenna performance enhancement," *Progress in Electromagnetics Research*, vol. 130, pp. 389-409, 2012

[24] E. Rajo-lglesias, O. Quevedo-Teruel, and L. Inclan-Sanchen, "Planar soft surfaces and their application to mutual coupling reduction, *IEEE Transactions on Antennas and Propagation*, vol. 57, no. 12, pp. 3852-3859, 2009.

[25] H. N. B. Phuong, H. V. Phi, N. K. Kiem, and D. N. Dinh, "Design of compact EBG structure for array antenna application," *ATC*, pp. 178-182, 2015.

[26] T. Jiang. T. Jiao, and Y. Li. "Array mutual coupling reduction using L-loading E-shaped electromagnetic band gap structures," *International Journal of Antennas and Propagation*, vol. 2016, pp. 9, 2016.

[27] S. H. Zainud-Deen, H. A. Malhat, and K. H. Awadalla, "Mutual coupling reduction in dielectric resonator antenna arrays embedded in a circular cylindrical ground plane," *Applied Computational Electromagnetics Society Journal*, vol. 25, no. 12, pp. 1129-1135, 2010.

[28] D. Sevenpiper, L. Zhang, R. F. Broas, and N. G. Alexopolous, "High-Impedance electromagnetic surfaces with a forbidden frequency band," *IEEE*

Transaction on Microwave Theory & Techniques, vol. 47, no. 11, pp. 2059-2074, 1999.

[29] http://www.emtalk.com/tut_3.htm

[30] M. Montagna, "Electromagnetic modeling of mm-wave and optical periodic and quasi-periodic structures," *Università Degli Studi Di Pavia*, Doctor Thesis. http://www3.unipv.it/dottIEIE/tesi/2009/m_montagna.pdf

Polarization Insensitive Compact Chipless RFID Tag

Sumra Zeb [1], Ayesha Habib [1], Javeria A. Satti [1], Yasar Amin [1,2], and Hannu Tenhunen [2]

[1] ACTSENA Research Group
University of Engineering and Technology (UET), Taxila, 47050, Pakistan
sumra_zeb@hotmail.com, ayesha.habib@uettaxila.edu.pk, javeriasatti@yahoo.com, yasar.amin@uettaxila.edu.pk

[2] TUCS, Department of Information Technology
University of Turku, Turku, 20520, Finland
hannu@kth.se

Abstract ─ This research article proposes a highly dense, inexpensive, flexible and compact 29 x 29 mm^2 chipless radio frequency identification (RFID) tag. The tag has a 38-bit data capacity, which indicates that it has the ability to label 2^{38} number of different objects. The proposed RFID tag has a bar-shape slot/resonator based structure, which is energized by dual-polarized electromagnetic (EM) waves. Thus, portraying polarization insensitive nature of the tag. The radar cross-section (RCS) response of the proposed tag design is analyzed using different substrates, i.e., Rogers RT/duroid®/5880, Taconic (TLX-0), and Kapton®HN (DuPont™). A comparative analysis is done, which reveal the changes observed in the RCS curve, as a result of using different substrates and radiators. Moreover, the effect on the RCS response of the tag is also examined, by bending the tag at different bent radii. The compactness and flexible nature of the tag makes it the best choice for Internet of things (IoT) based smart monitoring applications.

Index Terms ─ Chipless tag, Radar Cross-Section (RCS), Radio Frequency Identification (RFID).

I. INTRODUCTION

The continuous evolution of Internet of things (IoT) is the outcome of its tremendous scope in the present technological era. The fundamental concept of IoT is to create a web of interconnected smart objects [1]. Thus, IoT guarantees to provide every object with a communication capability and radio frequency identification (RFID) is the key enabler that gives a taste of reality to this aspect [2]. Hence, with the ever growing communication technology, IoT has been the center of attention for researchers to provide real-time solutions for the welfare of humanity [3].

RFID is one of the leading facilitator of IoT, which has spell-bound the global market due to its affordability, increased efficiency, compact size, and numerous applications in logistic [4], supply chain management, vehicle identification [5], baggage tracking on airports, etc. Furthermore, in recent years in order to meet the growing IoT trends, sustained advancement is observed from chip-based to chipless RFID technology. Chip-based tags are not much preferred because of the embedded silicon IC, which ultimately leads to higher price tags that are not suitable for a number of low-cost applications [6]. The identification cost should not be greater than the worth of object/item to be tagged.

Chipless tags do not have an integrated chip (IC) and therefore can be printed easily on to the goods. Moreover, this has also reduced their cost as compared to the chip-based counterparts. Consequently, the research efforts are more concentrated towards the development of low-cost, passive chipless RFID tags.

Various researches have revealed different passive chipless tags having compact and polarization insensitive geometries. In [7], a cross loop resonator based tag with a polarization independent nature is presented. It has the ability to store 20-bit data within a footprint of 4 x 4 cm^2. Then in [8], a chipless tag; consisting of multiple circular ring patch resonators, insensitive to polarization, is disclosed. The tag is designed in a compact dimension of 3 x 3 cm^2 with a coding capacity of upto 19 data bits.

This research work proposes a novel, compact, polarization insensitive, passive chipless RFID tag, comprising of a bar-shape slot/resonator based structure. The proposed tag is capable of yielding 38-bit high data capacity within a compact size of 29 x 29 mm^2. The tag is analyzed for various substrates along with different materials as radiators. Initially, the tag is designed using Rogers RT/duroid®/5880 substrate with copper metal as radiator in a frequency range of 4.6–14.3 GHz. Another tag is inspected using Taconic (TLX-0) along with copper radiator, and its response is analyzed for a frequency range of 4.62–14.4 GHz. Furthermore, to achieve flexibility within a reasonable budget, the tag is also examined using Kapton®HN substrate along with aluminum and silver nano-ink (Cabot ink CCI-300) as a radiator. The

Submitted On: August 11, 2017
Accepted On: January 9, 2018

RF range for Kapton®HN along with aluminum radiator is 5.4–17.97 GHz and 5.3–17.95 GHz for silver nano-ink.

II. WORKING MECHANISM

The passive chipless RFID tag/transponders do not need a battery to power them up [9]. They communicate using the principle of backscattering [10]. The proposed RFID tag has a dual-polarized slot/resonator based structure which means that the tag consists of horizontal and vertical slots. Consequently, the reader circuitry comprises of horizontally and vertically polarized transmitting and receiving antennas. The horizontally polarized transmitting antenna powers up the horizontal slots and the vertically polarized transmitting antenna excites the vertical slots of the RFID tag. Ultimately, the horizontal and vertical receiver antennas, present on the reader side, gather the modulated backscattered signals from the slots arranged in two different orientations. Besides, the dual-polarized structure of the tag depict its polarization insensitive nature. Owing to the fact, and unlike [11], the length of the horizontal slots is kept different from the length of vertical slots in the proposed tag structure, consequently they resonate at different frequencies which prevents mutual interference between the slots. Thus, the proposed tag always yields 38-bits, irrespective of the angle, to which it may be rotated. Ultimately, it can be used as 38-bit polarization insensitive tag. Moreover, the sharpness and the clarity of the resonant dips is not effected by rotating the tag. The RCS response of a single slot/resonator of the tag i.e., *S27* and *S28* on H and V-probe, at different angles of rotation is shown in Fig. 1.

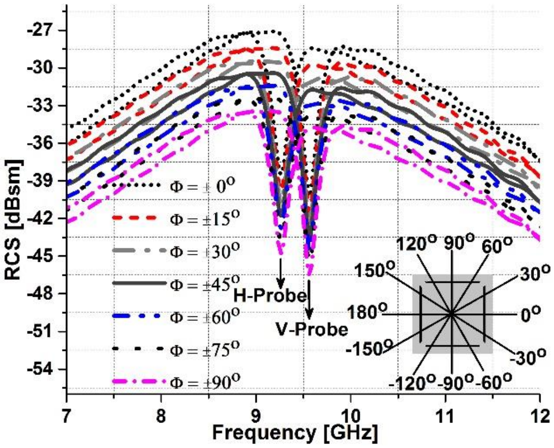

Fig. 1. Polarization insensitivity depicted by the tag.

The E-field circular wave equation is stated as:

$$\mathbf{E}(x,y,z,t)=E_{\circ}\exp\left[\mathrm{j}\left(\omega t-kz\right)\right]\hat{\mathbf{x}}+E_{\circ}\exp\left[\mathrm{j}\left(\omega t-kz+\frac{\pi}{2}\right)\right]\hat{\mathbf{y}},\ (1)$$

where ***E*** represents the electric field, *ω* shows the angular frequency, *(x,y,z)* represents the position vector and *k* constitutes the wave number.

III. PROPOSED CHIPLESS TAG DESIGN

Researchers have explored different aspects of the chipless technology. Efforts have been made to cater high data capacity requirement. The novelty of the proposed tag lies in its flexible nature, along with the ability to yield 38-data bits in a compact size while remaining insensitive to polarization. The tag is designed using CST STUDIO SUITE®. Furthermore, the flexible Kapton ®HN substrate based tag is printed with the help of DMP2800 inkjet printer which consists of a single refillable piezo-based print cartridge having 16 nozzles in a single row. The nozzles have a spacing of 254 µm and can eject drops within a range of 1pl to 10pl subjected to the type of cartridge used. The proposed tag is printed using 10pl cartridge (DM-11610) filled with silver nano-ink, i.e., (Cabot CCI-300). Moreover, the sintering process is carried out at 150 ºC for 2 hours. The printing accuracy is determined by observing the tag under ULTRA-55 Field Emission Scanning Electron Microscope from Carl Zeiss NTS. The 29 x 29 mm^2 chipless tag is capable of encoding 38-bit data which indicates that it can tag 2^{38} number of items/objects. In this research article, the tag design consists of horizontal and vertical bar-shaped slot/resonators of varying lengths, which are arranged in a square shape fashion. The resonating structures are meant for storing the encrypted information. When the EM waves strike these resonators then, each slot, i.e., (gap between the metallic parts), corresponds to one dip, which ultimately represents one bit or a logic state '1'. Subsequently, a logic state '0' is used to represent a slot that has been shorted. The proposed tag design is shown in Fig. 2.

The tag contains thirty-eight slot resonators, out of which nineteen are horizontally polarized, and nineteen are vertically polarized. The slots are represented as *S1-S38*. The horizontal slot resonators are odd numbered and are labeled as *S1, S3* onwards. Horizontally polarized plane wave energizes them. Whereas, the vertical slot/resonators are even numbered and are labeled as *S2, S4* onwards. They are excited by the vertically polarized plane waves. The metallic parts of the tag are referred as *M1-M38* each having width of 0.2 mm. The slot *S1* and *S2* have 8.3 mm and 8.2 mm width, respectively. Besides, all the slots from *S5-S38* have a constant width of 0.3 mm, whereas, slot *S3* and *S4* are optimized to 0.5 mm width. Since, keeping their width equal to 0.3 mm, affects their corresponding resonant dips, and makes them hardly detectable on RCS curve; due to mutual interference. Thus, the widths of all the slots are optimized in such a way, so that sharp and clear resonant dips are achieved on the RCS plot. Furthermore, the tag is kept at a far-field distance from the reader to measure its radar cross section (RCS) response. The far-field distance of the tag can be calculated from (2):

$$R = 2D^2 / \lambda, \tag{2}$$

where D symbolizes the largest dimension of the tag and λ indicates the wavelength. In the proposed research, the largest dimension of the tag is 29 mm or 0.029 m (for use in calculation), whereas λ is calculated using (3):

$$\lambda = c / f, \tag{3}$$

where c is the speed of light, i.e., 3 x 10^8 m/s and f is the central frequency, i.e. 9.45 GHz for this tag. After substituting value of λ in (2) the far field distance comes out to be 52.9 mm. Moreover, the resonant frequency of every individual dip corresponding to each slot can be found by (4) [12]:

$$f_r = \frac{c}{2L}\sqrt{\frac{2}{\varepsilon_r + 1}}, \tag{4}$$

where L is the length of the slot, ε_r refers to the relative permittivity of the substrate and c represents the speed of the light.

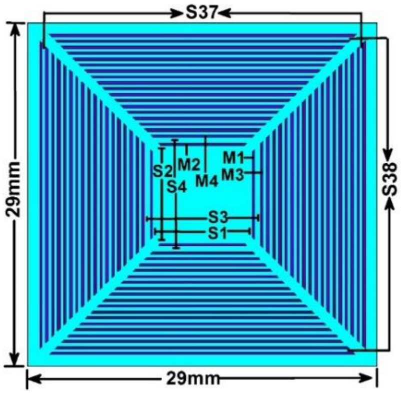

Fig. 2. Proposed tag design.

IV. RESULTS AND DISCUSSION

In this section the RCS plots of the proposed tag structure, analyzed using three different substrates, i.e., Rogers RT/duroid®/5880, Taconic TLX-0 and Kapton®HN, along with three different radiators that include copper, aluminum and silver nano-ink, are demonstrated. It is observed, that the tag design analyzed for different radiators and substrates; (having varying electrical properties), demonstrate a shift in RCS curve on the frequency axis. This is quite evident from the results of simulations discussed in this section. The characteristic comparison of the tag design examined using different substrates is given in Table 1.

A. Tag response using Roger RT/duroid®/5880

The proposed tag analyzed using Rogers RT/duroid®/5880 substrate along with copper metal used as radiator is referred as ‘Tag-A’. Each slot of the tag represents a bit or a logic state-1, which can be seen as a separate resonance dip on the RCS plot, hence the tag yields 38-data bits represented as Tag-A ID. The substrate has a permittivity of 2.2 whereas copper radiator has thickness of 0.035 mm. RF band from 4.6–14.3 GHz is utilized to transmit data. Furthermore, due to low water absorbing property of rigid Rogers RT/duroid®/5880, the tag is ideal for use in high moisture environments. The computed RCS curve of ‘Tag-A’ along with its 38-bit tag ID is shown in Fig. 3.

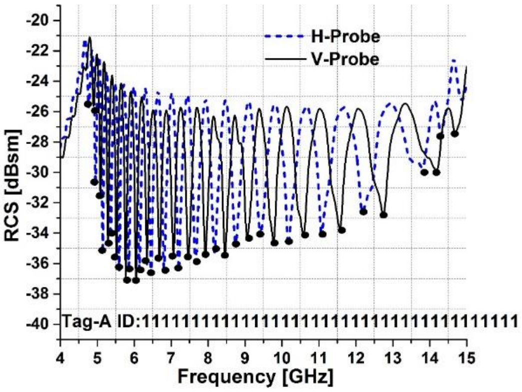

Fig. 3. Computed RCS response of ‘Tag-A’.

Moreover, the proposed tag design analyzed using Taconic TLX-0 substrate along with copper radiator is referred as ‘Tag-B’. The RCS plot of ‘Tag-B’ is similar to the response of the ‘Tag-A’ with a very nominal shift in the frequency band, i.e., from 4.62–14.4 GHz.

B. Tag response using Kapton®HN

Keeping in view the flexibility and excellent ability of the Kapton®HN to maintain its electrical properties over a wide range of temperature, the tag is analyzed for Kapton®HN substrate along with two different radiators, i.e., aluminum and silver nano-ink.

‘Tag-C’ is analyzed using Kapton®HN substrate exhibiting a permittivity value of 3.5, accompanied by aluminum radiator having a thickness of 0.007 mm. It utilizes the frequency band from 5.4–17.97 GHz. Computed RCS response for ‘Tag-C’ is shown in Fig. 4.

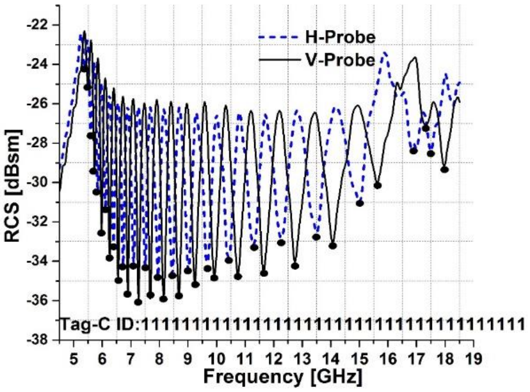

Fig. 4. Computed RCS response of ‘Tag-C’.

Table 1: Characteristic comparison table

Parameters	Tag-A	Tag-B	Tag-C	Tag-D
Substrate	Rogers RT/duroid®/5880	Taconic TLX-0	Kapton®HN	Kapton®HN
Substrate Thickness [mm]	0.787	0.5	0.125	0.125
Permittivity	2.2	2.45	3.5	3.5
Radiator	Copper	Copper	Aluminum	Silver nano-ink
Radiator Thickness [mm]	0.035	0.035	0.007	0.015
Freq. band [GHz]	4.6–14.3	4.62–14.4	5.4–17.97	5.3–17.95
Flexibility	x	x	✓	✓

‘Tag-D’ is analyzed using Kapton®HN substrate, along with silver nano-ink radiator having a thickness of 0.015 mm. The silver nano-ink radiator has a good electrical conductivity, i.e., 9×10^6 S/m, and is potentially resistant to oxidation. Besides, due to its porous nature it can be deployed easily on the substrates thus leading to its full printability. The RCS plot of the ‘Tag-D’ covers the frequency band from 5.3–17.95 GHz. Moreover, both ‘Tag-C’ and ‘Tag-D’, are capable of producing 38-bits which is unveiled by their respective tag ID’s. The computed RCS response of ‘Tag-D’ is shown in Fig. 5.

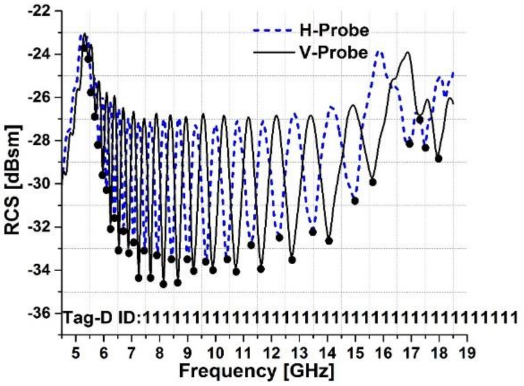

Fig. 5. Computed RCS response of ‘Tag-D’.

A comparison is done between the RCS curves of proposed tag structure, analyzed using different substrates. It is observed that as the permittivity of the substrates decrease, i.e., from 3.5 to 2.2, the resonant dips, drift towards the lower frequencies. Thus, illustrating a left shift in overall RCS response of the tag. This is quite evident from the frequency bands of various tags, as given in Table 1.

Furthermore, a comparative analysis is done between the RCS response of ‘Tag-C’ and ‘Tag-D’; that are analyzed using Kapton®HN substrate along with two different radiators. It is observed that by changing the radiator, while keeping same substrate, there is a slight variation in resonances of the tag. Consequently, a minor frequency shift in RCS curves of the two tags is noticed. This can be visualized from the behaviour of their least significant bits (LSB) that corresponds to the shortest slot. The comparison curve along with the prototype of the proposed tag is shown in Fig. 6.

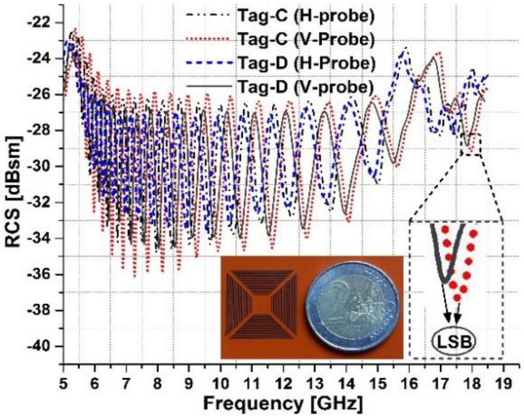

Fig. 6. RCS comparison curve of ‘Tag-C’ and ‘Tag-D’.

Ultimately, to analyze the robustness of the tag, its reliability factor is determined. For this purpose, five to six prototypes of every tag are fabricated and tested experimentally. The tag depicts a tolerance of 0.25% in the desired RF band, whereas 0.3% tolerance is notified along RCS axis. Thus, it is inferred that the proposed tag constitutes a reliable behaviour. The reliable performance of proposed tag on H-probe and V-probe is illustrated in Figs. 7 (a) & (b), respectively.

When incident plane waves excite the tag structure, then each individual slot gives a single resonant dip on a distinct frequency. Each slot corresponds to a logic state ‘1’. These slots are shorted in order to shift the logic state from ‘1’ to ‘0’. A shorted slot does not gives a dip at a specific resonant frequency, thus corresponds to ‘0’ logic state. Hence, by shortening; different tag IDs can be assigned to each tag, which ultimately, prevents the collision of data in the network. Since in the proposed tag, each slot produces a resonant dip at a different frequency; thus, shorting any slot will have a minor effect on the frequency response of the neighboring slots [13]. A comparison of tag carrying all 1’s; denoted by 11111111111111111111111111111111111111 tag ID, with the tag comprising of shorted *S10*, *S17* and *S24* slots; represented by the unique tag ID:

11111111101111110111111011111111111111 is illustrated in Fig. 8.

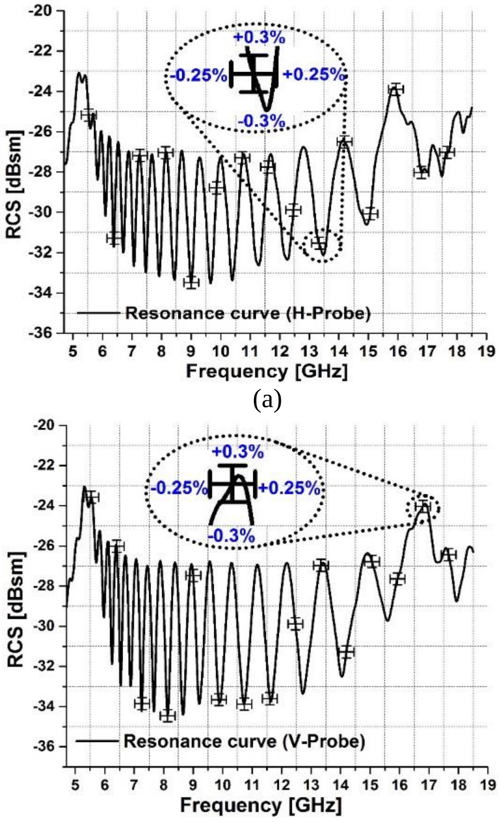

(a)

(b)

Fig. 7. (a) Reliability curve of ‘Tag-D’ (H-Probe), and (b) reliability curve of ‘Tag-D’ (V-Probe).

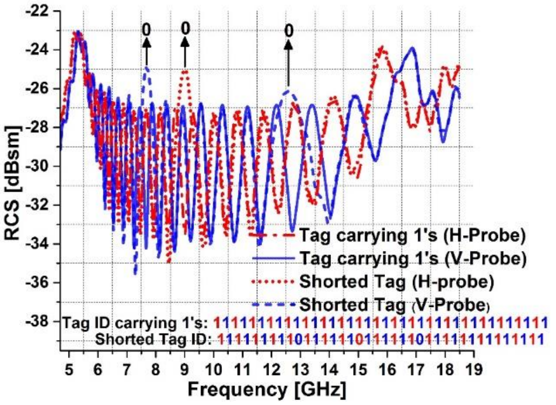

Fig. 8. Comparison of reference and shorted tag.

V. BENDING EFFECT ON TAG

The RCS response of the proposed tag is also examined by bending it at different bent radii, i.e., 18 mm, 60 mm, 80 mm, 90 mm. While performing the experiments the tag is attached to cylindrical polystyrene molds; which are designed with different curvature radii; corresponding to the various bending radii at which the RCS response of the tag is to be analyzed. The molds are designed using polystyrene material because it has a relative permittivity approximately equal to unity, which does not effects the RCS response of the tag. It is observed that with the decrease in the bending radius of the tag, its RCS response is effected yielding less prominent but still detectable resonant dips as in [10]. Hence, the data stored in the tag can be retrieved successfully at different bending radii. The RCS response of the tag on H and V-Probe at various bent radii represented by r, along with the proposed tag bent at a radius of 18 mm are illustrated in Figs. 9 (a) & (b), respectively.

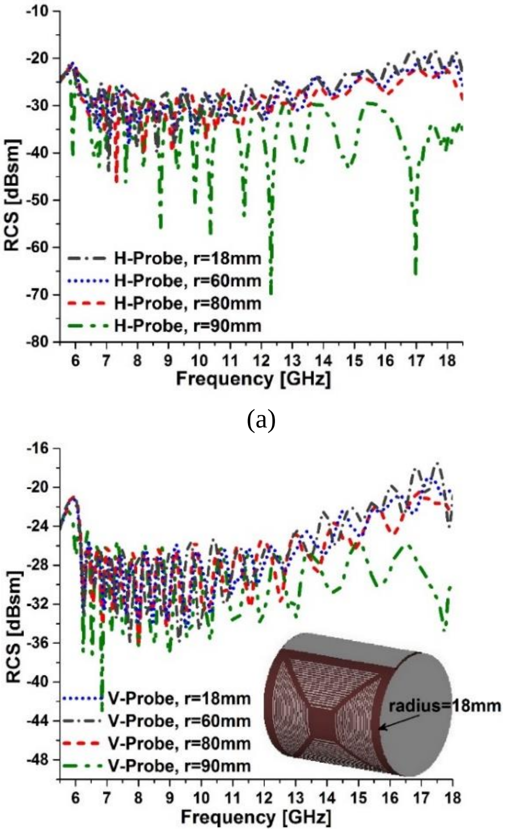

(a)

(b)

Fig. 9. (a) Bending effect on tag (H-Probe), and (b) bending effect on tag (V-Probe).

VI. COMPUTED AND MEASURED RESULTS

The computed and measured results of the proposed tag design, on H-probe and V-probe are depicted in Figs. 10 (a) & (b), respectively. The measured and computed results of the tag demonstrate an acceptable agreement. A slight shift in the resonances is observed, as detected by the reader circuitry. The testing of the tag is done in standard environment using a bistatic radar system [13].

The experimental setup used for testing of the tag consists of a Vector Network Analyzer (VNA) R&S®ZVL13 and two horn antennas, one is transmitter and the other is receiver. Transmitter antenna directs interrogator signal on the transponder, set at a far-field distance. The receiver antenna then collects the backscattered signal encoded with unique identification code using VNA.

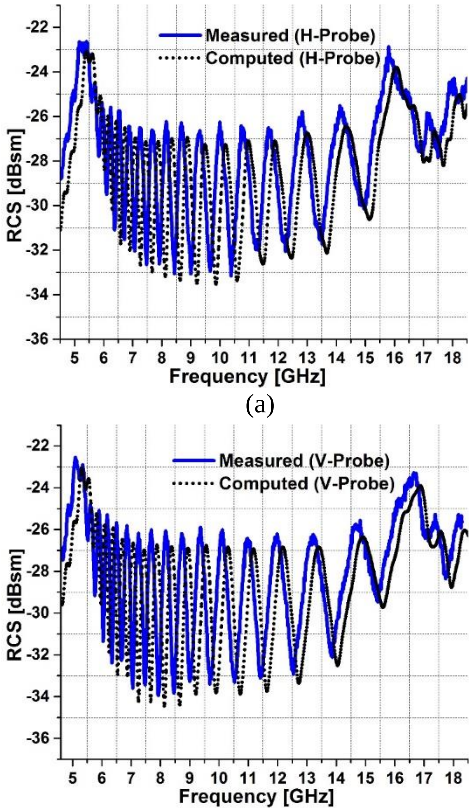

(a)

(b)

Fig. 10. (a) Measured RCS response (H-Probe), and (b) measured RCS response (V-Probe).

Table 2 shows a comparative study of the previous research works and the proposed tag design.

Table 2: Comparison with previous research work

Parameters	I-Slot [11]	Circular [14]	Square [15]	Proposed Research
Size [cm^2]	7.29	2.36	9	8.41
Tans. bits	32	9	5	38
Bit density [Bits/cm^2]	4.38	3.80	0.55	4.51
Flexibility	x	x	x	✓

From Table 2, it is evident that the proposed tag has the capability to encode 38-bit data in a miniaturized footprint of 8.41 cm^2. Thus, yielding a high bit density comparatively. Moreover, the flexible characteristic of the tag allows it to be deployed on irregular surface.

VII. CONCLUSION

A compact 29 x 29 mm^2 chipless RFID tag, having a high data capacity of 38-bits is revealed in this research work. The proposed tag structure yield very stable resonant dips, when analyzed for multiple substrates. The tag analyzed using Kapton®HN substrate is found to be of utmost significance; because of its flexible nature, easy printability and stability toward thermal changes. The tag analyzed using Rogers RT/duroid®/5880 substrate exhibits electrical stability towards high humidity levels. Consequently, providing an optimal solution for moisture rich atmospheres. Thus, the proposed tag can be used in different environmental conditions; becoming the ideal choice for IoT based industrial applications.

ACKNOWLEDGEMENTS

Vinnova (The Swedish Governmental Agency for Innovating Systems) and UET, Taxila, Pakistan, financially assisted this work.

REFERENCES

[1] M. Bolic, M. Rostamian and P. M. Djuric, “Proximity detection with RFID: A step towards the internet of thimgs,” *IEEE Pervasive Comput.*, vol. 14, pp. 70-76, 2015.

[2] A. Habib, M. A. Azam, Y. Amin, and H. Tenhunen, “Chipless slot resonators for IoT system identification,” *IEEE Int. Conf. on Electro Inf. Technol. (EIT*), Grand Forks, ND, pp. 0341-0344, 2016.

[3] J. Mccann and K. K. Leung, “A survey on the ietf protocol suite for the internet of things: Standards, challenges, and opportunities,” *IEEE Wireless Commun.*, vol. 20, pp. 91-98, 2013.

[4] C. Yuqiang, G. Jianlan, and H. Xuanzi, “The research of internet of things' supporting technologies which face the logistics industry,” *Int. Conf. on Comput. Intell. and Security (CIS)*, Nanning, pp. 659-663, 2010.

[5] A. Toccafondi, C. D. Giovampaola, P. Braconi, and A. Cucini, “UHF-HF RFID integrated transponder for moving vehicle identification,” *ACES Journal*, vol. 25, pp. 543-551, June 2010.

[6] Y. Feng, L. Xie, Q. Chen, and L. R. Zheng, “Low-cost printed chipless RFID humidity sensor tag for intelligent packaging,” *IEEE Sensors J.*, vol. 15, pp. 3201-3208, 2015.

[7] V. R. Sajitha, C. M. Nijas, T. K. Roshana, K. Vasudevan, and P. Mohanan, “Compact cross loop resonator based chipless RFID tag with polarization insensitivity,” *Microw. Opt. Technol. Lett.*, vol. 58, pp. 944-947, 2016.

[8] A. Vena, E. Perret, and S. Tedjini, “High-capacity chipless RFID tag insensitive to the polarization,” in *IEEE Trans. Antennas Propag.*, vol. 60, pp.

4509-4515, 2012.

[9] A. Vena, E. Perret, and S. Tedjini, "Toward a reliable chipless RFID humidity sensor tag based on silicon nanowires," *IEEE Trans. Microw. Theory Techn.*, vol. 64, pp. 2977-2985, 2016.

[10] D. Betancourt, K. Haase, A. Hübler, and F. Ellinger, "Bending and folding effect study of flexible fully printed and late-stage codified octagonal chipless RFID tags," *IEEE Trans. Antennas Propag.*, vol. 64, pp. 2815-2823, 2016.

[11] M. A. Islam and N. Karmakar, "Compact printable chipless RFID tags using polarization diversity," *42nd European Microw. Conf.*, Amsterdam, pp. 912-915, 2012.

[12] T. Dissanayake and K. P. Esselle, "Prediction of the notch frequency of slot loaded printed UWB antennas," *IEEE Trans. Antennas Propag.*, vol. 55, pp. 3320-3325, 2007.

[13] L. Xu and K. Huang, "Design of compact trapezoidal bow-tie chipless RFID tag," *Int. J. Antennas Propag.*, vol. 2015, pp. 7, 2015.

[14] M. Martinez and D. van der Weide, "Compact slot-based chipless RFID tag," *IEEE RFID Technol. Applicat. Conf. (RFID-TA)*, Tampere, pp. 233-236, 2014.

[15] F. Costa, S. Genovesi, and A. Monorchio, "A chipless RFID based on multiresonant high-impedance surfaces," *IEEE Trans. Microw. Theory Techn.*, vol. 61, pp. 146-153, 2013.

Sumra Zeb received her B.S. degree in Electrical Engineering from Comsats Institute of Information Technology in 2016. She joined University of Engineering and Technology, Taxila the same year as a full-time scholar where she is pursuing her Master's degree focused on Chipless RFID Tags under the supervision of Dr. Yasar Amin.

Ayesha Habib is working as a Research Scholar at Telecommunication Engineering Department, University of Engineering and Technology Taxila, Pakistan. She did her B.Sc. in Telecommunication Engineering from APCOMS, in 2012. She has completed her M.S. in Telecommunication Engineering from UET, Taxila Pakistan in 2014. In 2014, she has joined ACTSENA research group as a Research Scholar and has started her Ph.D. under the supervision of Dr. Yasar Amin. Her main research interests include Chipless RFID Tags with Integrated Sensor.

Javeria Anum Satti did B.S. in Telecommunication Engineering from University of Engineering and Technology, Taxila and then she joined the same institute as full-time researcher, to persue her Master's degree focused on High Dense Chipless RFID Tags.

Yasar Amin is Chairman and Associate Professor of Telecommunication Engineering Department, University of Engineering and Technology Taxila, Pakistan. He is the Founder of ACTSENA Research Group at UET Taxila, Pakistan. He did his B.Sc. in Electrical Engineering in 2001 and MSc in Electrical Engineering in 2003 from Royal Institute of Technology (KTH), Sweden. His Ph.D. is in Electronic and Computer Systems from Royal Institute of Technology (KTH), Sweden, with the research focus on printable green RFID antennas for embedded sensors, while has MBA in Innovation and Growth from Turku School of Economics, University of Turku, Finland. He is presently serving as leading Guest Editor at two International Journals and an active reviewer of more than a dozen well reputed International journals. He has contributed to over 20 journal papers, over 30 reviewed international conference papers.

Hannu Tenhunen is the Chair Professor of Electronic Systems at Royal Institute of Technology (KTH), Stockholm, Sweden. Prof. Tenhunen has held Professor position as Full Professor, Invited Professor or Visiting Honorary Professor in Finland (TUT, UTU), Sweden (KTH), USA (Cornel U), France (INPG), China (Fudan and Beijing Jiaotong Universities), and Hong Kong (Chinese University of Hong Kong), and has an honorary doctorate from Tallinn Technical University. He has been the director of multiple national large-scale research programs or being an initiator and director of national or Knowledge and Innovation Community EIT ICT Labs.European graduate schools. He has actively contributed to VLSI and SoC design in Finland and Sweden via creating new educational programs and research directions, most lately at European level as being the EU-level Education Director of (EIT), and its Knowledge and Innovation Community EIT ICT Labs.

A Wideband Circular Polarization Antenna for UHF Tags

Mohammad H. Zolghadri and Shahrokh Jam

Department of Electrical and Electronic Engineering
Shiraz University of Technology, Shiraz, 715155-313, Iran
m.zolghadri@sutech.ac.ir, jam@sutech.ac.ir

Abstract **─** In this paper, a low profile antenna for UHF Radio Frequency Identification (RFID) Tags with wideband circular polarization (CP) is proposed to solve the polarization mismatch in RFID systems. This antenna consists of two orthogonal dipole with unequal slots for realizing circular polarization radiation and a new matching network. For reducing size, a row-shaped tip loading is used. The measurement result of return loss bandwidth is 40 MHz (895-935 MHz) and 3-dB axial ratio bandwidth is 25 MHz (910-935 MHz). The overall size of antenna has been reduced to $(0.19\,\lambda_0 \times\ 0.19\,\lambda_0 \times\ 0.005\,\lambda_0\ )$ at 915 MHz compared to previous works. Besides, other advantages of this design are wideband impedance matching and CP bandwidth.

Index Terms **─** Axial ratio, circular polarization crossed dipole, RFID, tag antenna.

I. INTRODUCTION

Nowadays, the applications of RFID systems in the UHF band has gained popularity in many areas such as retail industry, access control, security systems and, assets management [1]. Features like small tag size and increasing reading range are the major challenging topics in designing RFID systems. One of the useful ways to increase the reading range is to design antenna with broadband CP. As a matter of fact, most commercial RFID systems use reader antenna with circular polarization. However, the majority of RFID tags' antenna are designed as microstrip or dipole antennas with linear polarization (LP) [2-6]. Because of the polarization mismatch between reader and tag antennas, only half of the power is delivered by LP Tag. Therefore, if polarization of tag's antenna is CP, the power received by tag will be increases by 3 dB, as a result, the reading range improves by 41 percent. Moreover, CP Tag antenna with a wideband matching network and miniaturized size has been considered for commercial applications.

In recent years, design of wideband CP antennas for tags have been attracted a lot of research interests [7-10]. In [7], two dipole antennas are organized orthogonally for creating CP polarization. This structure can attain wideband CP and compact size $(0.26\,\lambda_0 \times\ 0.26\,\lambda_0 \times\ 0.005\,\lambda_0$ at 915 MHz), with major design disadvantage of unwanted coupling between matching network and radiation elements. Although, the CP tag antenna presented in [8] has a desired gain (6 dBi) and reading range (8 m), this structure has large area $(0.58\,\lambda_0 \times 0.39\,\lambda_0 \times 0.07\,\lambda_0)$ at 915 MHz and narrow CP bandwidth 15 MHz $(900 - 915\ MHz)$. A low profile microstrip tag antenna with coupling-feed has been proposed in [9] which its size has been reduced to $(0.23\,\lambda_0 \times 0.23\,\lambda_0 \times 0.005\,\lambda_0)$ at 925 MHz. The important disadvantage of this structure is having small gain (-14 dBi) and narrow CP bandwidth (6 MHz). Moreover, the structure in [10] exhibits a wider CP bandwidth, 20 MHz $(903 - 923\ MHz)$, but it has relatively large occupied area $(0.33\,\lambda_0 \times 0.33\,\lambda_0 \times 0.005\,\lambda_0)$ at 915 MHz. Moreover, in [11], a compact RFID tag antenna with CP for metallic objects has been proposed. The antenna has a size $(0.22\,\lambda_0 \times 0.22\,\lambda_0 \times 0.004\,\lambda_0)$ at 915 MHz and a 3 dB CP bandwidth of 12 MHz.

In this paper, a new wideband CP RFID tag antenna is proposed. A cross dipoles with reactively loading is modified from [12] with row shape tip loading to realize CP radiation. This structure consists of cross slot loaded dipole and new matching network which contributes to improve features such as CP and return loss bandwidth and size reduction. The bandwidth of CP and return loss cover the RFID bands of North and South America.

II. PROPOSED STRUCTURE

The geometry and fabricated of the proposed wideband CP RFID Tag's antenna is shown in Fig. 1. It was fabricated on a FR4 substrate ($tan\delta = 0.02$, $\varepsilon_r = 4.4$) with dimension of D $(66\ mm \times 66mm\ )$ and thickness of H $(1.6\ mm)$. The structure includes two cross dipoles with same width (W) that loaded by two pairs of slots with equal width (T) and unequal lengths $(S1,\ S2)$. The dimensions of antenna are reduced to $(0.19\,\lambda_0 \times 0.19\,\lambda_0 \times 0.005\,\lambda_0)$ at 915 MHz by using arrow form tip loading with equal width $(W1)$ and (A), in the end of dipoles. Also, an Alien IC Higgs (RFID chip) with impedance of $(13.5 - j111\ \Omega)$ at 915 MHz is attached, which is the green zone as shown in Fig. 1.

Submitted On: July 5, 2016
Accepted On: October 4, 2017

Hence, conjugate matched impedance $(13.5 + j111\ \Omega)$ has to be provided by proposed tag antenna at this frequency. In this structure, to attain an inductive reactance, a modified T matching network that their dimensions $(\mathrm{M}, \mathrm{M}_1,\ \ldots\ , \mathrm{M}_4)$ are shown in Fig. 1, is used.

In this section, the procedure for achieving CP radiations and design matching network are presented. First, two dipoles with conjugate impedance are simulated separately, then two dipoles are arranged to crossed dipoles form, matching network is added and finally optimization for minimum return loss and axial ratio is held implemented.

A. Designing two dipoles

To attain a CP radiation pattern, two orthogonal field components with equal amplitude and 90 degree phase difference are needed. The basic idea that was used in the proposed structure is two dipoles with complex conjugated impedance of equal imaginary and real parts $(Z_1 = R + jX,\ Z_2 = R - jX,\ R = X)$ [13]. Therefore, the impedance phase of dipoles are $+45^o$ and -45^o. The two dipoles with unequal slots and same length contribute to inductive and capacitance reactance. The capacity tip loading as arrow and slot shape in the dipoles were used in this design to reduce the size of antenna. The increase the inductance, L and capacitance, C cause to reduce the frequency resonance which is given by (1):

$$f_C = \frac{1}{2\pi\sqrt{LC}}\ . \qquad (1)$$

The overall dimensions of two dipoles are decreased by arrow form tip loading in the end of them as shown in Fig. 2. The parameters A, W, L , $S1$ and $S2$ are used as variables optimized to achieve minimum axial ratio. With $A = 22.4\ mm$, $W = 6.6\ mm$, $L = 35.8\ mm$, $S1'' = 21.8\ mm$, the input impedance of one of the dipoles is $(54.1 - j54.9\ \Omega)$. Correspondingly, with $S2'' = 9.3\ mm$, the input impedance of another dipole is $(44.3 + j48.2\ \Omega)$. As seen in Fig. 2, if the length of its slot decreases, the effect of capacitance decreases and versa. Therefore the reactance of dipole becomes more capacitive.

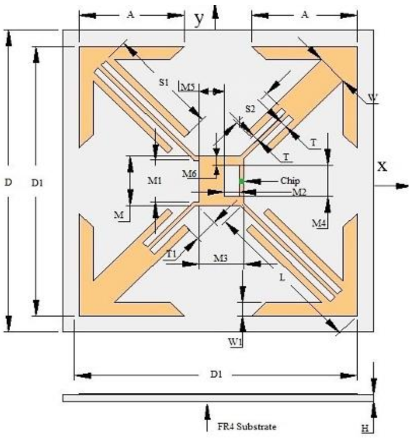

(a)

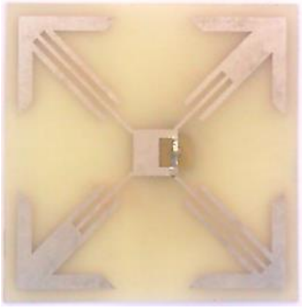

(b)

Fig. 1. (a) Geometries of the proposed tag antenna. (b) Photograph of the fabricated tag antenna.

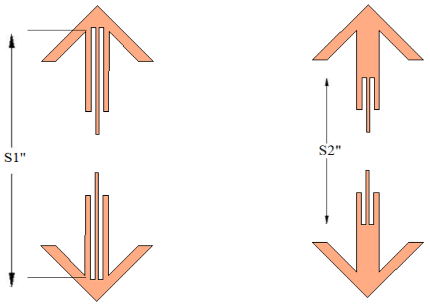

$(54.1 - j54.9\ \Omega)$ $(44.3 + j48.2\ \Omega)$

Fig. 2. Two dipoles with conjugated impedances.

B. Forming orthogonal dipoles

After determining the dimensions of two dipoles in center frequency, two dipoles are arranged to form the orthogonal dipole as shown in Fig. 3, with $M = 8\ mm$ and through short feed lines with inductance property in the center of the antenna. In this condition the input impedance of the proposed structure is $(54.1 + j10\ \Omega)$.

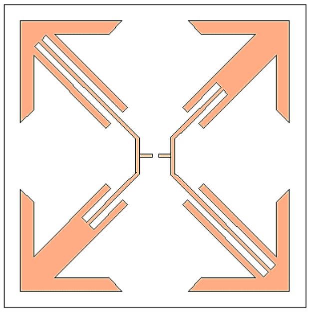

Fig. 3. Geometry of CP crossed dipole antenna without matching network.

C. Impedance matching network

After forming orthogonal dipole, it must be matched to RFID chip. The matching network consists of a modified T matching network to match the impedance tag antenna with RFID chip (Alien IC Higgs). A T match connection shown in Fig. 4. The first dimensions of T-match network are obtained from T matching network formulas (2) to (5), which explained in [14]:

$$Z_{in} = \frac{2Z_t(1+\alpha)^2 Z_A}{2Z_t + (1+\alpha)^2 Z_A}, \tag{2}$$

$$Z_t = jZ_0 tanK\frac{M}{2}, \tag{3}$$

$$Z_0 \cong 276log_{10}\frac{M_2}{\sqrt{r_e r'_e}}, \tag{4}$$

$$\alpha = \frac{\ln\left(M_2/r'_e\right)}{\ln\left(M_2/r_e\right)} \quad r_e = 0.25M_5 \quad r'_e = 8.25M_6, \tag{5}$$

where $Z_{in}$is the impedance at the chip terminal, Z_t is the impedance of the short circuit stub with T form and Z_0 is the characteristic impedance of the two transmission line with spacing $M2$ as shown in Fig. 4. It is obvious that for matching, Z_{in} must be equal to conjugate of chip impedance.

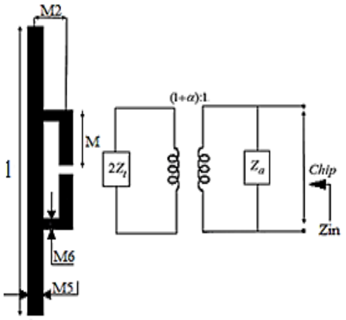

Fig. 4. The T-match connection.

The dimensions of modified network are represented by $(M, M1, \ldots, M6)$ in Fig. 1. The most important characteristics of the proposed modified T matching network are simplicity of tuning capability in comparing with another T matching network which has been proposed in a previous work [7].

The effective parameters on input resistance and reactance of suggested matching network are $(M, M2)$. The simulated input impedance of the proposed structure by tuning the lengths $(M, M2)$ of T matching network are shown in Figs. 5 and 6. The simulation results of input impedance when the length M increases from $8\,mm$ to $10\,mm$ are shown in Fig. 4. Also, the simulated input impedance of the proposed structure is varied by increasing the width $M2$ of T matching network from $2.5\,mm$ to $4.5\,mm$ are given in Fig. 6. As it is seen in Figs. 5 and 6, both input resistance and reactance can be matched in conjugate to chip impedance by adjusting parameters $M, M2$.

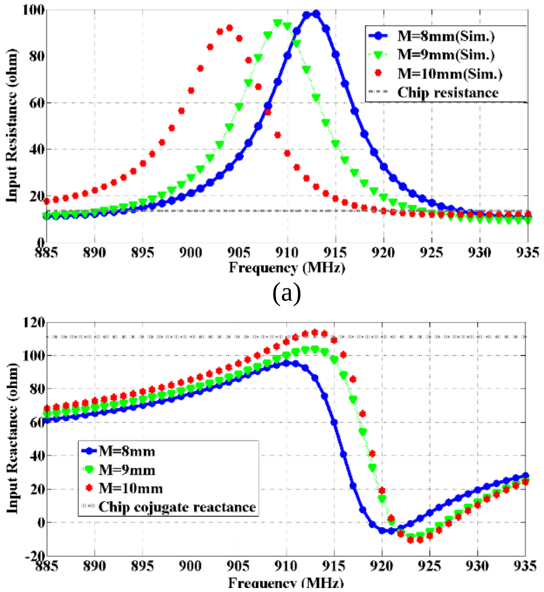

(a)

(b)

Fig. 5. Simulated input impedances by tuning parameter M, when $A = 22.5\,mm$, $S1 = 23.5\,mm$, $S2 = 10\,mm$, $M1 = 8\,mm$, $M2 = 3\,mm$, $M3 = 9.5\,mm$, $M4 = 6.5\,mm$. (a) Input resistance. (b) Input reactance.

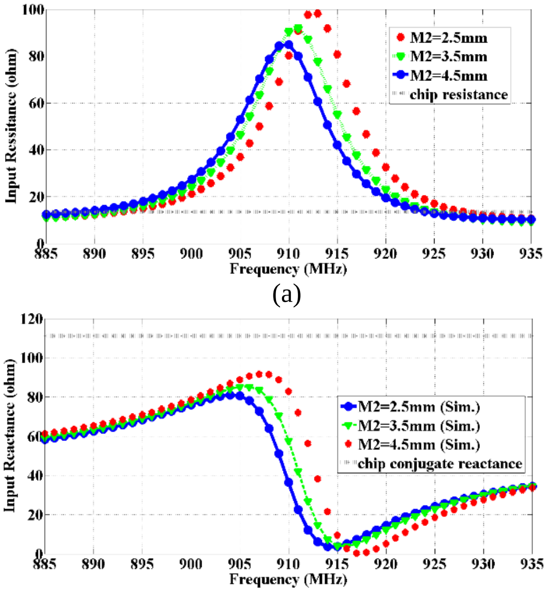

(a)

(b)

Fig. 6. Simulated input impedances by tuning parameter M2, when $A = 22.5\,mm$, $S1 = 23.5\,mm$, $S2 = 10\,mm$, $M = 10\,mm$, $M1 = 8\,mm$, $M3 = 9.5\,mm$, $M4 = 6.5\,mm$. (a) Input resistance. (b) Input reactance.

D. Introducing circular polarization

CP can be attained when the phase time difference between two orthogonal radiation fields E_x and E_y is odd multiples of 90 degree and the amplitude of the two field components are similar:

$$\text{CP conditions} \begin{cases} \angle E_y - \angle E_x = \begin{cases} +90^o (LHCP) \\ -90^o (RHCP) \end{cases} . \\ |E_y| = |E_x| \end{cases} \quad (6)$$

The effects on CP bandwidth ($AR \leq 3\ dB$) of the proposed structure are illustrated in Fig. 7 by increasing the tuning arrows length (A) from 21.5 mm to 23.5 mm. Through determining and selecting a proper length (A), the desirable bandwidth of CP can be achieved.

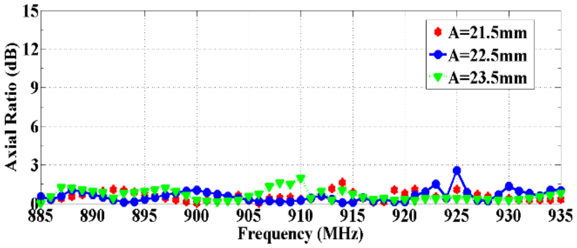

Fig. 7. Simulated axial ratio by tuning parameter A, when, $S1 = 23.5\ mm$, $S2 = 10\ mm$, $M = 10\ mm$, $M1 = 8\ mm$, $M2 = 3\ mm$, $M3 = 9.5\ mm$, $M4 = 6.5\ mm$.

E. Optimization

Finally, in this section through studying the effects of various parameters in the antenna performance, we obtain the optimum of their values. The parameters are optimized by Genetic Algorithm in HFSS software for desired axial ratio and resonant frequency. The final dimensions for the optimized RFID tag antenna are listed in Table 1.

Table 1: Optimized dimensions of antenna (mm)

$D = 67.4$	$D1 = 60.1$	$A = 22.4$	$W = 6.6$
$L = 35.8$	$S1 = 23.9$	$S2 = 10.1$	$T = 1.3$
$T1 = 5.7$	$W1 = 2.8$	$H = 1.6$	$M = 10.2$
$M1 = 8.3$	$M2 = 3.2$	$M3 = 9.6$	$M4 = 6.3$

III. RESULT AND DISCUSSION

Simulation and optimization of the proposed CP tag antenna are performed by commercially available electromagnetic simulation software (HFSS), in which the initial results of the suggested tag antenna can be comprehensively studied.

The input impedance of the fabricated antenna is measured using single-ended probe measurement method that requires the following equipment: a network analyzer (Agilent E8364B), flexible test cable, and TDR probe.

The CP bandwidth of the proposed antenna is investigated by presenting the amplitudes ($|E_x|, |E_y|$) and phase (φ_x, φ_y) of the two orthogonal radiation field in Fig. 8. Amplitudes and their phase diagram in Figs. 8 (a) and (b) show the phase φ_y follow φ_x by 90^o difference approximately. Hence, these results confirm that proposed antenna radiate RHCP.

To illustrate the CP radiation of the proposed antenna, the surface current distributions at 915 MHz are depicted in Fig. 9. In these figures, it is notable that current moves in the clockwise direction as ωt increases, which shows exciting a RHCP radiation.

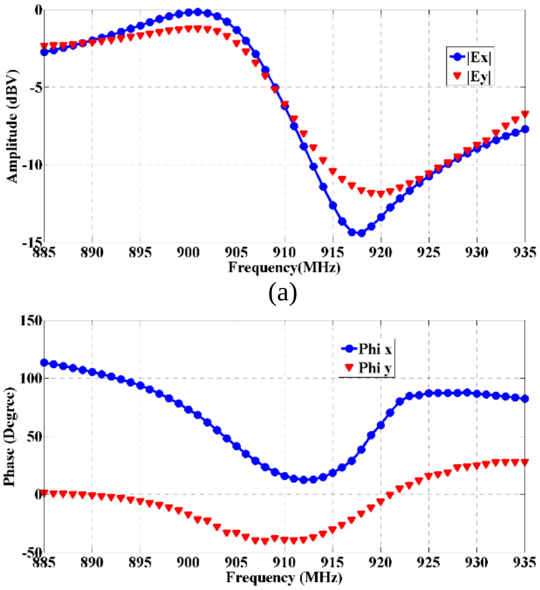

(a)

(b)

Fig. 8. Simulated radiation fields (Ex and Ey) in bore sight direction: (a) amplitude and (b) phase.

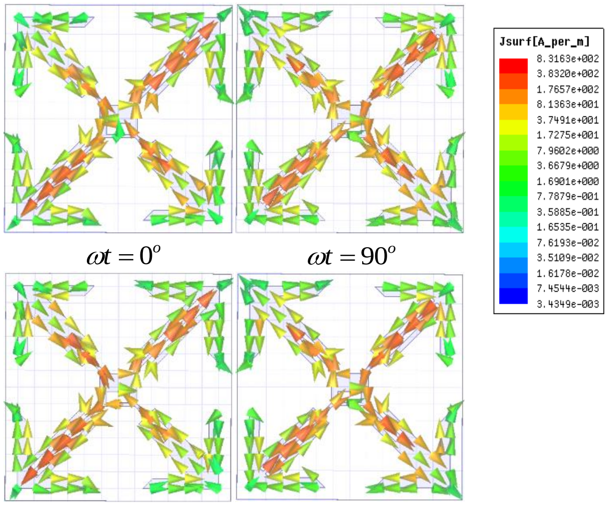

$\omega t = 0^o$ $\omega t = 90^o$

$\omega t = 180^o$ $\omega t = 270^o$

Fig. 9. Simulated surface current distributions at four phase angles in 915 MHz.

The simulated and measured input impedances and return losses of the optimized tag antenna are presented in Figs. 10 and 11, respectively. The simulated input impedance is $(20 + j66\,\Omega)$, and the measured input impedance for the proposed antenna is $(14 + j55\,\Omega)$ at $915\,MHz$. The slight frequency shift in simulated and measured result is due to the error in dielectric constant of FR4 in practical.

The simulated $-3\,dB$ return loss bandwidth of the proposed tag antenna is $35\,MHz\,(900 - 935\,MHz)$, that the measured $-3\,dB$ return loss bandwidth $40\,MHz$ $(895 - 935\,MHz)$ which is slightly wider than the simulation results. The simulated and measured AR are shown in Fig. 12.

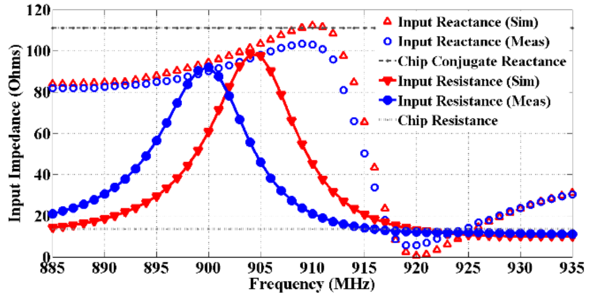

Fig. 10. Simulated and measured input impedance optimized antenna.

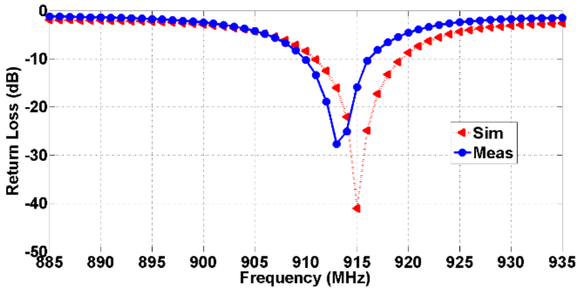

Fig. 11. Simulated and measured return losses of the proposed tag antenna.

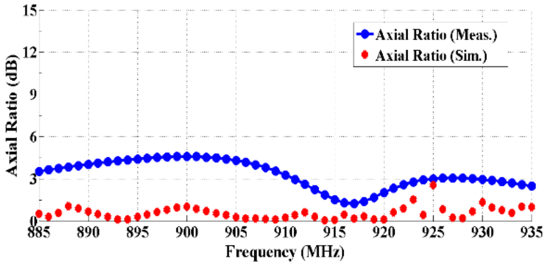

Fig. 12. Simulated and measured axial-ratio for the antenna.

The simulated $-3\,dB$ AR bandwidth of the proposed tag antenna is $50\,MHz$ $(885 - 935\,MHz)$, but the measured $-3\,dB$ AR bandwidth is $25\,MHz$ $(910 - 935\,MHz)$ slightly narrower than simulated one. The simulated antenna gains for the proposed antenna are shown Fig. 13.

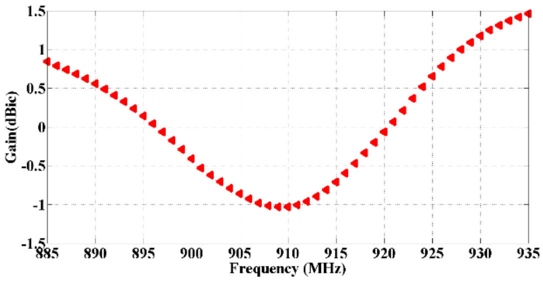

Fig. 13. Simulated antenna gains for the proposed antenna.

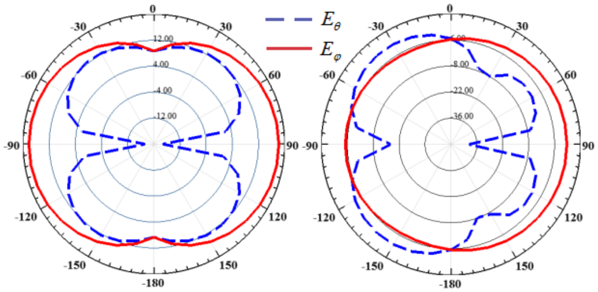

x-z plane Simulated y-z plane

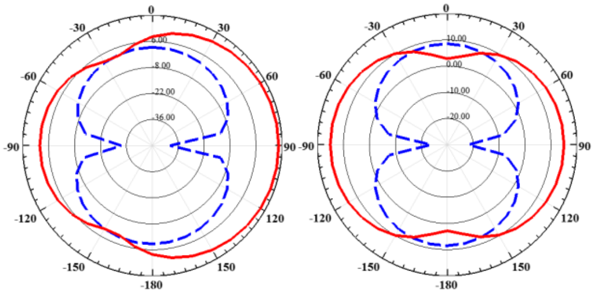

x-z plane Measured y-z plane

Fig. 14. Measured and simulated radiation patterns at 915 MHz for the proposed tag antenna.

The simulated and measured radiation pattern at $915\,MHz$ in two planes $(x - z,\ y - z)$ are shown in Fig. 14. It is seen that the value of E_θ and E_φ are approximately equal near $\theta = 0^o$ and $\theta = 180^o$ validating CP radiation in Z direction. The proposed antenna is simulated by sticking an Alien Higgs chip with $P_{th} = -14\,dBm$ [10]. In response to LHCP, RHCP and LP reader antenna, the gain and reading range of the antenna is calculated and the result portray in Fig. 15. The following friis equation is used to compute the maximum reading range:

$$r_{\max} = \frac{\lambda_o}{4\pi}\sqrt{\frac{P_t G_{tag}(\theta_t,\varphi_t) G_{reader}(\theta_r,\varphi_r)\rho\tau}{P_{th}}}\,, \tag{7}$$

$$\tau = \frac{4R_C R_A}{\left|Z_C + Z_A\right|^2}, \tag{8}$$

where $G_{reader}\ (\theta_r\ ,\ \varphi_r)$ is the gain of the reader antenna, $G_{tag}\ (\theta_t\ ,\ \varphi_t)$ is the gain of the tag antenna, P_{th} is the minimum requirement power to turn on the internal integrated circuits and detect the backscattered signal from the transmitter with power P_t, ρ is the polarization efficiency, and Z_C, Z_A in Equation (8) are correspondingly equivalent to impedance of chip and tag antenna. Table 2 presents the parameters which are used for calculating the reading range at 915 MHz.

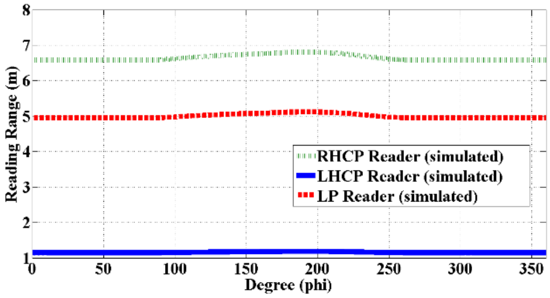

Fig. 15. Simulated reading ranges for rotating the proposed CP tags in the direction by using the RHCP reader antenna.

Table 2: Parameter values for the reading range at 915 MHz

P_t	λ	$G_{tag}\ (\theta = 0)$	G_{reader}	P_{th}	ρ		
					RHCP	LHCP	LP
1 (w)	0.32 (m)	0.25 (dB)	6 (dBi)	-14 (dBm)	0.99	0.003	0.56

IV. CONCLUSION

A compact cross dipole RFID tag antenna with wideband CP radiation is successfully designed and implemented. The CP bandwidth $(895 - 935\ MHz)$ is obtained by unequal slots insert to the dipoles. Moreover, in this BW the gain varied between -1 and 1 $dBic$, and the maximum reading range attained by using CP reader antenna is 6.7 mm. Also, the overall size of antenna is $(0.19\ \lambda_0 \times 0.19\ \lambda_0 \times 0.005\ \lambda_0)$ at 915 MHz. Therefore, the proposed structure is a good candidate for UHF RFID applications, particularly those that require long reading range and compact dimensions.

REFERENCES

[1] K. Finkenzeller, *RFID Handbook: Fundamentals and Applications in Contactless Smart Cards and Identification*. Wiley, 2003.

[2] W. Choi, J. Kim, J.-H. Bae, and G. Choi, “A small RFID tag antenna using proximity-coupling to identify metallic objects,” *IET Microwave and Optical Technology Letters*, vol. 50, pp. 2978-2981, 2008.

[3] Z. Fang, R. Jin, and J. Geng, “Asymmetric dipole antenna suitable for active RFID tags,” *IET Electronics Letters*, vol. 44, pp. 71-72, 2008.

[4] C. Horng-Dean and T. Yu-Hung, “Low-profile PIFA array antennas for UHF band RFID tags mountable on metallic objects,” *IEEE Transactions on Antennas and Propagation*, vol. 58, pp. 1087-1092, 2010.

[5] G. Marrocco, “The art of UHF RFID antenna design: impedance-matching and size-reduction techniques,” *IEEE Antennas and Propagation Magazine*, vol. 50, pp. 66-79, 2008.

[6] L. Ukkonen, M. Schaffrath, D. W. Engels, L. Sydanheimo, and M. Kivikoski, “Operability of folded microstrip patch-type tag antenna in the UHF RFID bands within 865-928 MHz,” *IEEE Antennas and Wireless Propagation Letters*, vol. 5, pp. 414-417, 2006.

[7] D. D. Deavours, “A circularly polarized planar antenna modified for passive UHF RFID,” *IEEE International Conference on RFID*, pp. 265-269, 2009.

[8] C. Chihyun, P. Ikmo, and C. Hosung, “Design of a circularly polarized tag antenna for increased reading range,” *IEEE Transactions on Antennas and Propagation*, vol. 57, pp. 3418-3422, 2009.

[9] C. Horng-Dean, K. Shang-Huang, C. Sim, and T. Ching-Han, “Coupling-feed circularly polarized RFID tag antenna mountable on metallic surface,” *IEEE Transactions on Antennas and Propagation*, vol. 60, pp. 2166-2174, 2012.

[10] C. Horng-Dean, C. Sim, and K. Shang-Huang, “Compact broadband dual coupling-feed circularly polarized RFID microstrip tag antenna mountable on metallic surface,” *IEEE Transactions on Antennas and Propagation*, vol. 60, pp. 5571-5577, 2012.

[11] P. Te, Z. Shuai, and H. Sailing, “Compact RFID tag antenna with circular polarization and embedded feed network for metallic objects,” *IEEE Antennas and Wireless Propagation Letters*, vol. 13, pp. 1271-1274, 2014.

[12] A. Nesic, I. Radnovic, M. Mikavica, S. Dragas, and M. Marjanovic, “New printed antenna with circular polarization,” *26th European Microwave Conference*, pp. 569-573, 1996.

[13] J. D. Kraus, *Antennas*. McGraw-Hill, 1988.

[14] C. A. Balanis, *Antenna Theory, Analysis and Design*. Second Edition, New York, John Wiley & Sons Inc., 1997.

Genetic Algorithm Based Shape Optimization Method of DC Solenoid Electromagnetic Actuator

Eduard Plavec [1], Ivo Uglešić [2], and Mladen Vidović [1]

[1] Switchgear and Controlgear Department
KONČAR Electrical Engineering Institute, Inc., Zagreb, 10 000, Croatia
eplavec@koncar-institut.hr, mvidovic@koncar-institut.hr

[2] Department of Energy and Power Systems
Faculty of Electrical Engineering and Computing, Zagreb, 10 000, Croatia
ivo.uglesic@fer.hr

Abstract **─** This paper presents the method for the shape optimization of the DC solenoid electromagnetic actuator using a genetic algorithm. Numerical simulation of its transient response includes simultaneously solving differential equations of magnetic, electrical and mechanical subsystems. The magnetic subsystem is analyzed by finite element method (FEM), while the electrical and mechanical subsystems are modeled separately and mutually coupled. A modified genetic algorithm is programmed in MATLAB software package. The shape optimization has been performed on two-dimensional (2D) axial-symmetric model of electromagnetic actuator. The measurement results obtained after the production and testing of electromagnetic actuator are compared with results of numerical simulation.

Index Terms **─** Electromagnetic actuator, finite element method, genetic algorithm, shape optimization, solenoid.

I. INTRODUCTION

Solenoid electromagnetic actuators are electromechanical devices which convert electrical energy to mechanical energy related to linear motion. They are characterized by their compact size and simple structure, and due to their reliability, simple activation and cheap production, they are widely used in many components that accompany our daily lives [1,2].

The design of solenoid electromagnetic actuators (EMA) starts with operating conditions of the device. DC electromagnetic actuators usually do not have a linear static characteristic, but it can be achieved by the coil current control or by changing the shape of the magnetic circuit [3]. The current control is usually not the simplest way as it requires sophisticated sensors, a microcomputer and various electronic components. A more suitable way is to adjust the electromagnetic device's magnetic conductive parts shape. This does not lead to a completely linear characteristic of plunger movement, but it can be considered as satisfactory [4].

The shape influence of magnetic conductive parts of EMA-s was studied by Roters [5] even in the forties of the last century. The development of optimization methods began with the development of computer technology [6]. Unlike the local optimization techniques, evolutionary algorithms, like GA, are not highly dependent on either initial conditions nor on constraints in the solution domain [7]. Evolutionary algorithms attempt to imitate nature, where all living organisms exist in a given environment [8]. This idea can be modified and used for optimization problem solutions based on numerical calculations, assuming that the environment is defined on known values and characteristics [9,10].

There are a lot of different techniques used for the shape optimization of electromagnetic devices, but the usage of GA for shape optimization of electromagnetic actuators exist only in a few references which are listed below. The shape optimization of the electromagnetic valve with fixed permanent magnet using a GA is shown in [11], while in [12] it is used in similar application for the multi-objective optimization of electromagnetic components.

This paper presents the shape optimization method of DC EMA. The numerical simulation of the transient response of EMA includes simultaneously solving differential equations of magnetic, electrical and mechanical subsystems. Numerical calculations are performed using the ANSYS Electronics software package which consists of several modules. The magnetic subsystem is analyzed by finite element method (FEM) using ANSYS Maxwell, while the electrical and mechanical subsystems are separately modeled in the ANSYS Simplorer and mutually coupled. The GA is programmed in a MATLAB software package and linked to ANSYS Maxwell, where the electromagnetic

Submitted On: September 15, 2017
Accepted On: January 1, 2018

calculations have been performed on 2D axial-symmetric model.

The main advantage of the method presented in this paper is the possibility of the optimization electromagnetic force acting on plunger at specific plunger displacement, which could be very useful in many different applications of EMA-s.

II. DESCRIPTION AND WORK PRINCIPLE

The basic structure of the solenoid EMA consists of a non-magnetic shaft, sleeve bearing, upper and lower core, magnetic conductive housing, non-magnetic part of housing, coil, working gap, plunger and return spring (Fig. 1).

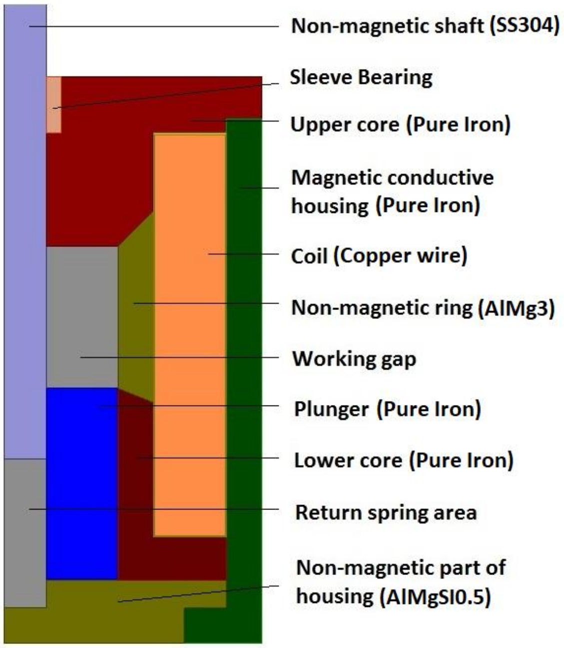

Fig. 1. DC solenoid electromagnetic actuator – basic structure (cross-section).

The non-magnetic shaft separates the magnetically conductive parts (cores and plunger) and transfers the mechanical force of the plunger to a certain mechanism that the electromagnetic actuator starts. The key role of sleeve bearing is to reduce sliding friction between the magnetic conductive upper core and the movable non-magnetic shaft. The stationary ferromagnetic core as well as the movable ferromagnetic plunger are the basic parts of the actuator through which the magnetic circuit closes. The cores, housing and plunger are made of electrically conductive material with non-linear B-H characteristics. The original purpose of the non-magnetic ring is to act like a plunger guide tube and to prevent its eccentric force, offering a smooth sliding surface with a low friction sliding coefficient. If the non-magnetic ring is located in the middle of the coil it can also increase the operating speed of the plunger [13]. The working gap, in some references also known as the main air gap, is the place where attraction force between the plunger and the core is generated, i.e., the place of electromechanical conversion of energy. The function of the return spring is to return the plunger to its initial position after switching off the EMA. The purpose of the non-magnetic part of the housing is to determine the initial position of the plunger.

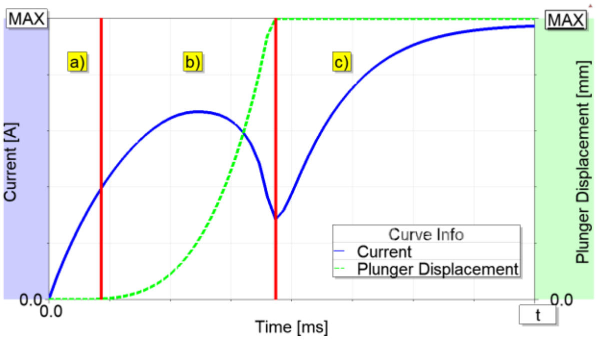

Fig. 2. The typical response behavior of the DC solenoid electromagnetic actuator.

The typical response behavior of DC EMA is illustrated in Fig. 2 and consists of the following three operation periods [14], mutually separated with red vertical lines:

a) The Sub-transient Period. In this period the plunger does not move, it is at rest despite the application of excitation voltage. The magnetic flux which flows through the plunger does not raise simultaneously with magnetomotive force (MMF) due to the presence of eddy currents.

b) The Transient Period. This period starts when the electromagnetic force of the plunger becomes larger than the initial return spring force and therefore the plunger starts to move. The movement of the plunger causes the varying magnetic flux in the EMA. The electromotive force (EMF), which opposes to the voltage source and causes the current drop, is induced in the coil due to change of linkage magnetic flux.

c) The Stopping Period. In this mode, the plunger touches the upper part of the core and finishes the movement, the EMF disappears and current continues to increase.

The EMA that should be optimized starts the newly developed high-voltage circuit breaker mechanism. It should overcome the force of 80 N at the plunger displacement of 6 mm and meet all the design constraints which are listed in Table 1. The mechanism's built–in switches are capable of breaking the current in the amount of 2.5 A.

Table 1: Design constraints parameters of EMA

Design Constraint Parameter	Value
Max. current	2.5 A
Electromagnetic force	>80 N (6 mm)
Actuator width	<60 mm
Actuator height	<70 mm
Plunger displacement	10 mm
Voltage supply	220 VDC

III. MATHEMATICAL MODEL

Dynamic modeling of the time response of the electromagnetic actuator is difficult because of the need to simultaneously solve non-linear differential equations of its magnetic, electrical and mechanical subsystem [15]. The equations which lead to time and space dependent electromagnetic magnitudes and which are also used to solve the magnetic subsystem of electromagnetic actuator are well known Maxwell's equations [16,17]:

$$div\vec{B} = 0, \tag{1}$$

$$rot\vec{H} = \overrightarrow{J_{EC}} + \vec{J}, \tag{2}$$

$$rot\vec{E_\iota} = -\frac{\partial \vec{B}}{\partial t}, \tag{3}$$

$$\overrightarrow{J_{EC}} = \sigma \cdot \vec{E_\iota}, \tag{4}$$

$$\vec{B} = \mu \cdot \vec{H}, \tag{5}$$

with the following notations: $\vec{B}$ – magnetic flux density and $\vec{H}$ – magnetic field strength, $\vec{J}$ – current density, $\overrightarrow{J_{EC}}$ – eddy current density, $\vec{E_\iota}$ – induced electric field strength, μ – permeability of material and σ – conductivity of material. To solve these equations in the case of axial-symmetric geometry, it is convenient to use the magnetic vector potential defined as:

$$\vec{B} = rot\vec{A}. \tag{6}$$

By combining the Equations (2), (4), (5) and (6) the following equations are obtained:

$$\vec{B} = \mu \cdot \vec{H} = rot\vec{A} \;\rightarrow\; H = B/\mu, \tag{7}$$

$$rot\left(\vec{B}/\mu\right) = \sigma \cdot \vec{E_\iota} + \vec{J}. \tag{8}$$

Furthermore, if we put expression (6) into the Equation (3) the following equation is obtained:

$$rot\vec{E_\iota} = -\frac{\partial \vec{B}}{\partial t} = -\frac{\partial (rot\vec{A})}{\partial t} \;\rightarrow\; \vec{E_\iota} = -\frac{\partial \vec{A}}{\partial t}, \tag{9}$$

$$rot\left(\frac{rot\vec{A}}{\mu}\right) = -\sigma \cdot \frac{\partial \vec{A}}{\partial t} + \vec{J}. \tag{10}$$

In the case of axial-symmetric geometry, the vector potential $\vec{A}$ has only one component and that scalar function depends on two space variables (r, z) and time (t). The final expression for the time dependable differential equation of magnetic subsystem, with implementation of all causes of eddy currents is [1]:

$$\frac{\partial}{\partial z}\left(\frac{1}{\mu} \cdot \frac{\partial \vec{A}}{\partial z}\right) + \frac{\partial}{\partial r}\left(\frac{1}{\mu} \cdot \frac{1}{r} \cdot \frac{\partial (r \cdot \vec{A})}{\partial r}\right) = \sigma \cdot \frac{\partial \vec{A}}{\partial t} - \vec{J}. \tag{11}$$

This equation should be solved taking into consideration the boundary condition $(\overrightarrow{A_z} = 0)$ in reference to the system of stationary and movable parts of the EMA. The electric subsystem is composed of coil and DC power supply. The applied voltage U is given as a function of current and time and can be expressed, after the simplification of the linkage flux expression, with the following differential equation:

$$\lambda = N \cdot \Phi = NBS = N \cdot \mu_0 \frac{N \cdot i}{h} \cdot S = L \cdot i, \tag{12}$$

$$(R_i + R_Z) \cdot i(t) + \frac{d\lambda(i,z)}{dt} = U(t), \tag{13}$$

with the following notations: λ – linkage magnetic flux, N – number of turns, Φ – magnetic flux, B – magnetic flux density, S – cross section area of coil, i – coil current, h – height of coil, R_i – resistance of power supply, R_z – resistance of coil, U – applied voltage.

The position of movable plunger is defined by the following equation of motion:

$$m\frac{d^2z}{dt} + \gamma\frac{dz}{dt} + kz = F_e - F_R, \tag{14}$$

where γ and k are friction and stiffness coefficients. F_e and F_R are electromagnetic force and friction force, while m is the mass of the plunger. The model of all three subsystems are mutually coupled in the ANSYS Electronics software package, as it is shown in Fig. 3.

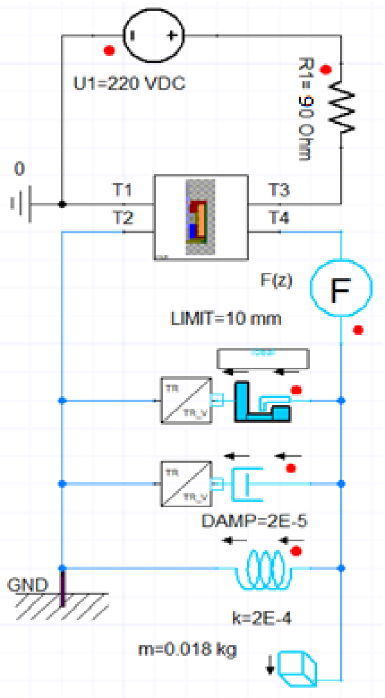

Fig. 3. The model of DC solenoid EMA in ANSYS Electronics.

The electromagnetic force acting on the plunger in dependence on plunger displacement, is obtained as follows. Coil width can be calculated using following equation:

$$w_c = N_x \cdot D_w, \tag{15}$$

where N_x is, the number of turns in x direction and D_w is wire diameter. To calculate the coil height, the Pappus centroid theorem for volume of solids of revolution is used:

$$V = 2\pi \cdot A \cdot d = L \cdot A_w = \frac{R}{R_{lin}} \cdot A_w, \qquad (16)$$

where A is, the area of the surface which is rotating, d is the distance of its geometric centroid from the axis of revolution, L is the length of wire, A_w is the area of the wire cross section, R is the coil resistance and R_{lin} is the linear resistance. The distance and area can be obtained using equations:

$$d = w_c + r_{po} + t_{lc}, \qquad (17)$$

$$A = N_x \cdot N_y \cdot A_w, \qquad (18)$$

$$N_y = h_c / D_w, \qquad (19)$$

with the following notations: r_{po} – plunger outer radius, t_{lc} – lower core thickness, N_y – number of turns in y direction, h_c – coil height (Fig. 4). By combining the Equations (16), (17), (18) and (19) it is obtained the equation for calculation of the coil height:

$$h_c = \frac{D_w \cdot R}{\pi \cdot N_x \cdot R_{lin} \cdot (r_{po} + w_c + t_{lc})}. \qquad (20)$$

From the definition of Maxwell Stress Tensor and the properties of Kronecker delta with the fact that the magnetic field B has only y component, it is possible to write the force acting on plunger as:

$$\sigma_{yy} = \frac{1}{\mu_0} B_y B_y - \frac{1}{2\mu_0} B^2 \delta_{yy}, \qquad (21)$$

$$\sigma_{yy} = \frac{1}{\mu_0} B^2 - \frac{1}{2\mu_0} B^2 = \frac{B^2}{2\mu_0} = F, \qquad (22)$$

$$F_e(z) = \frac{\mu_0 (NI)^2 S}{2\left(\frac{l_m}{\mu_r} + z\right)^2}, \qquad (23)$$

where S is, the cross-section area of plunger, l_m is the length of the path along ferromagnetic material, μ_r is relative permeability of material and z is the plunger displacement. The cross-section area of the plunger can be obtained using equation:

$$S = \pi \cdot (r_{po}^2 - r_{nms}^2), \qquad (24)$$

where r_{nms} is the radius of non-magnetic shaft. Length of the path along the ferromagnetic material is calculated using the following equation:

$$l_m = 2_{rco} - 2r_{nms} + t_h + \frac{t_{lcb}}{2} + h_c + t_{lc} - r_{ci} + h_p + i_{lc} + i_{uc} + h_{uc}, \qquad (25)$$

with the following notations: r_{co} – coil outer radius, t_h – housing thickness, t_{lcb} – lower core base thickness, h_c – coil height, t_{lc} – lower core thickness, r_{ci} – inner coil radius, h_p – plunger height, h_{sb} – sleeve bearing height, i_{lc} – incline of lower core, i_{uc} – incline of upper core, t_{ucb} – upper core base thickness, (Fig. 4). If we combine Equations (15), (20), (22), (23), (28) and put it in Equation (21) the final expression for force acting on plunger is obtained.

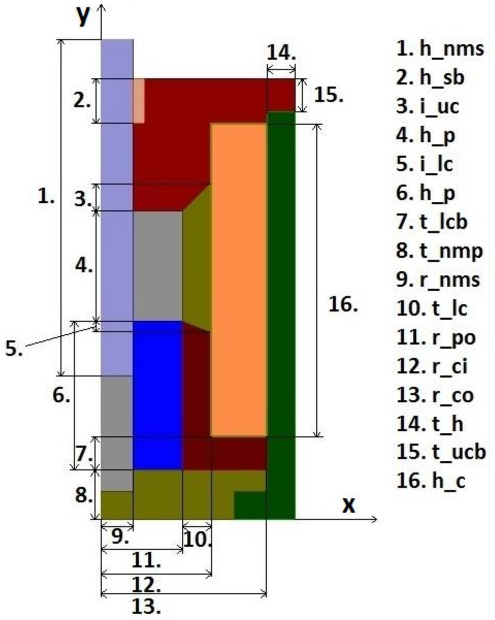

Fig. 4. Design variables overview.

IV. METHODOLOGY

The electromagnetic calculation is performed using the ANSYS Electronics software package, using its two modules, ANSYS Maxwell and ANSYS Simplorer. ANSYS is started in interactive mode (not batch mode), so if we have a repetitive task that just needs to change some parameters, there is no need to start up ANSYS for all studies, which saves up a lot of time and is very interesting when performing the optimization process.

The first step to link Maxwell with MATLAB is writing an ANSYS script in an ANSYS ADPL environment. The second step is creating a batch file to run ANSYS from MATLAB. The batch file is used for communication, to forward results of finite element analysis (FEA) to MATLAB and to return input parameters from MATLAB to ANSYS (Fig. 5).

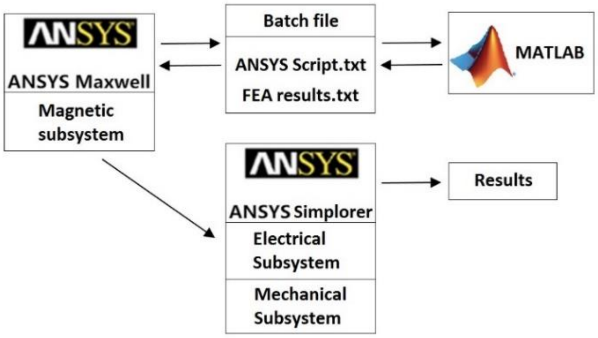

Fig. 5. Overview of computation methodology.

MATLAB performs the geometry generation calculations, the analysis required to suggest a geometry which approaches the optimal shape design of EMA, using the GA. The inputs to the GA are the design parameters, constraints and objectives that need to be maximized. The main parameters required by the GA (Table 2), such as the number of individuals to be analyzed, the mutation rate, crossover rate, the list of variables we are optimizing and the maximum number of iterations are declared in ANSYS script.

Table 2: The main parameters of GA

Number of Individuals	30
Crossover Rate	0.6
Mutation Rate	0.05
Crossover Type	Uniform
Mutation Type	Uniform
Maximum Number of Iterations	5000

The optimization process in MATLAB starts with a randomly generated population of design variables, with their initial values encoded as genes in a chromosome [18]. Once the population is initialized the operators are used to modify genes after which the fitness function is called [19]. As the design objective is to maximize force at a specific plunger displacement taking all the constraints into consideration, the fitness function converted to the minimization problem is:

$$\text{Fitness Funtion} = \text{Minimize}\left(\frac{1}{F_e(z)}\right). \qquad (26)$$

At this point all the constraints are checked, objective values computed and ANSYS Maxwell module is provided with a shape of geometry. Numerical simulation results of magnetic subsystem of EMA-a are then forwarded to the ANSYS Simplorer where the subsystems are mutually coupled and results are obtained. This process is repeated until a stopping criterion is reached, which happens when the number of generations is reached or solution has converged (Fig. 6).

The seventeen design variables are selected to operate shape optimization of the presented EMA. The parts which are very sensitive to the change of reluctance, like the top end area of the plunger, have its shape separated with a few more sub-variables to achieve the most suitable shape as it is described in [1]. Due to the initial design constraint on plunger displacement it is possible to fix the working gap variable to the required value as well as neglect variables that have no effect on electromagnetic properties of EMA, it will speed up the optimization process.

Depending on the initial constraints on current and voltage supply it is possible to calculate coil resistance and parametrize coil. The inner coil radius is defined by the plunger outer radius and thickness of lower core:

$$r_{ci} = r_{po} + t_{lc}. \qquad (27)$$

The outer coil radius is defined by coil resistance, wire diameter, bare wire diameter, coil height, winding stacking factor and the inner coil radius:

$$r_{co} = \sqrt{\frac{R\cdot D_{bw}^2\cdot D_w^2}{4\cdot\rho\cdot h_c\cdot p} + r_{ci}^2}, \qquad (28)$$

$$D_{bw} = 0.0826\cdot 1.123^{-AWG}, \qquad (29)$$

$$D_w = 0.0082\cdot 0.8931^{AWG}, \qquad (30)$$

with the following notations: R – coil resistance, D_{bw} – bare wire diameter, ρ – resistivity, r_{ci} – coil inner radius, r_{co} – coil outer radius, D_w – wire diameter, h_c – coil height, p – winding stacking factor, AWG – American wire gauge. According to the references [6,7,18], the values of the winding stacking factor are in range from 0.65 to 0.8.

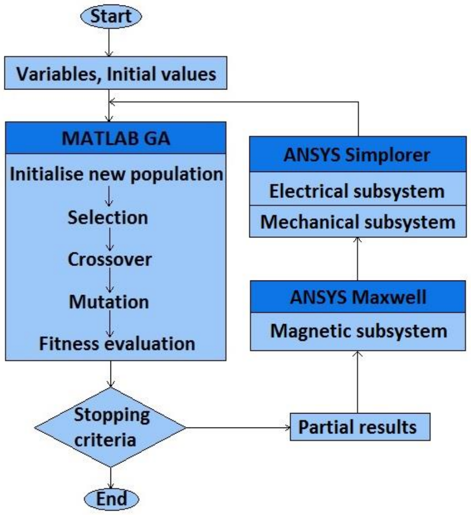

Fig. 6. Flow diagram of the optimization process.

V. ANALYSIS OF NUMERICAL RESULTS

The developed method has been applied to DC solenoid EMA with exciting external voltage as a step function (220 V). The optimization process had been performed on a PC with CPU Intel Core i7 (3.8 GHz, 16 cores) and 64 GB RAM. The solution converged after two weeks of calculation and 2348 generations (Fig. 7).

At the beginning of the transient phenomenon, the eddy currents, which oppose the magnetic field of coil by their magnetic field, are induced. This phenomenon is called magnetic diffusion and causes a penetration delay of the magnetic field in the interior of housing, cores and plunger, which adversely affects the response time of the EMA.

The magnetic diffusion phenomenon can be clearly seen in Fig. 8, where the distribution of the magnetic field in EMA at t=1.6 ms, t=4.6 ms and t=5.6 ms is illustrated. The magnetic flux in the working gap is distributed uniformly in the radial direction, while that is not the case with flux distribution on the pole face of the plunger (Fig. 9). This phenomenon is called the pole face effect [20]. The steady-state magnetic flux is not uniform due to the hysteresis effect of the magnetic core.

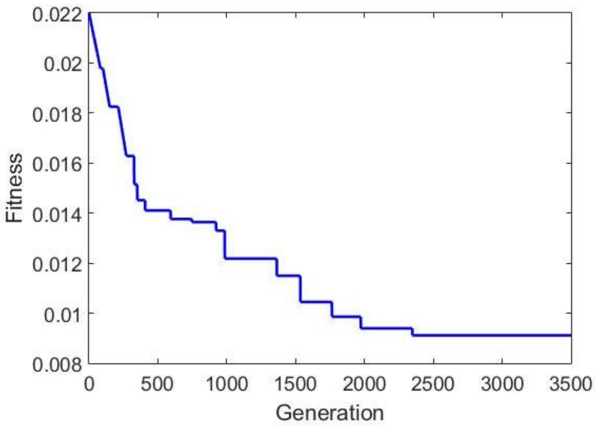

Fig. 7. Genetic algorithm convergence curve.

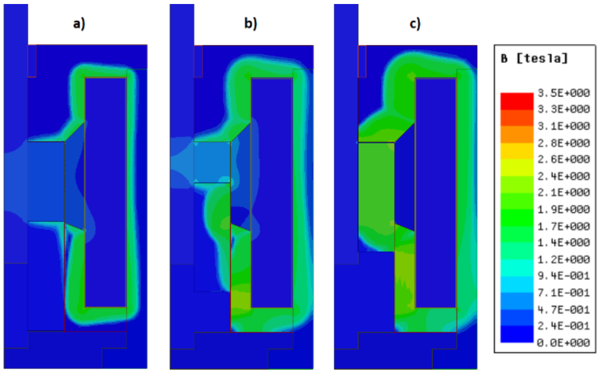

Fig. 8. Dynamic distribution of magnetic field in the actuator at: (a) t=1.6 ms, (b) t=4.6 ms, and (c) t=5.6 ms.

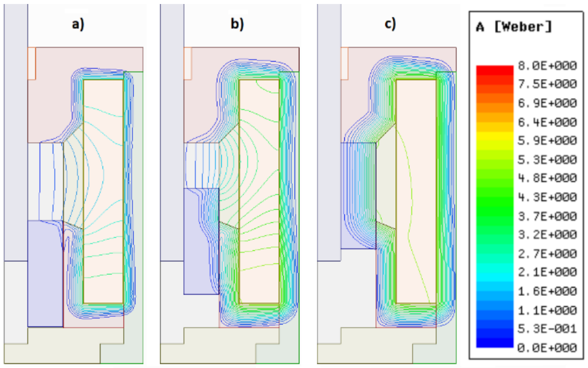

Fig. 9. Dynamic flux distribution in the actuator at: (a) t=1.6 ms, (b) t=4.6 ms, and (c) t= 5.6 ms.

Numerical simulation results of the coil current, plunger displacement, speed, induced voltage and flux linkage are shown in Fig. 10 and Fig. 11 as functions of time.

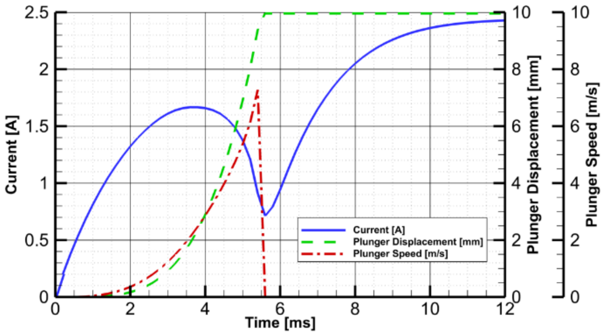

Fig. 10. Numerical simulation results of solenoid EMA.

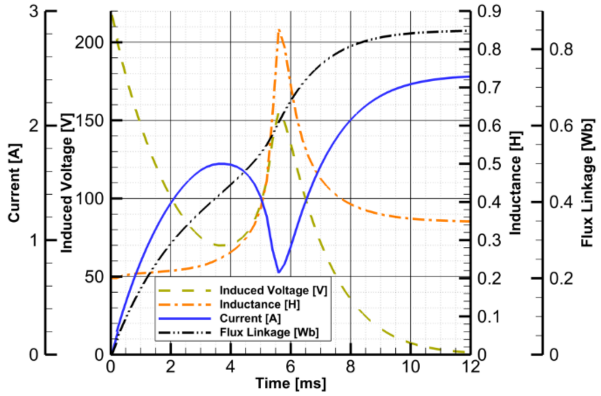

Fig. 11. Numerical simulation results (2) of solenoid EMA.

The plunger does not start to move until the magnetic flux penetrates into the plunger enough and electromagnetic force on the plunger overcomes the initial load force of spring (0.4 N). During the motion, the plunger reaches the maximum speed of 7.3 m/s. The time response of simulated EMA is 5.59 ms. The static values of electromagnetic force depending on the plunger displacement are obtained using the magnetostatic calculation. The results are shown in Fig. 12.

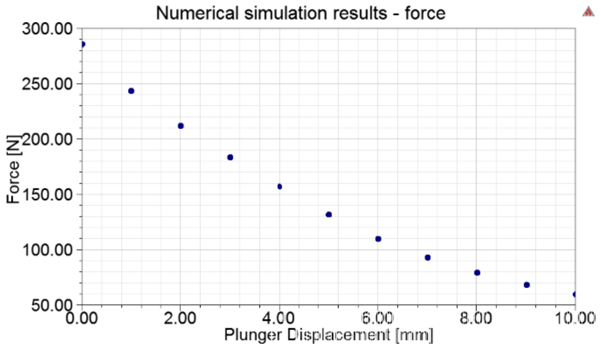

Fig. 12. Numerical simulation results of solenoid EMA, force characteristics.

At maximum plunger displacement, the static electromagnetic force has its minimum value of 59.7 N. As the plunger approaches the end of motion, the force continues to increase. The maximum static electromagnetic force is reached at the end of motion and its value is 285.1 N. Since the static value of electromagnetic force at plunger displacement of 6 mm is higher than 80 N, the initial design constraint is satisfied.

VI. MANUFACTURING, TESTING AND RESULTS COMPARISON

After completion of the optimization process, the 3D model of the most optimal shape of electromagnetic actuator and square fasten plate are modeled in SolidWorks, after which the prototype is sent to manufacturing. The final optimized values of design variables are stated in Table 3.

Table 3: Optimized values of design variables

	Design Variable	Range	Optimized Value
1.	h_{nms}	20-60 mm	50 mm
2.	h_{sb}	2-10 mm	4 mm
3.	i_{uc}	0-7 mm	4.4 mm
4.	z	10 mm	10 mm
5.	i_{lc}	0-5 mm	3.2 mm
6.	h_p	9-16 mm	15.2 mm
7.	t_{lcb}	2-5 mm	4.1 mm
8.	t_{nmp}	3 mm	3 mm
9.	r_{nms}	2-5 mm	2.5 mm
10.	t_{lc}	2-5 mm	2.2 mm
11.	r_{po}	2-15 mm	11.5 mm
12.	r_{ci}	5-20 mm	13.7 mm
13.	r_{co}	6-40 mm	16.0 mm
14.	t_h	2-5 mm	2.0 mm
15.	t_{ucb}	2-8 mm	2.8 mm
16.	h_c	10-50 mm	29.7 mm
17.	h_{uc}	10-25 mm	13.8 mm
18.	AWG	29-34	32

The prototype of the EMA, after the manufacturing process, had been tested in the laboratory. The measured sizes are: plunger displacement, electromagnetic force on the plunger, coil current and coil resistance. The coil resistance, measured using a standard multimeter (FLUKE 88V/A), is 87.5 Ω, which is slightly less than 3% to the simulated value. The transient recorder (National Instruments TR12K) with sample rate of 20 MS/s and its acquisition unit is used to measure fast transient phenomena precisely. The inductive LVDT sensor (induSENSOR DTA25), connected to the transient recorder's acquisition unit and attached to the non-magnetic shaft of EMA, is used to measure the plunger displacement. The prototype of EMA is fixed to the testing unit using a non-magnetic material not to affect the magnetic field of EMA. The test configuration is illustrated in Fig. 13.

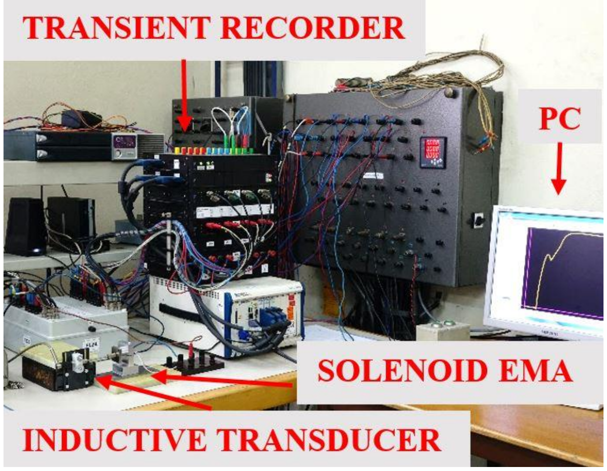

Fig. 13. Testing of prototype EMA.

The comparison of the numerical simulation results and the measurement results of the plunger displacement and coil current, are illustrated in Fig. 14.

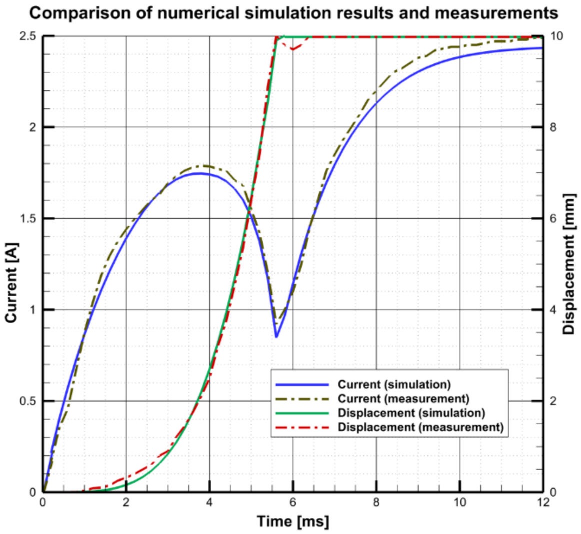

Fig. 14. Comparison of numerical simulation results and measurements.

The measured time response of tested EMA is 5.5 ms, which is 1.6% less than the numerical simulation response. The maximum deviation between the calculated and measured values of the coil current is 4%, while the maximum deviation between calculated and measured values of plunger displacement is 5%. The reasons the simulated results of coil current are smaller than measured results are the difference in calculated and measured coil resistance and neglection of friction between the sleeve bearing and the non-magnetic shaft. The maximum deviation of simulated results and measurements of plunger displacement is obtained at the end of motion, when plunger rebounds.

The force measurement is conducted using a previously mentioned testing unit, but instead of inductive sensor the spring with known characteristic is used. The force is measured in nine points, repeatedly at every 1 mm of distance between solenoid EMA and testing unit. Based on the spring characteristics and its compression, the force that EMA has to overcome at specific distance is calculated. If the force amount is too large, the same is decreased to the level which EMA can overcome. The test configuration can be seen in Fig. 15.

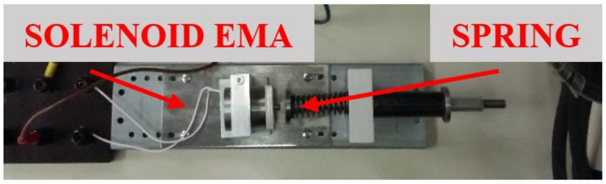

Fig. 15. Force measurement test configuration.

The force measurement of this type gives the static values of electromagnetic force at specific distance and is not comparable to the dynamic electromagnetic force of transient numerical simulation. In order to compare transient numerical simulation results of the electromagnetic force with the measurements, magnetostatic calculation is performed with current values that correspond to forces for specific values of distance between the EMA and the testing unit. A comparison of numerical simulation results and force measurements are shown in Fig. 16.

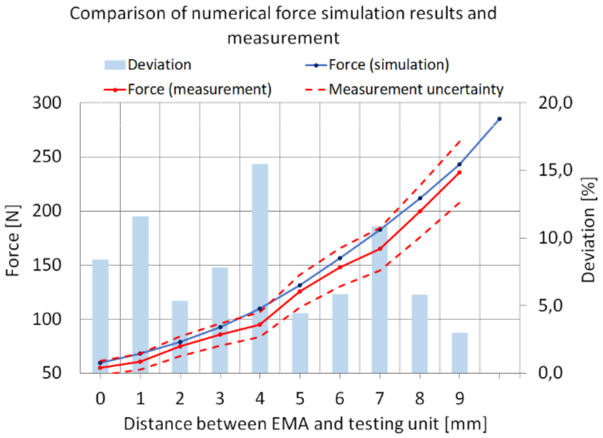

Fig. 16. Comparison of numerical force simulation results and measurement.

The maximum measured value of the static electromagnetic force, at the distance between the EMA and the testing unit of 9 mm, is 236 N. The static electromagnetic force measured at a plunger displacement of 6 mm is 149.8 N and it satisfies the initial design constraint. The maximum deviation between the calculated and measured values of the static electromagnetic force is 16.1%, at a distance between the EMA and the testing unit of 4 mm. At the same time, this measurement point is the only point which is outside the uncertainty zone (±12%) of force measurement unit. The main reason for this deviation is insufficiently precise force measurement method which should be improved on in further work.

The prototype model of the EMA (Fig. 17) has radius of 18 mm, while its overall height is 47 mm, which meets the initial design constraints (Table 1) on the actuator width and height. Compared to the initial design which is developed in the late nineties, the optimized design has smaller dimensions and a faster time response. Using the described optimization method electromagnetic force has increased during the plunger motion, while the maximum force at the end of motion is 5.93% less than initial design (Table 4). Since the effective working range of both EMA-s is between 6 and 8 mm of the plunger displacement, the maximum force at the end of motion is not so important.

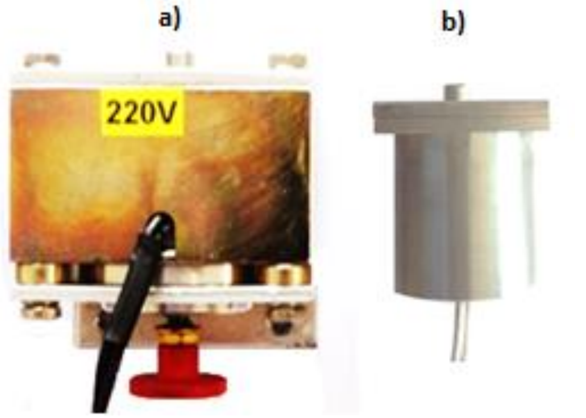

Fig. 17. Design of EMA-s: (a) initial and (b) optimized.

Table 4: Comparison of initial and optimized model of EMA

	Initial Design	Optimized Design	Improvement
Height [mm]	80	47	**-41.25%**
Width [mm]	63	36	**-42.86%**
F_{MAX} [N]	250	236	**-5.6%**
$F(6\,mm)$ [N]	114	156	**+36.84%**
Time response [ms]	8	5.6	**-30%**

VII. CONCLUSION

Electromagnetic actuators (EMA-s) which start some kind of tripping mechanism usually need a certain force value at specified plunger displacement to overcome the initial force of tripping mechanism. Maximizing the electromagnetic force during the time response usually results with a maximized electromagnetic force at the end of motion, in the saturation area, which is not very useful in this case. In this paper, the shape optimization method of the EMA-s which is based on a genetic algorithm and the finite element method, with the added ability to maximize electromagnetic force at desired plunger displacement, is presented.

After completion of the optimization process, the EMA with the most optimal shape is produced and tested in laboratory. The presented optimization method of the EMA gives the simulation results with a maximum deviation of 4% compared to the measured values of coil current and 5% compared to measured values of plunger displacement. The maximum deviation between force measurements and simulated results are 16.1% due to the insufficiently precise force measurement method, which needs to be improved. Using the presented optimization method, the achieved electromagnetic force acting on the plunger at a plunger displacement of 6 mm is 157 N, which is an improvement of 36.84% compared to the initial model of EMA. Also, based on this method, the dimensions of EMA are reduced 70.2% in height and 75% in width.

Based on the obtained results, it can be concluded that this method can successfully optimize the shape and describe the dynamic behavior of EMA-a and therefore be used for the design and development of such systems.

REFERENCES

[1] E. Plavec and M. Vidović, “Genetic algorithm based plunger shape optimization of DC solenoid electromagnetic actuator,” *24th Conf. IEEE TELFOR 2016*, Belgrade, 2016.

[2] D. Cvetković, I. Ćosić, and A. Šubić, “Improved performance of the electromagnetic fuel injector solenoid actuator using a modelling approach,” *International Journal of Applied Electromagnetics and Mechanics*, vol. 27, pp. 251-273, IOS Press, 2008.

[3] S.-B. Yoon, J. Hur, Y.-D. Chun, and D.-S. Hyun, “Shape optimization of solenoid actuator using the finite element method and numerical optimization technique,” *IEEE Trans. Mag*., vol. 33, Sept. 1997.

[4] T. Glück, *Soft Landing and Self-sensing Strategies for Electromagnetic Actuators*, ISSN 1866-2242, Shaker Verlag, Aachen, 2013.

[5] H. C. Roters, *Electromagnetic Devices*, New York, 1941.

[6] F. Mach, I. Novy, P. Karban, and I. Doležel, “Shape optimization of electromagnetic actuators,” *IEEE Conf. ELEKTRO*, pp. 595-598, 2014.

[7] O. G.Bellmunt and L. F.Campanile, *Design Rules for Actuators in Active Mechanical Systems*, Springer, New York, 2010.

[8] H. R. E. H. Bouchekara and M. Nahas, “Optimization of electromagnetics problems using an improved teaching-learning-based-optimization technique,” *ACES Journal*, vol. 30, no. 12, Dec. 2015.

[9] R. Diaz de Leon-Zapata, G. Gonzalez, A. G. Rodriguez, E. Flores-Garcia, and F. J. Gonzalez, “Genetic algorithm for geometry optimization of optical antennas,” *Proceedings of the COMSOL Conference*, Boston, 2016.

[10] S. M. Makouie and A. Ghorbani, “Comparison between genetic and particle swarm optimization algorithms in optimizing ships’ degaussing coil currents,” *ACES Journal*, vol. 31, no. 5, May 2016.

[11] S. H. Lee, H. C. Yi, K. Han, and J. H. Kim, “Genetic algorithm-based design optimization of electromagnetic valve actuators in combustion engines,” *ENERGIS*, vol. 8, pp. 13222-13230, 2015.

[12] A. Subbiah and O. Ladin, “Genetic algorithm based multi-objective optimization of electromagnetic components using COMSOL® and MATLAB®,” *COMSOL Conference Proceedings*, Boston, 2016.

[13] J. S. Ryu, Y. Yao, C. S. Koh, S. N. Yun, and D. S. Kim, “Optimal shape design of 3D nonlinear electromagnetic devices using parametrized design sensitivity analysis,” *IEEE Trans. Mag*., vol. 41, no. 5, 2005.

[14] R. Narayanswamy, D. P. Mahajan, and S. Bavisetti, “Unified coil solenoid actuator for aerospace application,”*Electrical Systems for Aircraft,Railway and Ship Propulsion (ESARS), IEEE*, 2012.

[15] M. Hassani and A. Shoulaie, “Dynamic modeling of linear actuator using fuzzy system to approximate magnetic characteristics,” *ACES Journal*, vol. 30, no. 8, Aug. 2015.

[16] D. Jiles, *Introduction to Magnetism and Magnetic Materials*, CRC Press, 2016.

[17] M. Lahdo, T. Ströhla, and S. Kovalev, “Magnetic propulsion force calculation of a 2-DOF large stroke actuator for high-precision magnetic levitation system,” *ACES Journal*, vol. 32, no. 8, Aug. 2017.

[18] S. R. B. Rama and D. Vakula, “Optimized polygonal slit rectangular patch antenna with defective ground structure for wireless applications,” *ACES Journal*, vol. 30, no. 11, Nov. 2015.

[19] G. Liu, Y. Wang, X. Xu, W. Ming, and X. Zhang, “The optimal design of real time control precision of planar motor,” *ACES Journal*, vol. 32, no. 10, Oct. 2017.

[20] K. Bessho and S. Yamada, “Analysis of transient characteristics of plunger-type electromagnets,” *Electrical Engineering in Japan*, vol. 82, no. 4, 1978.

Eduard Plavec was born in 1988, in Zagreb, Croatia. He is a Ph.D. student at University of Zagreb, Faculty of Electrical Engineering and Computing where he also received his B.Sc. and M.Sc. degrees in Electrical Engineering and Information Technology in 2011 and 2013, respectively.

He joined KONČAR Electrical Engineering Institute in 2014, where he began as a Research and Development Engineer in the field of electromagnetics at the Switchgear and Controlgear Department. His areas of interest include computational electromagnetics and high-voltage engineering.

He is a Member of the CIGRÉ Study Committee A3 – High-voltage equipment, IEEE Member since 2012 and ACES Member since 2016.

Ivo Uglešić was born in Zagreb, Croatia, in 1952. He received his Ph.D. degree in Electrical Engineering and Computing from the University of Zagreb, Croatia, in 1988.

Currently, he is a Professor at the Faculty of Electrical Engineering and Computing (Department of Energy and Power systems), University of Zagreb. He is the Head of the High-Voltage Laboratory at the Faculty of Electrical Engineering and Computing. His areas of interest include high-voltage engineering and power transmission.

Mladen Vidović was born in Zagreb, Croatia. He received his B.Eng. degree from University of Zagreb, Faculty of Electrical Engineering in 1984.

He has been working in KONČAR Electrical Engineering Institute since 1986, at Switchgear and Controlgear Department where he is currently the Head of Research and Development Section. His areas of interest are design and diagnostic of high-voltage switchgears and development of on-line monitoring systems of high-voltage apparatus. He is the author of several papers and patents.